DE-AC26-98BC15109

DEVELOPMENT OF AN IMPROVED SIMULATOR FOR CHEMICAL AND MICROBIAL IOR METHODS

Final Report

September 30, 1998 to September 29, 2001

By

Gary A. Pope
Kamy Sepehrnoori
Mojdeh Delshad
October 2001

Work Performed under Contract No. DE–AC26-98BC15109

Prepared for U.S. Department of Energy

Purna Halder, Project Manager

U.S. Department of Energy
National Petroleum Technology Office
P.O. Box 3628
Tulsa, OK 74101

Prepared by

Center for Petroleum and Geosystems Engineering
The University of Texas at Austin
Austin, Texas 78712

TABLE OF CONTENTS

Page

SECTION 1

SECTION 2

SECTION 3

SECTION 4

ABSTRACT

This is the final report of a three-year research project on further development of a chemical and microbial improved oil recovery reservoir simulator. The objective of this research was to extend the capability of an existing simulator (UTCHEM) to improved oil recovery methods which use surfactants, polymers, gels, alkaline chemicals, microorganisms and foam as well as various combinations of these in both conventional and naturally fractured oil reservoirs.

The first task was the addition of a dual-porosity model for chemical IOR in naturally fractured oil reservoirs. We formulated and implemented a multiphase, multicomponent dual porosity model for enhanced oil recovery from naturally fractured reservoirs. The multiphase dual porosity model was tested against analytical solutions, coreflood data, and commercial simulators.

The second task was the addition of a foam model. We implemented a semi-empirical surfactant/foam model in UTCHEM and validated the foam model by comparison with published laboratory data.

The third task addressed several numerical and coding enhancements that will greatly improve its versatility and performance. Major enhancements were made in UTCHEM output files and memory management. A graphical user interface to set up the simulation input and to process the output data on a Windows PC was developed. New solvers for solving the pressure equation and geochemical system of equations were implemented and testes. A corner point grid geometry option for gridding complex reservoirs was implemented and tested.

Enhancements of physical property models for both chemical and microbial IOR simulations were included in the final task of this proposal. Additional options for calculating the physical properties such as relative permeability and capillary pressure were added. A microbiological population model was developed and incorporated into UTCHEM. We have applied the model to microbial enhanced oil recovery (MEOR) processes by including the capability of permeability reduction due to biomass growth and retention. The formations of bio-products such as surfactant and polymer surfactant have also been incorporated.

EXECUTIVE SUMMARY

Pioneering research being conducted at The University of Texas at Austin is providing a scientific and engineering basis for modeling the improved recovery of oil and the enhanced remediation of aquifers through the development and application of compositional simulators. This research has resulted in the development and application of UTCHEM, a 3D, multicomponent, multiphase, compositional model of chemical flooding processes. The model accounts for complex phase behavior, chemical and physical transformations and heterogeneous porous media properties, and uses advanced concepts in high-order numerical accuracy and dispersion control. The flow and mass-transport equations are solved for any number of user-specified chemical components (water, oil, surfactant, alcohols, polymer, chloride, calcium, other electrolytes, tracers, cross linkers, etc.). These components can form up to four fluid phases (air, water, oil, and microemulsion) and any number of solid minerals depending on the overall composition. The simulator has been developed and applied to AOR modeling over many years. The oil industry has supported its development continuously for many years, but DOE FE contracts have been the single largest source of funding. UTCHEM source code has been requested and distributed by us to about 100 industrial and academic organizations. These groups use it for a wide variety of applications. Many of them as well as ourselves have validated it against a wide variety of laboratory and field data. Its numerical accuracy has been demonstrated repeatedly by comparisons with a variety of analytical solutions when available and by comparisons with other well-known commercial simulators for special cases such as water flooding that can be simulated by these simulators. Because of this, it has become the standard general-purpose chemical flooding simulator for the industry. Nevertheless, there is an important need for additional development of UTCHEM along the lines described below.

UTCHEM source code and the documents became available for download at our CPGE web page http://www.pe.utexas.edu/cpge/UTCHEM/ in October 2000 and since then more than 100 individuals have downloaded the code.

The objective of this research was to extend the capability of UTCHEM to advanced oil recovery (AOR) methods that use surfactants, polymers, gels, alkaline chemicals, microorganisms and foam as well as various combinations of these in both conventional and naturally fractured oil reservoirs. Chemical and microbial methods of improving oil recovery has been extensively developed and tested, but there has been very little research on how and when to combine them or how to apply them in naturally fractured reservoirs and better modeling of these processes is one of the critical elements needed to advance these technologies.

We have developed and implemented a multiphase and multicomponent dual porosity model so the use of chemical methods in naturally fractured oil reservoirs can be evaluated. A dual porosity model of naturally fractured media assumes that there are two distinct transport systems: an interconnected fracture system and a disjoint matrix system. The dual porosity formulation allows flow in both matrix and fracture. The exchange of fluids between the fracture and matrix rock is based on the Warren and Root theory. Mass transfer between the fracture and matrix rock includes diffusion, convection, imbibition, and gravity drainage. The dual porosity model adds additional subgridding to the main finite difference grid. The matrix blocks are divided into smaller sections, so that the transport within the blocks can be modeled accurately. The results of model validation against analytical solutions of known problems and laboratory coreflood experiments are presented.

We have also implemented a semi-empirical foam model in UTCHEM that describes gas mobility reduction and accounts for the effects of shear thinning due to gas flow rate and water and oil saturations. The model accounts for these effects in a way consistent with the capillary pressure mechanisms that has been successful in representing foam displacements. We were successful in history matching several published laboratory foam experiments.

A microbiological population model has also been incorporated into UTCHEM. The implementation includes very general kinetics and mass transfer models so it can accommodate any number of substrates, electron acceptors and biological species. It can model the substrate inhibition, substrate competition, electron acceptor inhibition, abiotic decay, biomass growth, and biomass attachment. We have applied the model to microbial enhanced oil recovery processes by including the capability of permeability reduction due to biomass growth and retention. The formations of bio-products such as surfactant and polymer surfactant have also been incorporated.

SECTION 1

TASK 1: DUAL POROSITY MODEL

Many oil reservoirs in the United States are naturally fractured, and some of the larger ones like Spraberry contains billions of barrels of remaining oil, but relatively little research has been done on the use of advanced oil recovery methods. In addition, very little success has been achieved in increasing the oil production from these complex reservoirs. The use of chemical methods of improved oil recovery from naturally fractured reservoirs has been particularly neglected. Some laboratory experiments have been done to investigate the use of surfactants in fractured chalk (Al-Lawati and Saleh, 1996; Austad, 1994; Keijzer and De Vries, 1990; Schechter *et al.*, 1991). However, the results of these studies are hard to interpret and to apply to field-scale predictions without a model that takes into account both the fluid flow and chemical phenomena in both fractures and rock matrix. The most efficient approach to modeling naturally fractured reservoirs appears to be the dual-porosity model, first proposed by Barenblatt *et al.* (1960) and introduced to the petroleum industry by Warren and Root (1963). The dual-porosity model assumes that two equivalent continuous porous media are superimposed: one for fractures and another for the intervening rock matrix. A mass balance for each of the media yields two continuity equations that are connected by so-called transfer functions that characterize flow between matrix blocks and fractures. Since Kazemi *et al.* (1976) introduced the first multiphase dual-porosity model, almost all subsequent dual-porosity models have been based on modifications of the transfer functions. These transfer functions are what distinguish various dual porosity models in the literature.

We have formulated for multiphase flow, including complex chemical phenomena currently modeled with UTCHEM for both fracture and rock matrix, e.g., the effects of reduced interfacial tension on phase trapping, surfactant adsorption, and so forth. The dual-porosity model handles the flow of tracers in both rock systems as well.

Formulation

Assumptions and formulation of the equations used in UTCHEM are covered in detail in Datta Gupta *et al.* (1986), Saad (1989), and Delshad *et al.* (1996). For consistency, the same assumptions and formulation are used for the mass-conservation equation and the pressure equation in the matrix. The major assumptions are as follows:

1. Slightly compressible fluid and rock properties.
2. Darcy's law applies.
3. Dispersion follows a generalization of Fick's law to multiphase flow in porous media.
4. Ideal mixing.
5. The fluid phase behavior is independent of the reservoir pressure.

The mass conservation equation used in UTCHEM is

$$\frac{\partial}{\partial t}\left(\phi \tilde{C}_k \rho_k\right)+\bar{\nabla}\cdot\left[\sum_{l=1}^{n_p}\rho_k\left(C_{k\ell}\,\bar{u}_\ell-\phi S_\ell\,\bar{\bar{K}}_{\kappa\ell}\cdot\bar{\nabla}C_{\kappa\ell}\right)\right]=R_k \qquad (1.1)$$

where

$\tilde{C}_{\kappa}$ = Overall volumetric concentration of component κ, L^3/L^3 PV

$C_{\kappa\ell}$ = Concentration of component □ in phase ℓ, L^3/L^3

$\bar{\bar{K}}_{\kappa\ell}$ = Dispersion coefficient tensor of component κ in phase ℓ, L^2/t

R_{κ} = Total source/sink for component κ, $m/L^3 t$

$\bar{u}_\ell$ = Volumetric flux of phase ℓ, L/t

ρ_{κ} = Density of component phase κ, m/L^3

The pressure equation is derived from the mass-conservation equation and is

$$\phi_R \, c_t \frac{\partial p_1}{\partial t} - \vec{\nabla} \cdot \bar{\bar{k}} \cdot \lambda_{rTc} \vec{\nabla} p_1 =$$

$$- \vec{\nabla} \cdot \sum_{\ell=1}^{n_p} \bar{\bar{k}} \cdot \lambda_{r\ell c} \vec{\nabla} D + \vec{\nabla} \cdot \sum_{\ell=2}^{n_p} \bar{\bar{k}} \cdot \lambda_{r\ell c} \vec{\nabla} p_{c\ell 1} + \sum_{k=1}^{n_{cv}} Q_k \qquad (1.2)$$

where

c_t = total system compressibility, Lt^2 / m
D = depth, L
$\bar{\bar{k}}$ = permeability tensor, L^2
p_ℓ = pressure of phase ℓ, Lt^2 / m
$p_{c\ell 1}$ = capillary pressure between the given phase ℓ and phase 1, Lt^2 / m
Q_k = source/sink flow for component k per bulk volume, $L^3 / L^3 t$
$\lambda_{r\ell c}$ = relative mobility, $m / L\,t$
λ_{rTc} = total relative mobility, $m / L\,t$
n_p = number of phases
n_{cv} = number of volume - occupying components

A detailed description of the variables used in both the mass-conservation and pressure equations is found in Datta Gupta *et al.* (1986), Saad (1989), and Delshad *et al.* (1996). Equations 1.1 and 1.2 may be extended to account for dual-porosity behavior by adding sink/source transfer terms to represent the matrix-fracture transfer. Another set of equations similar to Eqs. 1.1 and 1.2 is used to calculate the sink/source transfer terms. No wells are allowed to be completed in the matrix blocks at this time. We have two sets of equations: one set for the fracture system and another for the matrix block. The matrix-block set of equations is used to calculate the sink/source transfer terms used in the fracture-system set of equations. In both sets the pressure equation is solved implicitly while the mass-conservation equations are solved explicitly afterwards. The solution method decouples the matrix-pressure equation from the fracture pressure equation while solving the matrix mass-conservation equations explicitly. The decoupling procedure is discussed below. At each time level, the matrix pressure equation is solved implicitly to calculate the sink/source transfer terms. The sink/source transfer terms are then added to the fracture pressure equation, which in turn is solved implicitly. Next, the matrix mass-conservation equations are solved explicitly to calculate sink/source transfer terms that are added to the fracture mass-conservation equations that are solved explicitly as well. At the end of the timestep, both fracture and matrix variables are updated and a new timestep begins.

Discretized matrix equations

The spatial domain will be divided into nested grids in the horizontal direction and stacked grids in the vertical direction utilizing a modified MINC style (Wu and Pruess, 1986) as shown in Fig 1.1. The advantage of this approach is it reduces the problem to one dimension in the horizontal direction; the whole problem is reduced from three-dimensional problem to a two-dimensional one. Keeping this in mind, Eq. 1.1 can be expanded for each component as

$$\begin{aligned}
&\frac{\partial}{\partial t}\left\{\phi \tilde{C}_\kappa \left[1 + c_\kappa^o \left(p_\ell - p_R\right)\right]\right\} \\
&= -\frac{\partial}{\partial h}\left\{\sum_{\ell=1}^{n_p}\left[1 + c_\kappa^o \left(p_\ell - p_R\right)\right]\left(C_{\kappa\ell} u_{h\ell} - \phi S_\ell K_{hh\kappa\ell}\frac{\partial C_{\kappa\ell}}{\partial h}\right)\right\} \\
&\quad -\frac{\partial}{\partial z}\left\{\sum_{\ell=1}^{n_p}\left[1 + c_\kappa^o \left(p_\ell - p_R\right)\right]\left(C_{\kappa\ell} u_{z\ell} - \phi S_\ell K_{zz\kappa\ell}\frac{\partial C_{\kappa\ell}}{\partial z}\right)\right\} \\
&\quad + Q_\kappa
\end{aligned} \tag{1.3}$$

where the overall concentration of each component κ is given by

$$\tilde{C}_\kappa = \left(1 - \sum_{\kappa=1}^{n_c}\hat{C}_\kappa\right)\sum_{\ell=1}^{n_p} C_{\kappa\ell} S_\ell + \hat{C}_\kappa \tag{1.4}$$

where

$\hat{C}_\kappa$ = adsorbed concentration of component κ, L^3/L^3 PV
c_κ^o = compressibility of component κ, Lt^2/m
h = horizontal direction
$\bar{\bar{K}}$ = dispersion tensor, L^2/t
S_ℓ = satuaration of phase ℓ, L^3/L^3 PV
u = Darcy's flux, L/t
z = vertical direction

The porosity in the accumulation term is approximated as

$$\phi = \phi_R\left[1 + c_r\left(p_1 - p_R\right)\right] \tag{1.5}$$

where ϕ_R is the porosity at a specific pressure p_R, p_1 is the aqueous phase pressure, and c_r is the rock compressibility at p_R. Substituting the expression for rock compressibility and neglecting the terms containing the product $c_k{}^o c_r$ because they are small, we have

$$\begin{aligned} LHS = {} & \phi_R\left(c_r + c_\kappa^o\right)\frac{\partial p_1}{\partial t}\tilde{C}_\kappa^n \\ & + \phi_R\left[1 + c_\kappa^o\left(p_1 - p_R\right)^{n+1} + c_r\left(p_1 - p_R\right)^{n+1}\right]\frac{\partial \tilde{C}_\kappa}{\partial t} \end{aligned} \tag{1.6}$$

Keeping in mind that a modified MINC-style subgridding scheme is used, the spatial derivatives are evaluated as follows:

$$
\begin{aligned}
\mathrm{RHS} = {} & -\frac{2\Delta z_k}{V_{bik}} \sum_{\ell=1}^{n_p} \Big\langle u_{x\ell,i+1/2k} y_{ik} \left[1 + c_\kappa^o (p_1 - p_R)\right]_{ik} C_{\kappa\ell,i+1/2k} \\
& + u_{y\ell,i+1/2k} x_i \left[1 + c_\kappa^o (p_1 - p_R)\right]_{ik} C_{\kappa\ell,i+1/2k} \\
& - u_{x\ell,i-1/2k} y_{i-1} \left[1 + c_\kappa^o (p_1 - p_R)\right]_{i-1k} C_{\kappa\ell,i-1/2k} \\
& - u_{y\ell,i-1/2k} x_{i-1} \left[1 + c_\kappa^o (p_1 - p_R)\right]_{i-1k} C_{\kappa\ell,i-1/2k} \\
& - K_{xx} \Bigg\{ \phi_R S_\ell \left[1 + c_\kappa^o (p_1 - p_R)\right]_{ik} y_i \frac{C_{\kappa\ell,i+1k} - C_{\kappa\ell,ik}}{x_{nod,i+1} - x_{nod,i}} \\
& - \phi_R S_\ell \left[1 + c_\kappa^o (p_1 - p_R)\right]_{i-1k} y_{i-1} \frac{C_{\kappa\ell,ik} - C_{\kappa\ell,i-1k}}{x_{nod,i} - x_{nod,i-1}} \Bigg\} \\
& - K_{yy} \Bigg\{ \phi_R S_\ell \left[1 + c_\kappa^o (p_1 - p_R)\right]_{ik} x_i \frac{C_{\kappa\ell,i+1k} - C_{\kappa\ell,ik}}{y_{nod,i+1} - y_{nod,i}} \\
& - \phi_R S_\ell \left[1 + c_\kappa^o (p_1 - p_R)\right]_{i-1k} x_{i-1} \frac{C_{\kappa\ell,ik} - C_{\kappa\ell,i-1k}}{y_{nod,i} - y_{nod,i-1}} \Bigg\} \Big\rangle \\
& - \frac{1}{\Delta z_k} \sum_{\ell=1}^{n_p} \Big\langle u_{z\ell,ik+1/2} \left[1 + c_\kappa^o (p_1 - p_R)\right]_{ik} C_{\kappa\ell,ik+1/2} \\
& - u_{z\ell,ik-1/2} \left[1 + c_\kappa^o (p_1 - p_R)\right]_{ik-1} C_{\kappa\ell,ik-1/2} \\
& - 2K_{zz} \Bigg\{ \phi_R S_\ell \left[1 + c_\kappa^o (p_1 - p_R)\right]_{ik} \frac{C_{\kappa\ell,ik+1} - C_{\kappa\ell,ik}}{\Delta z_{k+1} + \Delta z_k} \\
& - \phi_R S_\ell \left[1 + c_\kappa^o (p_1 - p_R)\right]_{ik-1} \frac{C_{\kappa\ell,ik} - C_{\kappa\ell,ik-1}}{\Delta z_k + \Delta z_{k-1}} \Bigg\} \Big\rangle
\end{aligned}
\tag{1.7}
$$

In Eq. 1.7 the convection terms are evaluated using one point upstream weighting, shown in Eq. 1.7 for the case when the potential $\Phi_{i-1} > \Phi_i > \Phi_{i+1}$. Physical dispersion is modeled in the matrix blocks using a diagonal dispersion tensor. The elements of this tensor are given by

$$
K_{xxk\ell} = \frac{D_{\kappa\ell}}{\tau} + \frac{\alpha_{L\ell} u_{x\ell}^2}{\phi S_\ell |u_\ell|} + \frac{\alpha_{T\ell} u_{y\ell}^2}{\phi S_\ell |u_\ell|} + \frac{\alpha_{T\ell} u_{z\ell}^2}{\phi S_\ell |u_\ell|} \tag{1.8}
$$

$$
K_{yyk\ell} = \frac{D_{\kappa\ell}}{\tau} + \frac{\alpha_{L\ell} u_{y\ell}^2}{\phi S_\ell |u_\ell|} + \frac{\alpha_{T\ell} u_{x\ell}^2}{\phi S_\ell |u_\ell|} + \frac{\alpha_{T\ell} u_{z\ell}^2}{\phi S_\ell |u_\ell|} \tag{1.9}
$$

$$K_{zzk\ell} = \frac{D_{\kappa\ell}}{\tau} + \frac{\alpha_{L\ell} u_{z\ell}^2}{\phi S_\ell \left| u_\ell \right|} + \frac{\alpha_{T\ell} u_{x\ell}^2}{\phi S_\ell \left| u_\ell \right|} + \frac{\alpha_{T\ell} u_{y\ell}^2}{\phi S_\ell \left| u_\ell \right|} \tag{1.10}$$

where

$$\left| u_\ell \right| = \sqrt{u_{x\ell}^2 + u_{y\ell}^2 + u_{z\ell}^2} \tag{1.11}$$

and

$D_{\kappa\ell}$ = diffusion coefficient of component κ in in phase ℓ, L^2 / t

α_L, α_T = longitudinal and transverse dispersivity, L

The fluxes $u_{x\ell}$, $u_{y\ell}$ and $u_{z\ell}$ are modeled through the use of Darcy's law for multiphase flow through permeable media, which is given by

$$\bar{u}_\ell = -\bar{\bar{k}} \lambda_{r\ell} \left(\bar{\nabla} p_\ell - \gamma_\ell \bar{\nabla} D \right) \tag{1.12}$$

where

$\lambda_{r\ell}$ = relative mobility of phase ℓ, L^2 / t

γ_ℓ = specific weight of phase ℓ, $m / L^2 t$

The pressure equation, Eq. 2, can be rewritten as

$$\phi_R \, c_t \frac{\partial p_1}{\partial t} - \bar{\nabla} \cdot \sum_{\ell=1}^{n_p} \bar{\bar{k}} \cdot \lambda_{r\ell c} \bar{\nabla} p_1 = -\bar{\nabla} \cdot \sum_{\ell=1}^{n_p} \bar{\bar{k}} \cdot \lambda_{r\ell c} \bar{\nabla} D + \bar{\nabla} \cdot \sum_{\ell=2}^{n_p} \bar{\bar{k}} \cdot \lambda_{r\ell c} \bar{\nabla} p_{c1\ell} \tag{1.13}$$

Note that the sink/source term has been removed, since no wells are completed in the matrix blocks in this formulation. The finite-difference form of the left side of Eq. 1.13, using a MINC style approach, can be written as

$$\begin{aligned}\mathrm{LHS} = {} & \phi_R c_t \frac{p_{1,ik}^{n+1} - p_{1,ik}^{n}}{\Delta t} \\ & - \frac{2\Delta z_k}{V_{b,ik}} \sum_{\ell=1}^{n_p} \left[k_x \left(\lambda_{r\ell c,i+1/2k} y_i \frac{p_{1,i+1k}^{n+1} - p_{1,ik}^{n+1}}{x_{nod,i+1} - x_{nod,i}} \right.\right. \\ & \left. - \lambda_{r\ell c,i-1/2k} y_{i-1} \frac{p_{1,ik}^{n+1} - p_{1,i-1k}^{n+1}}{x_{nod,i} - x_{nod,i-1}} \right) \\ & \left.+ k_y \left(\lambda_{r\ell c,i+1/2k} x_i \frac{p_{1,i+1k}^{n+1} - p_{1,ik}^{n+1}}{y_{nod,i+1} - y_{nod,i}} - \lambda_{r\ell c,i-1/2k} x_{i-1} \frac{p_{1,ik}^{n+1} - p_{1,i-1k}^{n+1}}{y_{nod,i} - y_{nod,i-1}} \right) \right] \\ & - \frac{2}{\Delta z_k} \sum_{\ell=1}^{n_p} k_z \left(\lambda_{r\ell c,ik+1/2} \frac{p_{1,ik+1}^{n+1} - p_{1,ik}^{n+1}}{\Delta z_{k+1} + \Delta z_k} - \lambda_{r\ell c,ik-1/2} \frac{p_{1,ik}^{n+1} - p_{1,ik-1}^{n+1}}{\Delta z_k + \Delta z_{k-1}} \right) \end{aligned} \qquad (1.14)$$

The right side of Eq. 1.13 can be separated into a gravity term and a capillary-pressure term. The gravity term in the right side of Eq. 1.13 can be expanded as

$$\begin{aligned} G = {} & -\frac{2\Delta z_k}{V_{b,ik}} \sum_{\ell=1}^{n_p} \left[k_x \left(\lambda_{r\ell c,i+1/2k} \gamma_{\ell,i+1/2k} y_i \frac{D_{i+1} - D_i}{x_{nod,i+1} - x_{nod,i}} \right.\right. \\ & \left. - \lambda_{r\ell c,i-1/2k} \gamma_{\ell,i-1/2k} y_{i-1} \frac{D_i - D_{i-1}}{x_{nod,i} - x_{nod,i-1}} \right) \\ & + k_y \left(\lambda_{r\ell c,i+1/2k} \gamma_{\ell,i+1/2k} x_i \frac{D_{i+1} - D_i}{y_{nod,i+1} - y_{nod,i}} \right. \\ & \left.\left. - \lambda_{r\ell c,i-1/2k} \gamma_{\ell,i-1/2k} x_{i-1} \frac{D_i - D_{i-1}}{y_{nod,i} - y_{nod,i-1}} \right) \right] \\ & - \frac{2}{\Delta z_k} \sum_{\ell=1}^{n_p} k_z \left(\lambda_{r\ell c,ik+1/2} \gamma_{\ell,ik+1/2} \frac{D_{k+1} - D_k}{\Delta z_{k+1} + \Delta z_k} \right. \\ & \left. - \lambda_{r\ell c,ik-1/2} \gamma_{\ell,ik-1/2} \frac{D_k - D_{k-1}}{\Delta z_k + \Delta z_{k-1}} \right) \end{aligned} \qquad (1.15)$$

Equation 1.15 can be simplified by realizing that the matrix blocks are modeled as horizontal matrix blocks. Rewriting Eq. 1.15, we obtain

$$G = -\frac{1}{\Delta z_k} \sum_{\ell=1}^{n_p} k_z \left(\lambda_{r\ell c,ik+1/2} \gamma_{\ell,ik+1/2} - \lambda_{r\ell c,ik-1/2} \gamma_{\ell,ik-1/2} \right) \qquad (1.16)$$

Similarly, the capillary-pressure term in the right side of Eq. 1.13 can be expanded as

$$
\begin{aligned}
PC = \frac{2\Delta z_k}{V_{b,ik}} \sum_{\ell=2}^{n_p} \Bigg[& k_x \left(\lambda_{r\ell c,i+1/2} y_i \frac{p_{c\ell 1,i+1k} - p_{c\ell 1,ik}}{x_{nod,i+1} - x_{nod,i}} \right. \\
& \left. - \lambda_{r\ell c,i-1/2k} y_{i-1} \frac{p_{c\ell 1,ik} - p_{c\ell 1,i-1k}}{x_{nod,i} - x_{nod,i-1}} \right) \\
& + k_y \left(\lambda_{r\ell c,i+1/2k} x_i \frac{p_{c\ell 1,i+1k} - p_{c\ell 1,ik}}{y_{nod,i+1} - y_{nod,i}} \right. \\
& \left. - \lambda_{r\ell c,i-1/2k} x_{i-1} \frac{p_{c\ell 1,ik} - p_{c\ell 1,i-1k}}{y_{nod,i} - y_{nod,i-1}} \right) \Bigg] \\
& + \frac{2}{\Delta z_k} \sum_{\ell=2}^{n_p} k_z \left(\lambda_{r\ell c,ik+1/2} \frac{p_{c\ell 1,ik+1} - p_{c\ell 1,ik}}{\Delta z_{k+1} + \Delta z_k} \right. \\
& \left. - \lambda_{r\ell c,ik-1/2} \frac{p_{c\ell 1,ik} - p_{c\ell 1,ik-1}}{\Delta z_k + \Delta z_{k-1}} \right)
\end{aligned} \qquad (1.17)
$$

$\lambda_{r\ell c}$ in the above equations is evaluated using one-point upstream weighing and is given by

$$\lambda_{r\ell c} = \lambda_{r\ell} \sum_{\kappa=1}^{n_c} \left(1 + c_\kappa^o \Delta p\right) C_{\kappa\ell} \qquad (1.18)$$

For the case when the potential $\Phi_{i-1} > \Phi_i > \Phi_{i+1}$, $\lambda_{r\ell c,i-1/2}$ is evaluated at *i*-1 and $\lambda_{r\ell c,i+1/2}$ is evaluated at *I*. $\lambda_{r\ell}$ in Eq. 18 is given by

$$\lambda_{r\ell} = \frac{k_{r\ell}}{\mu_\ell} \qquad (1.19)$$

Decoupled equations

The matrix-block pressure equation will be decoupled from the fracture pressure equation to minimize coding effort (Chen, 1993). The transfer functions added to the fracture pressure equation have the form

$$\begin{aligned}
\tau_{mf} = {} & N_m \sum_{\ell=1}^{n_p} \sum_{i=1}^{N_{subh}} k_z \frac{2V_{b,iN_{subv}} \lambda_{r\ell c,iN_{subv}+1/2}}{\Delta z_{N_{subv}}} \\
& \left[\frac{p_{1m,iN_{subv}}^{n+1} - p_{1f}^{n+1} - \gamma_{\ell,iN_{subv}+1/2}\left(D_{iN_{subv}} - D_f\right)}{\Delta z_{N_{subv}}} \right] \\
& + N_m \sum_{\ell=1}^{n_p} \sum_{i=1}^{N_{subh}} k_z \frac{2V_{b,i1}\lambda_{r\ell c,i1/2}}{\Delta z_1} \left[\frac{p_{1m,i1}^{n+1} - p_{1f}^{n+1} - \gamma_{\ell,i1/2}\left(D_{i1} - D_f\right)}{\Delta z_1} \right] \\
& + N_m \sum_{\ell=2}^{n_p} \sum_{i=1}^{N_{subh}} k_z \frac{2V_{b,iN_{subv}} \lambda_{r\ell c,iN_{subv}+1/2}}{\Delta z_{N_{subv}}} \left[\frac{p_{c\ell 1,iN_{subv}} - p_{c\ell 1,f}}{\Delta z_{N_{subv}}} \right] \\
& + N_m \sum_{\ell=2}^{n_p} \sum_{i=1}^{N_{subh}} k_z \frac{2V_{b,i1}\lambda_{r\ell c,i1/2}}{\Delta z_1} \left[\frac{p_{c\ell 1,i1} - p_{c\ell 1,f}}{\Delta z_1} \right] \\
& + N_m \sum_{\ell=1}^{n_p} \sum_{k=1}^{N_{subv}} 4\Delta z_k \lambda_{r\ell c,N_{subh}+1/2k} \Big[p_{1m,N_{subh}k}^{n+1} - p_{1f}^{n+1} \\
& - \gamma_{\ell,N_{subh}+1/2,k}\left(D_{N_{subh}k} - D_f\right)\Big] \left(\frac{k_x y_{N_{subh}}}{x_{N_{subh}} - 2x_{nod,N_{subh}}} + \frac{k_y x_{N_{subh}}}{y_{N_{subh}} - 2y_{nod,N_{subh}}} \right) \\
& + N_m \sum_{\ell=2}^{n_p} \sum_{k=1}^{N_{subv}} 4\Delta z_k \lambda_{r\ell c,N_{subh}+1/2k} \left(p_{c\ell 1,N_{subh}k} - p_{c\ell 1,\ell} \right) \\
& \left(\frac{k_x y_{N_{subh}}}{x_{N_{subh}} - 2x_{nod,N_{subh}}} + \frac{k_y x_{N_{subh}}}{y_{N_{subh}} - 2y_{nod,N_{subh}}} \right)
\end{aligned} \tag{1.20}$$

where

N_m = number of matrix blocks per gridblock

N_{subh} = number of lateral matrix subgrids

N_{subv} = number of vertical matrix subgrids

The decoupling method substitutes the unknown matrix pressure in Eq. 1.20 with a function that is dependent on the fracture pressure at the next time level. The decoupling procedure is provided next.

If we solve the matrix pressure equation, Eq. 1.13, with boundary condition p_{lf}^{n}, the solution would represent how the matrix pressure changes if the boundary condition were kept constant. Let this solution be represented by

$$\phi_R \, c_t \frac{\partial \bar{p}_{1m}}{\partial t} - \vec{\nabla} \cdot \sum_{\ell=1}^{n_p} \bar{\bar{k}} \cdot \lambda_{r\ell c} \vec{\nabla} \bar{p}_{1m} = -\vec{\nabla} \cdot \sum_{\ell=1}^{n_p} \bar{\bar{k}} \cdot \lambda_{r\ell c} \vec{\nabla} D + \vec{\nabla} \cdot \sum_{\ell=2}^{n_p} \bar{\bar{k}} \cdot \lambda_{r\ell c} \vec{\nabla} p_{c\ell 1} \tag{1.21}$$

Now let

$$\tilde{p}_{1m}^{n+1} = \frac{p_{1m}^{n+1} - \bar{p}_{1m}^{n+1}}{p_{1f}^{n+1} - p_{1f}^{n}} \tag{1.22}$$

If we substitute Eq. 1.22 in the original pressure equation, Eq. 1.13, we obtain

$$\phi_R \, c_t \frac{\partial \tilde{p}_{1m}}{\partial t} - \vec{\nabla} \cdot \sum_{l=1}^{n_p} \bar{\bar{k}} \cdot \lambda_{rlc} \vec{\nabla} \tilde{p}_{1m} = 0 \tag{1.23}$$

The appropriate boundary condition for Eq. 1.23 is $\tilde{p}_1 = 1$ by evaluating Eq. 1.22 at the boundary. Note that neither Eq. 1.21 nor Eq. 1.23 have any fracture unknowns. Furthermore, p_1^{n+1} can easily be evaluated from

$$p_{1m}^{n+1} = \bar{p}_{1m}^{n+1} + \left(p_{1f}^{n+1} - p_{1f}^{n}\right)\tilde{p}_{1m}^{n+1} \tag{1.24}$$

Substituting the expression for p_{1m}^{n+1} into Eq. 20 and rearranging, we obtain

$$\begin{aligned}
\tau_{mf} = N_m \Bigg\{ p_{1f}^{n+1} \sum_{\ell=1}^{n_p} \Bigg[& \sum_{i=1}^{N_{subh}} \frac{2V_{b,iN_{subv}} k_z \lambda_{r\ell c,iN_{subv}+1/2} \left(\tilde{p}_{1m,iN_{subv}}^{n+1} - 1\right)}{\Delta z_{N_{subv}}^2} \\
& + \sum_{i=1}^{N_{subh}} \frac{2V_{b,i1} k_z \lambda_{r\ell c,i1/2} \left(\tilde{p}_{1m,i1}^{n+1} - 1\right)}{\Delta z_1^2} \\
& + \sum_{k=1}^{N_{subv}} 4\Delta z_k \lambda_{r\ell c,N_{subv}+1/2k} \left(\tilde{p}_{1m,N_{subh}k}^{n+1} - 1\right) \Bigg(\frac{k_x y_{N_{subh}}}{x_{N_{subh}} - 2x_{nod,N_{subh}}} \\
& + \frac{k_y x_{N_{subh}}}{y_{N_{subh}} - 2y_{nod,N_{subh}}} \Bigg) \Bigg]
\end{aligned}$$

$$
\begin{aligned}
&- p_{1\ell}^{n} \sum_{\ell=1}^{n_p} \Bigg[\sum_{i=1}^{N_{subh}} k_z \frac{2V_{b,iN_{subv}} \lambda_{r\ell c,iN_{subv}+1/2} \tilde{\overline{p}}_{1m,iN_{subv}}^{n+1}}{\Delta z_{N_{subv}}^{2}} \\
&+ \sum_{i=1}^{N_{subh}} k_z \frac{2V_{b,i1} \lambda_{r\ell c,i1/2} \tilde{\overline{p}}_{1m,i1}^{n+1}}{\Delta z_{1}^{2}} \\
&+ \sum_{k=1}^{N_{subv}} 4\Delta z_k \lambda_{r\ell c,N_{subh}+1/2k} \tilde{\overline{p}}_{1m,N_{subh}k}^{n+1} \Bigg(\frac{k_x y_{N_{subh}}}{x_{N_{subh}} - 2x_{nod,N_{subh}}} \\
&+ \frac{k_y x_{N_{subh}}}{y_{N_{subh}} - 2y_{nod,N_{subh}}} \Bigg) \Bigg]
\end{aligned}
$$

$$
\begin{aligned}
&+ \sum_{\ell=1}^{n_p} \Bigg[\sum_{i=1}^{N_{subh}} k_z \frac{2V_{b,iNsubv} \lambda_{r\ell c,iNsubv+1/2} \overline{p}_{1m,iN_{subv}}^{n+1}}{\Delta z_{N_{subv}}^{2}} \\
&+ \sum_{i=1}^{N_{subh}} k_z \frac{2V_{b,i1} \lambda_{r\ell c,i1/2} \overline{p}_{1m,i1}^{n+1}}{\Delta z_{1}^{2}} + \sum_{k=1}^{Nsubv} 4\Delta z_k \overline{p}_{1m,Nsubhk}^{n+1} \lambda_{r\ell c,N_{subv}+1/2k} \\
&\left(\frac{k_x y_{N_{subh}}}{x_{N_{subh}} - 2x_{nod,N_{subh}}} + \frac{k_y x_{N_{subh}}}{y_{N_{subh}} - 2y_{nod,N_{subh}}} \right) \Bigg]
\end{aligned}
$$

$$
\begin{aligned}
&- \sum_{\ell=1}^{n_p} \Bigg[\sum_{i=1}^{N_{subh}} k_z \frac{2V_{biN_{subv}} \lambda_{r\ell c,N_{subv}+1/2} \gamma_{\ell,N_{subv}+1/2} \left(D_{iN_{subv}} - D_f \right)}{\Delta z_{N_{subv}}^{2}} \\
&+ \sum_{i=1}^{N_{subh}} k_z \frac{2V_{bi} \lambda_{r\ell c,i1/2} \gamma_{\ell,i1/2} \left(D_{i1} - D_f \right)}{\Delta z_{1}^{2}} \\
&+ \sum_{k=1}^{N_{subv}} 4\Delta z_k \lambda_{r\ell c,N_{subv}+1/2k} \gamma_{\ell,N_{subv}+1/2k} \left(D_{N_{subh}k} - D_f \right) \\
&\left(\frac{k_x y_{N_{subh}}}{x_{N_{subh}} - 2x_{nod,N_{subh}}} + \frac{k_y x_{N_{subh}}}{y_{N_{subh}} - 2y_{nod,N_{subh}}} \right) \Bigg]
\end{aligned}
$$

$$
\begin{aligned}
&+\sum_{\ell=2}^{n_p}\Bigg[\sum_{i=1}^{N_{subh}} k_z \frac{2V_{biN_{subv}}\lambda_{r\ell c,iN_{subv}+1/2}\left(p_{c\ell 1,iN_{subv}}-p_{c\ell 1,f}\right)}{\Delta z^2_{Nsubv}} \\
&+\sum_{i=1}^{N_{subh}} k_z \frac{2V_{bi}\lambda_{r\ell c,i1/2}\left(p_{c\ell 1,i1}-p_{c\ell 1,f}\right)}{\Delta z_1^2} \\
&+\sum_{k=1}^{N_{subv}} 4\Delta z_k \lambda_{r\ell c,N_{subv}+1/2k}\left(p_{c\ell 1,N_{subh}k}-p_{c\ell 1,f}\right) \qquad (1.25) \\
&\left(\frac{k_x y_{N_{subh}}}{x_{N_{subh}}-2x_{nodN_{subh}}}+\frac{k_y x_{N_{subh}}}{y_{N_{subh}}-2y_{nodN_{subh}}}\right)\Bigg]\Bigg\}
\end{aligned}
$$

The transfer function given in Eq. 1.25 can be evaluated by first solving Eq. 1.21, then solving Eq. 1.23. This procedure effectively eliminates any matrix unknowns at the n+1 time level from the transfer function, which facilitates solving the fracture and matrix pressure equations separately. Once the fracture pressures are known, the matrix pressures at the n+1 time level can be evaluated using Eq. 1.24. As described above, the dual porosity model in UTCHEM adds additional subgridding to the main finite difference grid used for porous media problems. The matrix blocks are divided into smaller sections, so that the transport within the blocks can be modeled accurately. This concept is illustrated in Fig. 1.1. Matrix blocks are divided into parallelepipeds for horizontal flow and into slabs for vertical flow, as shown in Fig. 1.1.

We have tested the model and its implementation by comparing the UTCHEM results with analytical solutions of known problems, laboratory coreflood experiments, and also with the results from other simulators. These tests included (1) comparison with the analytical solution for a tracer diffusion problem in a 1D fracture system, (2) laboratory results of a tracer injection in a fractured core, and (3) comparison with the results of the commercial simulator for a waterflood in a naturally fractured reservoir. The results of the validation and verification were satisfactory and confirmed the validity of the dual porosity model and the accuracy of its implementation in the simulator. We then performed field-scale simulations of tracer test in a naturally fractured reservoir. The results are discussed in the following sections.

1.1 Comparison with the Analytical Solution for a Single-Phase Diffusion Problem

The first tests to validate the dual-porosity formulation and implementation in UTCHEM were for the transport of a partitioning tracer in a single-fracture, infinite-matrix rock where both water and oil phases were present. Tracer diffusion in the matrix blocks is 1D and normal to the fracture. Effluent tracer concentration is used as the basis for the comparison. Oil saturation was at a residual saturation of 0.2 in the fracture and zero in the matrix blocks. Tang *et al.* (1981) gives the analytical solution for the tracer in the fracture. Tang *et al.* makes the following assumptions related to the geometry and hydraulic properties of the system:

- The width of the fracture is much smaller than its length.
- Transverse diffusion and dispersion within the fracture assure complete mixing across the fracture width at all times.
- The permeability of the porous matrix is very low and transport in the matrix will be by molecular diffusion.

In the application of Tang's model to the transport of partitioning tracers, the following additional assumptions are made, and reflected in the modification of the solution given by Deeds (1999):

- The tracers do not decay significantly.
- There is no sorption of the tracers to the fracture wall or within the porous matrix.

The differential equation for tracer transport in the fracture is written as

$$\frac{\partial C_f}{\partial t} + \frac{u}{R}\frac{\partial C_f}{\partial x} - \frac{D_L}{R}\frac{\partial^2 C_f}{\partial x^2} - \frac{\phi_m D_m}{bR}\frac{\partial C_m}{\partial y} = 0 \qquad (1.26)$$

where

C_f = Concentration in the fracture

C_m = Concentration in the matrix

u = Average linear velocity in fracture

R = Retardation factor ($R = 1 + \frac{KS_o}{S_w}$)

$2b$ = Fracture width

D_L = Longitudinal dispersion coefficient for the tracer in the fracture

D_m = Diffusion coefficient for the solute in the matrix

ϕ_m = Matrix porosity

The equation for the transport of the tracer in the porous matrix can be written as

$$\frac{\partial C_m}{\partial t} - D_m \frac{\partial^2 C_m}{\partial x^2} = 0 \qquad b \le x \le \infty \tag{1.27}$$

The boundary conditions are as follows:

$$C_f(0,t) = C_o \tag{1.28}$$

$$C_f(\infty,t) = 0 \tag{1.29}$$

$$C_f(x,0) = 0 \tag{1.30}$$

where C_o is the injection tracer concentration.

The boundary conditions for Equation 1.27 are

$$C_m(b,x,t) = C_f(x,t) \tag{1.31}$$

$$C_m(\infty,x,t) = 0 \tag{1.32}$$

$$C_m(y,x,0) = 0 \tag{1.33}$$

Note that the boundary condition in Equation 1.31 expresses the coupling of Equation 1.26 for the fracture transport and Equation 1.27 for the matrix transport. Tang *et al.* use a Laplace transform approach to derive the following solution for transport in the fracture:

$$\frac{C_f}{C_o} = \frac{2\,exp(\,vx\,)}{\pi^{1/2}} \int_{l}^{\infty} exp\left[-\varepsilon^2 - \frac{v^2\,x^2}{4\,\varepsilon^2}\right] erfc\left[\frac{Y}{2T}\right] d\varepsilon \tag{1.34}$$

where

$$l = \frac{x}{2}\left(\frac{R}{D_L t}\right)^{1/2} \tag{1.35}$$

$$v = \frac{u}{2D_L} \tag{1.36}$$

$$Y = \frac{x^2 \phi_m D_m^{1/2}}{4D_L b \varepsilon^2} \tag{1.37}$$

$$T = \left(t - \frac{Rx^2}{4D_L \varepsilon^2}\right)^{1/2} \tag{1.38}$$

Table 1.1 gives the parameters for the analytical solution. Two runs were made. The first one was a continuous injection of a water tracer (Fig. 1.2), and the second one was a finite slug of water tracer followed by water for the remainder of the simulation (Fig. 1.3). The effect of subgridding of the matrix was investigated, and it was shown that the numerical solution closely matched the analytical solution with as few as eight matrix subgrids. The numerical solution improved slightly when 16 subgrids were used. No subgridding at all yielded erroneous results. Using two subgrids improved the solution significantly. As the number of subgrids increases, the quality of the numerical solution improves. Using eight subgrids seems to be a good choice considering that using more subgrids increases computation time, but as always the required gridding will depend on the problem and the desired accuracy of the solution.

1.2 Comparison with the Coreflood Results

Deeds (1999) performed several laboratory partitioning tracer experiments in Berea rocks with single fracture. The schematic of the core is given in Fig. 1.4. These experiments were the first partitioning tracer tests completed in fractured media. Berea sandstone was chosen for his study because it has low matrix permeability of about 0.1 D relative to the expected fracture permeability of greater than 100 D. Berea also has a high tortuosity of about 0.4, which ensured the possibility of significant matrix diffusion effects. Decane was used as the oil phase. A known volume of decane was injected into the fracture. Due to an order of magnitude larger entry pressure of the matrix rock compared to that of the fracture, all of the decane remained in the fracture. The decane injection was followed by water injection to create residual oil saturation in the fracture. The amount of oil left in the fracture was quantified by the difference between the injected volume and the volume that was forced out during the subsequent waterflood. The tracers were isopropyl alcohol (IPA) as the conservative tracer and hexanol as the partitioning tracer with the partition coefficient of about 5.6. The flow rate was about 0.17 mL/min. Table 1.2 gives the relevant physical properties for this experiment. Figure 1.5 shows the effluent concentration of the conservative IPA tracer. The effect of matrix diffusion on the tracer responses is evident in both tracer retardation and the late time tailing in the data. The effluent IPA concentration data were successfully matched with the UTCHEM results given in Fig. 1.5. The input parameters are listed in Table 1.2. The effluent concentration of the partitioning tracer is given in Fig. 1.6. The results of UTCHEM simulation are compared with those measured in the laboratory in Fig. 1.6. The agreement is not as good as that for the conservative tracer but still follows the trend of the experimental data remarkably well. The oil saturation in the fracture was 0.2 for this simulation.

1.3 Comparison with ECLIPSE Simulator

This verification test is based on the comparison of UTCHEM results with those of a commercial reservoir simulator, ECLIPSE (ECLIPSE 100 Reference Manual, 1997), for a slightly modified version of the Kazemi *et al.* (1976) quarter of a five-spot waterflood problem in a naturally fractured reservoir. The reservoir is 600 ft long, 600 ft wide, and 30 ft thick. It is discretized into 8x8 uniform gridblocks in the x and y directions and one 30-ft-thick gridblock in the z direction (Fig. 1.7). A shape factor of 0.0844 ft^2 was used in both UTCHEM and ECLIPSE reflecting matrix block dimensions of $10 \times 10 \times 30$ ft. The shape factor is calculated using Kazemi *et al.*'s shape factor (σ) given by the following equation:

$$\sigma = 4\left(\frac{1}{L_x^2}+\frac{1}{L_y^2}+\frac{1}{L_z^2}\right) \tag{1.39}$$

where L_x, L_y, L_z are the dimensions of the matrix blocks. The properties of matrix and fracture rocks and reservoir fluid properties are summarized in Table 1.3. Relative permeability and capillary pressure curves used for both fracture and matrix rocks are given in Figs. 1.8 and 1.9 respectively.

In order to compare the results of UTCHEM with ECLIPSE, we had to add a flag to change the way relative permeability is calculated when fluid flow is from the fracture to the matrix. In UTCHEM, the relative permeabilities at the interface when the flow is from the fracture to the matrix are evaluated by taking advantage of phase potential continuity. Therefore, the matrix relative permeability curve is evaluated at the saturation that satisfies the continuity of capillary potentials. Water phase relative permeability is then calculated using

$$k_{rw} = \left(\omega\, k_{rwm} + S_{wf}\ (1-\omega)\, k_{rwm}\left(S_{wj}\right)\right) \tag{1.40}$$

and that of the oil phase using

$$k_{ro} = \left(\omega\, k_{rom} + S_{of}\ (1-\omega)\, k_{rom}\right) \tag{1.41}$$

ω is a one point upstream weighting parameter that is equal to one when the flow is from the matrix to the fracture and equal to zero when the flow is from the fracture to the matrix. Note that S_{wj} is evaluated assuming zero capillary pressure in the fracture. Relative permeabilities when the flow is from the fracture to the matrix are multiplied by the phase saturation in the fracture to account for the partial coverage (Chen, 1993).

However, in ECLIPSE one-point-upstream weighting is used when evaluating the relative permeability at the matrix-fracture interface (ECLIPSE, 1997a). UTCHEM was then modified to allow for a similar relative permeability evaluation as follows.

$$k_{r\ell} = \omega\, k_{r\ell m} + (1-\omega)\, k_{r\ell f} \qquad \ell = w, o \tag{1.42}$$

The simulation results of production rates, cumulative oil production, and water-oil ratio are compared in Figs. 1.10 through 1.12 respectively. A close agreement is found between the results of the two simulators.

The successful validation and verification test proved that we are now ready to apply the model to field applications for processes such as partitioning interwell tracer test (PITT), polymer flood, and surfactant flood in naturally fractured reservoir.

1.4 Field-Scale Tracer Simulations

Two simulations were performed. The first run was the PITT in a fractured reservoir with one conservative tracer and one partitioning tracer with a partition coefficient of 1. The other simulation was a similar PITT but with no fractures in the reservoir. Total porosity was kept the same in both simulations. The reservoir is 600 ft long, 600 ft wide, and 30 ft thick. It is discretized into 8x8 uniform gridblocks in the x and y directions and one 30-ft-thick gridblock in the z direction (Fig. 1.7). The 8x8 grid used for the nonfractured reservoir case is the same as fracture grid in the fractured reservoir. A 4x4 matrix block was used reflecting matrix block dimensions of $10\times10\times30$ ft. The properties of matrix and fracture rocks and reservoir fluid properties are summarized in Table 1.4. The initial oil saturation was 75% with residual oil saturation value of 30% in the nonfractured reservoir, which is the same as that in the matrix block in the fractured simulation. A tracer slug of 200 days was injected at the rate of 2000 ft^3/d followed by water for 800 days for the fractured reservoir and 1800 days for the nonfractured reservoir. Note that 95% of the total porosity in the fractured reservoir is in the matrix.

The effluent tracer concentrations for the single porosity simulation are shown in Fig. 1.13. The results are typical with arrival of the conservative tracer first and lag of the partitioning tracer due to partitioning into the oil phase. At the end of the simulation, 98% of the injected conservative tracer was recovered compared to a partitioning tracer recovery of only 92%.

The tracer response in the fractured reservoir is shown in Fig. 1.14. The conservative tracer arrives first but the partitioning tracer achieves a similar peak concentration compared to that of the conservative tracer. At the end of the simulation, the recovery of the partitioning tracer of 54% was higher than that of the conservative tracer of about 47%. One explanation for higher recovery of the partitioning tracer is that more of the conservative tracer remains with the water in the matrix, while the partitioning tracer partitions into the oil and leaves with it. The effect of gravity is ignored in these simulations and the only driving mechanism for the matrix-fluid transfer is the counter-current imbibition. As a result of counter-current imbibition, water flows in the matrix but not out. The net effect is that the partitioning tracer has two mechanisms to leave the matrix block. One is diffusion through both phases and the other is convection along with the oil phase. The conservative tracer, on the other hand, can leave only by diffusion through the water phase.

1.5 Effect of Matrix Subgridding on Tracer Response Curves

As with any numerical solution, we must determine the number of gridblocks or in this case subgrids required yielding a result with acceptable accuracy. The optimum number of matrix subgrid is highly dependent on the problem to be simulated. For example, for the tracer test with no convective forces in the matrix, where the duration is short, or the diffusion coefficient is small, the tracer would penetrate only for a fraction of the distance to the center of the matrix block. For the case of incomplete penetration of the tracer into the matrix block, only the outside subgrids will be involved in meaningful calculations. If the subgrids are evenly spaced, then the inner subgrids only serve to increase the computation time required for the problem. On the other hand, for the tracer test with both convective and diffusive forces in the matrix, the matrix subgridding may not be as critical as the abovementioned case. For the purpose of simplicity, we performed 1-D simulations of a partitioning tracer test in naturally fractured reservoir to investigate the effect of matrix subgridding on the tracer response curves. A summary of the reservoir properties and the simulation input data are given in Table 1.5. The fracture initially is saturated with water and the matrix is at the oil saturation of 0.5 where the residual oil saturation is 0.3. One conservative tracer and two partitioning tracers were then injected at a rate of 250 bbls/day for a period of 20 days and it followed by water injection for about 4 years. The partitioning tracers had a partition coefficient of 5 and 10 respectively. A 4x4 matrix subgridblocks were used as the base case. The tracer response curves are given in Fig. 1.15. As expected, the tracer data are typical for partitioning tracer tests, with a relative lag of the partitioning tracer with respect to the conservative tracer. The peak tracer concentration is the highest for the conservative tracer and the lowest for the tracer with the highest partition coefficient of 10. The same simulation was repeated allowing for more refined matrix subgridblocks of up to 32 in the horizontal direction. The effect of using more horizontal subgridblocks for the matrix on the conservative tracer data is shown in Fig. 1.16 with relatively insignificant effect of the tracer tail concentration. Figure 1.17 shows the effect of matrix subgridding on the response curves for the tracer with the partition coefficient of 5. It appears that more than 4 horizontal subgrids are required for the tracer response curves to converge.

Similar simulations were performed with different number of the vertical subgrids. The number of vertical subgrids ranged from the 4 in the base case simulation to 32. Figure 1.18 indicates a lag in the peak tracer concentration as the number of subgrid increases consistent with those observed for the horizontal refinement.

1.6 Surfactant Simulation

The reservoir is 600 ft long, 600 ft wide, and 30 ft thick. It is discretized into 8x8 uniform gridblocks in the x and y directions and five 30-ft-thick layers in the z direction. Matrix block dimensions are 10×10×30 ft. Matrix blocks are subgridded by 4 in both lateral and vertical directions. The properties of matrix and fracture rocks and reservoir fluid properties are summarized in Table 1.6. Initial irreducible water saturation was 10% in the fracture and 25% in the matrix rocks. The permeability was layered with a high permeability layer in the middle at 500 md. The matrix permeability was 1 md. Water was injected at a rate of 1000 bbls/d for a period of 1500 days followed by a dilute surfactant solution injection for 100 days and then followed by water injection. The surfactant concentration was 1% mixed with a cosolvent concentration of 1%. Oil saturation profiles in fracture and matrix are shown in Figs. 1.18 through 1.23. The Oil saturation in the matrix is the average of all the matrix subgrid blocks. The channeling of the injected water through the middle high permeability layer is clear in these figures. Most of the oil recovered by waterflooding was due to the fracture and the remaining oil saturation was about 50% by the end of the 1500-day waterflood (Fig. 1.20). An average oil saturation of about 45% is remained in the matrix rocks at the end of waterflood period. The injection of dilute surfactant recovered additional oil from both fracture and matrix. The remaining oil saturation in the fracture at the end of the flood was about 10% (Fig. 1.22). The average oil saturation in the matrix was reduced from 45% to about 41% at the end of the flood (Fig. 1.23). The concentration of surfactant at the end of the flood is shown in both fracture and matrix blocks (Fig. 1.24 and Fig. 1.25). There is still significant amount of surfactant remained in the fracture after 400 days of water injection post surfactant flooding (Fig. 1.24). Figure 1.25 shows that surfactant solution has entered the rock matrix by both diffusion and convection.

SECTION 2

TASK 2: FOAM MODEL

Foams are used to increase the gas viscosity in many practical applications such as oil recovery, environmental engineering, and chemical engineering. In oil and gas reservoirs, foam has been used as a mobility control or as a blocking agent to improve the IOR flood performance or to improve acidizing operations. The essence of foam behavior is that foam reduces gas mobility, as a function of surfactant concentration, water saturation (or equivalently capillary pressure), permeability, oil saturation, and flow rate and making limiting capillary pressure a function of permeability, for modeling foam diversion between layers. Foam can be used as a blocking agent to plug high permeability lenses in heterogeneous reservoirs and divert the displacing fluids through the low permeability zones.

According to experimental observations, apparent foam viscosity is governed by its texture. Therefore, modeling of foam flow in porous media is not straightforward. Empirical mobility modification (Islam and Farouq Ali, 1990), fractional flow theory (Rossen *et al.*, 1991), compositional models (Coombe *et al.*, 1990), percolation theory, flow theory (Rossen and Gauglitz, 1990; Kharabaf and Yortsos, 1996), and population balance model (Patzek, 1988; Kovscek *et al.*, 1995) are among the methods to model foam flow in porous media.

Foam exhibits at least two steady-state flow regimes as a function of foam quality with transition occurring at a certain foam quality, f_g^*. The transition foam quality that separates the two foam regimes depends on surfactant formulation and concentration and permeability among possibly other fluid and porous media properties. To design and simulate processes using foam, there is a need for a foam model that can accommodate both foam-flow regimes. Rossen and coworkers (Cheng *et al.*, 2000) have developed a foam model for both flow regimes where the gas relative permeability is modified for the effect of foam. Cheng *et al.* (2000) provided a simple procedure to set up the simulation-input parameters for a set of steady state core flood data. The foam model incorporated in UTCHEM is based on the model of Cheng *et al.*, (2000). Although foam alters both gas relative permeability and viscosity in complex ways, for simplicity of computations, the foam model used here assigns all of the reductions of gas mobility due to foam to the gas relative permeability. In the model of Cheng *et al.*, foam forms if (1) surfactant is present and its concentration is above some threshold value, C_s^* and (2) water saturation exceeds a threshold value of S_w^*. The high quality or coalescence regime corresponds to $S_w = S_w^*$. If $S_w > S_w^*$, foam reduces gas mobility by a large constant factor; this corresponds to the low-quality regime. The models of Vassenden and Holt (1998) and in the STARS simulator (Cheng *et al.*, 2000) use a similar approach. The foam model is described as follows:

$$\text{If} \quad S_w < S_w^* - \varepsilon \text{ or } C_s < C_s^* \quad \text{then} \quad k_{rg}^f = k_{rg} \tag{2.1}$$

$$\text{If} \quad S_w^* - \varepsilon \le S_w \le S_w^* + \varepsilon \quad \text{and} \quad C_s \ge C_s^*,$$

$$\text{Then } k_{rg}^f = \frac{k_{rg}}{1 + \dfrac{(R-1)\left(S_w - S_w^* + \varepsilon\right)}{2\varepsilon}} \tag{2.2}$$

$$\text{If} \quad S_w > S_w^* + \varepsilon \text{ or } C_s \ge C_s^* \quad \text{then} \quad k_{rg}^f = \frac{k_{rg}}{R} \tag{2.3}$$

Where C_s is surfactant concentration in the aqueous phase, C_s^* is a threshold surfactant concentration for foam formation, k_{rg}^f is the effective gas relative permeability modified for foam, k_{rg} is the gas relative permeability in the absence of foam, and S_w^* and R are foam model parameters. The foam parameter R is modified according to gas flow rate to allow for shear thinning behavior of foam in low-quality regime as follows

$$R = R_{ref}\left(\frac{u_g}{u_{g,ref}}\right)^{\sigma-1} \tag{2.4}$$

Here u_g is gas volumetric flux, R_{ref} is the values of R at a reference gas volumetric flux, and σ is the conventional power-law exponent. For Newtonian foam behavior, $\sigma = 1$, and for shear thinning behavior, $\sigma < 1$.

S_w^* is the water saturation at which foam collapses. It is a function of surfactant formulation and rock properties but not a function of flow rate. The gas mobility is controlled by S_w^* in the high quality regime and by R in the low quality regime.

We have also developed a procedure to account for the effect of reservoir permeability and heterogeneity on the foam processes by estimating the critical water saturation as a function of rock permeability. As mentioned earlier, the critical water saturation (S_w^*) corresponding to critical capillary pressure is for a given rock permeability. For heterogeneous reservoir, the critical capillary pressure varies and as the consequence the foam strength varies.

The critical water saturation (S_w^*) in Equation 2.1 can be estimated by the following steps given the relative permeability – water saturation relationship. The main assumption here is that the reference data are based on the laboratory measurements of foam in the absence of oil.

1. Compute the reference water saturation, $S_{w,ref}$ at a given foam quality ($f_{g,ref}$) where the water and gas relative permeabilities are functions of water saturation.

   $$f_{g,ref} = \frac{\lambda_g}{\lambda_g + \lambda_w} = \frac{k_{rg}\,\mu_w}{k_{rg}\,\mu_w + k_{rw}\,\mu_g} \qquad (2.5)$$

   Where λ_g and λ_w are the relative mobilities of gas and water phases. k_{rg} and k_{rw} are the relative permeabilities of gas and water phases, and μ_g and μ_w are the viscosities of gas and water phases.

2. Calculate the water relative permeability at $S_{w,ref}$.

3. Calculate the water relative permeability at $S_{w,ref}^*$ using

   $$k_{rw}\left(S_{w,ref}^*\right) = \frac{k_{rw}\left(S_{w,ref}\right)}{R_{ref}} \qquad (2.6)$$

   where R_{ref} is an input parameter based on laboratory data.

4. Scale $S_{w,ref}^*$ for the new permeability using the power-law relation.

$$k_{rw}\left(S_w^*\right)=k_{rw}\left(S_{w,ref}^*\right)\left(\frac{k}{k_{ref}}\right)^b \tag{2.7}$$

where b and k_{ref} are experimentally determined parameters..

5. Calculate S_w^* based on the relative permeability calculated in Equation 2.6. The calculated S_w^* will be used as the input to the simulator. This procedure requires the knowledge of the following variables based on the laboratory experiments.

$f_{g,ref}$:	Reference foam quality
R_{ref} :	Value of R at reference conditions
k_{ref} :	Reference permeability.
b :	Exponent used for calculating S_w^*

2.1 Comparison with Published Data

The abovementioned foam model has been implemented in UTCHEM. We have history matched the results of laboratory foam corefloods to test the validity of the foam model and its implementation in UTCHEM. We then performed field-scale simulations to investigate the applicability of foam in IOR applications.

2.1.1 Data of Kibodeaux (1997)

To test and validate the model and its implementation in the code, we compared the simulation results with the coreflood results of Kibodeaux (1997). The core was an unfired Berea sandstone 24.2 cm long with a cross section of 15.6 cm^2 positioned vertically. The core had a permeability of 720 md and porosity of 0.22. The core was first saturated with water and nitrogen to a water saturation of 0.9. First the surfactant solution was injected followed by slugs of co-injection of gas and surfactant solution starting with 20% aqueous solution ($f_w = 0.2$). The injected water cut was then decreased incrementally to zero corresponding to 100% nitrogen gas injection. The injected surfactant solution was a mixture of 1 wt% sodium chloride, 0.01 wt% calcium chloride and 1 wt% surfactant. The coreflood results included the pressure drop measured across three sections of the core and along the length of the core and the average water saturation at different times. Several UTCHEM simulations were performed to simulate the experiment and match the pressure drops and average water saturations. The input foam parameters were varied to find the sensitivity of the model results to these parameters.

A comparison of the measured and simulated pressure drop as a function of pore volumes injected is shown in Fig. 2.1. The measured average water saturation is compared with the simulation results in Fig. 2.2. These preliminary results seem encouraging since the model can qualitatively mimic the behavior of foam. However, we need to simulate other experimental foam floods and enhance and fine tune the foam model as needed.

2.1.2 Data of Vassenden *et al.* (1999)

Kibodeaux performed his experiments in the absence of oil. The second and more realistic validation of the foam model in UTCHEM was done by history matching of the experimental results of Vassenden *et al.* (1999) with oil present. The foam experiments were performed in both 1-m- and 10-m-long sandpacks at the reservoir conditions of Snorre field in the North Sea. The container for the 10-m sandpack was assembled of ten 1-m-long tubes made of corrosion-resistant alloy. Here, we only focus on the history match of the results in the 1-m sandpack. The sand used in the pack was crushed Berea rock with a permeability of 7,600 md and a porosity of 0.394. Experiments were performed with the tubes oriented horizontally. The injected surfactant solution was a mixture of synthetic seawater and 0.1 wt% surfactant solution. The oil was a mixture of separator oil and gas samples from the Snorre field in the North Sea. A hydrocarbon gas mixture of 70% methane was used with a composition similar to the Snorre's separator gas. The experiments were performed at the temperature of 90° C and pressure of about 300 bars, representative of the field conditions. The surfactant solution was injected prior to the foam experiments to satisfy the surfactant adsorption. The initial water, oil, and gas saturations before the foam experiments were 0.8, 0.06, and 0.14, respectively. The foam was then injected by co-injection of water and surfactant solution. Table 2.1 gives the sequence of injection during the experiment. The pressure drop measured across the sandpack indicated regions with different foam strengths and properties. Because of the presence of both weak and strong foam regimes, we could not match the pressure drop measurements with one set of foam parameters. However, we were able to roughly match the pressure drop using different foam parameters associated with the different foam quality regions. A comparison of the measured and simulated pressure drop is given in Fig. 2.3.

2.2 Field-Scale Simulations

Two-dimensional cross-sectional simulations were performed with foams in high quality regime to investigate the significance of foam in flow divergence in a layered permeability reservoir. Table 2.2 lists the parameter values assumed in the simulations. Foam is injected in a two-layer reservoir until steady state is achieved. Both layers were initially saturated with brine at an oil saturation of 0.6 with the residual oil saturation is 0.15. There was no imposed barrier between the layers and no permeability anisotropy within the layers. The foam simulations initiated with the simultaneous injection of surfactant and gas with a foam quality of 80% and lasted for about 10 pore volumes. The surfactant concentration in the injected water was 3 vol.%. The total liquid and gas injection rate was held constant at 27.7154 ft^3/d. For the purpose of comparison, a similar simulation was performed but only 3 vol.% surfactant solution was injected with the same total rate of 27.7154 ft^3/d. Figure 2.4 compares the oil recovery as a fraction of original oil in place for both foam and surfactant simulations. Initially the surfactant flood has a higher recovery compared to that of the foam flood but due to the lack of mobility control, it leaves behind oil in the low permeability layer and the recovery at about 10 PV is about 80%. However, foam flood recovers almost all the oil from both layers since the foam blocks off the high permeability layer and the surfactant solution sweeps the low permeability layer more effectively than the surfactant flood alone. Figures 2.5 and 2.6 show the effect of foam in reducing the gas mobility quantified as the gas mobility reduction factor (parameter R) at 2 and 6 pore volumes of simultaneous gas and surfactant injection. The foam is stronger in the high permeability layers on the top with the R values in the range of 4500 compared to those in the low permeability in the range of 1500.

Oil saturation profiles are also compared in Figs. 2.7 and 2.8 at 2 PV fluid injection. Figure 2.7 indicates a better sweep efficiency with the foam injection compared to that in Fig. 2.8 with the surfactant injection. The surfactant solution sweeps the high permeability layer with very little influence on the low permeability layer when is injected with no mobility control agent such as foam or polymer. The final oil saturation profiles for both processes are given in Figs. 2.9 and 2.10.

SECTION 3

TASK 3: NUMERICAL ENHANCEMENTS

In this task, we present our accomplishments on the numerical and code enhancements of UTCHEM.

3.1 Dynamic Memory Management

The UTCHEM simulator was originally coded in FORTRAN 77, which did not allow the allocation of the memory during execution time of the simulator. We have implemented FORTRAN 90 features in the code to add dynamic memory capability. This feature allows users to run multiple data sets with different numbers of gridblocks using the same executable code. We first collected all the common blocks and the variables within these common blocks used in all subroutines and declared them in a module. The arrays are then defined as allocatable arrays. Each subroutine can then share the variables of the same module. The storage for the array is allocated when the ALLOCATE statement is executed; that is, the array becomes dynamically allocated. The allocatable array is available until it is automatically deallocated or until a DEALLOCATE statement is executed.

3.2 Flexible Gridding

In an effort to more accurately and efficiently represent complex reservoir geometries and geological features, the corner point geometry is adapted in UTCHEM. Among flexible grids such as corner point geometry, triangular grid, or Voronoi grids, the corner point geometry is the most used with the advantage of relatively simple implementation in reservoir simulators. A corner point geometry option is formulated for implementation in UTCHEM to overcome the disadvantages of the rectangular grid in simulating reservoirs with curves boundaries or fault lines. The advantages of the curvilinear grid include

- More efficient use of gridblocks, since the gridblocks no longer stretch beyond reservoir boundaries as the case for the rectangular grid. This eliminates the use of inactive gridblocks beyond the no flow boundary of the reservoir. This reduction in the total number of gridblocks translates to less CPU times.

- More accurate results since flow is perpendicular to the gridblock faces compared to a zig-zag path in rectangular grid.

The corner point geometry option is a powerful tool for construction of three-dimensional finite difference grids. It allows the user to specify the coordinates of eight corners of every gridblock. This feature is useful and essential for representing irregular reservoir boundaries, faults, and pinchouts. Effort was made in formulating the gridblock geometry such as length and width of curvilinear grid, cross-sectional areas, volumes, thickness, and center depths. The derivation of these grid properties is an extension to those for the 2-D quadrilateral (Tuma, 1979). In 3-D, each gridblock is a solid (hexahedron) defined by the location of its eight corners with vertices (corner points) $P_1(x_1,y_1,z_1)$, $P_2(x_2,y_2,z_2)$, $P_3(x_3,y_3,z_3)$, $P_4(x_4,y_4,z_4)$, $P_5(x_5,y_5,z_5)$, $P_6(x_6,y_6,z_6)$, $P_7(x_7,y_7,z_7)$, $P_8(x_8,y_8,z_8)$ as shown in Fig. 3.1a.

- Area of quadrilateral in 3D is calculated as

$$A_{3DQ} = \sqrt{A_{xy}^2 + A_{yz}^2 + A_{xz}^2} \tag{3.1}$$

where

$$A_{xy} = \frac{1}{2}\begin{vmatrix} x_1 & y_1 & 1 \\ x_2 & y_2 & 1 \\ x_3 & y_3 & 1 \end{vmatrix} + \frac{1}{2}\begin{vmatrix} x_1 & y_1 & 1 \\ x_3 & y_3 & 1 \\ x_4 & y_4 & 1 \end{vmatrix} \tag{3.1a}$$

$$A_{yz} = \frac{1}{2}\begin{vmatrix} y_1 & z_1 & 1 \\ y_2 & z_2 & 1 \\ y_3 & z_3 & 1 \end{vmatrix} + \frac{1}{2}\begin{vmatrix} y_1 & z_1 & 1 \\ y_3 & z_3 & 1 \\ y_4 & z_4 & 1 \end{vmatrix} \tag{3.1b}$$

$$A_{zx} = \frac{1}{2}\begin{vmatrix} z_1 & x_1 & 1 \\ z_2 & x_2 & 1 \\ z_3 & x_3 & 1 \end{vmatrix} + \frac{1}{2}\begin{vmatrix} z_1 & x_1 & 1 \\ z_3 & x_3 & 1 \\ z_4 & x_4 & 1 \end{vmatrix} \tag{3.1c}$$

where |. | represents the determinant of the matrix constructed using the coordinates of the gridblock.

- Volume of hexahedron can be written as

$$V_H = V_{T1235} + V_{T2348} + V_{T2358} + V_{T2568} + V_{T3578} \tag{3.2}$$

where

$$V_{T1235} = \frac{1}{6}\begin{vmatrix} x_1 & y_1 & z_1 & 1 \\ x_2 & y_2 & z_2 & 1 \\ x_5 & y_5 & z_5 & 1 \\ x_3 & y_3 & z_3 & 1 \end{vmatrix} \tag{3.2a}$$

$$V_{T2348} = \frac{1}{6}\begin{vmatrix} x_2 & y_2 & z_2 & 1 \\ x_3 & y_3 & z_3 & 1 \\ x_4 & y_4 & z_4 & 1 \\ x_8 & y_8 & z_8 & 1 \end{vmatrix} \tag{3.2b}$$

$$V_{T2358} = \frac{1}{6}\begin{vmatrix} x_2 & y_2 & z_2 & 1 \\ x_3 & y_3 & z_3 & 1 \\ x_8 & y_8 & z_8 & 1 \\ x_5 & y_5 & z_5 & 1 \end{vmatrix} \tag{3.2c}$$

$$V_{T2568} = \frac{1}{6}\begin{vmatrix} x_2 & y_2 & z_2 & 1 \\ x_5 & y_5 & z_5 & 1 \\ x_8 & y_8 & z_8 & 1 \\ x_6 & y_6 & z_6 & 1 \end{vmatrix} \tag{3.2d}$$

$$V_{T3578} = \frac{1}{6}\begin{vmatrix} x_3 & y_3 & z_3 & 1 \\ x_5 & y_5 & z_5 & 1 \\ x_7 & y_7 & z_7 & 1 \\ x_8 & y_8 & z_8 & 1 \end{vmatrix} \tag{3.2e}$$

- The centroid or block center of hexahedron, $P_c(X_c, Y_c, Z_c)$ as shown in Fig. 3.1b can be obtained as

$$X_c = \frac{1}{8}(x_1 + x_2 + x_3 + x_4 + x_5 + x_6 + x_7 + x_8) \tag{3.3a}$$

$$Y_c = \frac{1}{8}(y_1 + y_2 + y_3 + y_4 + y_5 + y_6 + y_7 + y_8) \tag{3.3b}$$

$$Z_c = \frac{1}{8}(z_1 + z_2 + z_3 + z_4 + z_5 + z_6 + z_7 + z_8) \tag{3.3c}$$

- Distance, d_{cs}, between block center of hexahedron, $P_c(X_c, Y_c, Z_c)$, and the center point of quadrilateral surface, $P_s(X_s, Y_s, Z_s)$, may be obtained as

$$d_{cs} = \sqrt{(X_c - X_s)^2 + (Y_c - Y_s)^2 + (Z_c - Z_s)^2} \tag{3.4}$$

where the centroid or the center of gravity for the quadrilateral surface is obtained from

$$X_s = \frac{1}{4}(x_1 + x_2 + x_3 + x_4) \tag{3.5a}$$

$$Y_s = \frac{1}{4}(y_1 + y_2 + y_3 + y_4) \tag{3.5b}$$

$$X_s = \frac{1}{4}(z_1 + z_2 + z_3 + z_4) \tag{3.5a}$$

- Directional vector $\vec{n}_l$ of the straight line $\overrightarrow{P_c P_s}$ is given as

$$\vec{n}_l = (\alpha_l, \beta_l, \gamma_l) \tag{3.6}$$

where the directional cosines $\alpha_l, \beta_l, and\ \gamma_l$ are calculated as

$$\alpha_l = \frac{X_c - X_s}{d_{cs}},\ \beta_l = \frac{Y_c - Y_s}{d_{cs}},\ \gamma_l = \frac{Z_c - Z_s}{d_{cs}} \tag{3.7}$$

- Angle θ between the quadrilateral surface $P_1\ P_2\ P_3\ P_4$ and the straight line $\overrightarrow{P_c P_s}$ as shown in Fig. 3.1b is given by

$$\sin\theta = \alpha_s\alpha_l + \beta_s\beta_l + \gamma_s\gamma_l \tag{3.8}$$

where $\alpha_l, \beta_l, and\ \gamma_l$ are determined from Equations 3.7. The directional cosines $\alpha_s, \beta_s, and\ \gamma_s$ of quadrilateral surface are obtained from the following expressions.

$$\alpha_s = \pm\frac{A}{\sqrt{A^2 + B^2 + C^2}},\ \beta_s = \pm\frac{B}{\sqrt{A^2 + B^2 + C^2}},\ \gamma_s = \pm\frac{C}{\sqrt{A^2 + B^2 + C^2}} \tag{3.9a}$$

where

$$A = \begin{vmatrix} y_1 & z_1 & 1 \\ y_2 & z_2 & 1 \\ y_3 & z_3 & 1 \end{vmatrix},\ B = \begin{vmatrix} z_1 & x_1 & 1 \\ z_2 & x_2 & 1 \\ z_3 & x_3 & 1 \end{vmatrix},\ C = \begin{vmatrix} x_1 & y_1 & 1 \\ x_2 & y_2 & 1 \\ x_3 & y_3 & 1 \end{vmatrix} \tag{3.9b}$$

- Perpendicular distance from the center of hexahedral gridblock, $P_c(X_c, Y_c, Z_c)$ to quadrilateral surface $P_1\ P_2\ P_3\ P_4$ as shown in Fig. 3.1b is computed by

$$d_p = d_{cs} \sin\theta \tag{3.10}$$

Substituting Equations 3.9a and 3.8 into Equation 3.10 yields

$$d_p = \frac{|(X_c - X_s)A + (Y_c - Y_s)B + (Z_c - Z_s)C|}{\sqrt{A^2 + B^2 + C^2}} \tag{3.11}$$

where A, B, and C are determined from Equation 3.9b and $|F|$ means the absolute value of the function F.

In addition, Equation 3.11 can be written as

$$d_p = \frac{|X_c A + Y_c B + Z_c C + D|}{\sqrt{A^2 + B^2 + C^2}} \tag{3.12}$$

where

$$D = \begin{vmatrix} x_1 & y_1 & z_1 \\ x_2 & y_2 & z_2 \\ x_3 & y_3 & z_3 \end{vmatrix} \tag{3.13}$$

In Cartesian coordinate system, using Equations 3.11 or 3.12 yields the half of block size.

We have made successful comparisons with Eclipse simulator using 3-D corner point grids. Figure 3.2b shows the oil saturation distribution at the end of a 30-day waterflood simulated with UTCHEM. The injection and production wells were placed in the opposite corners with a rate of 100 bbls/day. The permeability was uniform and isotropic at 300 md with a uniform porosity of 0.2. The initial water saturation was at a uniform residual water saturation of 0.37.

3.3 Graphical User Interface for Windows

We have designed a graphical user interface (UTCHEM-GUI) to set up the input, make the run, and post process the output files of the simulation. The interface is developed in a Windows (NT, 95 or higher) using Visual Basic. UTCHEM-GUI can process the well data using Microsoft Excel and output maps using either Surfer 7 software licensed from Golden Software, Inc. or Tecplot 9.0 from AMTEC Engineering Inc. A pdf version of the UTCHEM user's guide and UTCHEM technical manual are also included in the GUI. Examples of few panels of the GUI are given in Figs. 3.3 through 3.5.

We developed a graphical user interface called UTHIST for post-processing the history output files of for users who prefer running on workstations with the Unix, Linux, or Solaris operating environment and would like to take advantage of the post processing utilities. The UTHIST interface is developed in Windows environment on a PC platform using Visual Basic. The interface is also linked to Microsoft Excel. Once the well output data files are ported from the workstation to the PC and are processed using UTHIST, excel files are generated for each well for further data manipulation or graphical enhancement.

To generate the 2-D maps of output data on the PC, we have also developed an interface written in C^{++} to convert the UTCHEM output files compatible to Surfer 7 software licensed from Golden Software, Inc. Surfer is a grid-based contouring and three-dimensional surface-plotting graphics program that runs under Microsoft Windows, Windows 95, and Windows NT. The interface called UTSURF reads the output files of UTCHEM that contain data such as pressure, saturation, and species concentration and the output file that contains the grid and well data. Once the Surfer script file is executed, 2-D images of UTCHEM output files are generated. The maps will automatically include the grid, the well locations, and well names. An example of a vertical cross section of temperature distribution generated using UTSURF utility is given in Fig. 3.6.

We have also developed another interface written in C^{++} to convert the UTCHEM output files compatible to Tecplot 9.0 to generate 3-D volumetric images. Tecplot is a powerful tool for visualizing a wide range of technical data and runs on variety of computer platforms including Microsoft Windows. It offers X-Y plotting, 2- and 3-D surface plots in a variety of formats, and 3-D volumetric visualization and animation in time or space. The interface called UTPLOT reads the output files of UTCHEM that contain data such as pressure, saturation, and species concentration and the output file that contains the grid and well data. Once the Tecplot script file is executed, 2-D or 3-D images of UTCHEM output files are generated. The maps will automatically include the grid. An example of a 3-D pressure distribution generated using UTPLOT utility is given in Fig. 3.7.

We have made a major overhaul of the UTCHEM output data format in order to facilitate the graphical post processing of many of the simulation output data with our UTCHEM-GUI. Table 3.1 gives the list of additional output files that can now be processed with the UTCHEM-GUI. We have also added the capability of plotting the output data for one-dimensional simulations using Microsoft Excel.

3.4 Solvers

The discretization of the pressure equation in the UTCHEM simulator leads to a linear system of algebraic equations of the form Ax = b, where A is an n x n positive definite banded matrix, x is the vector of discrete pressures, and b is the boundary data vector. Efficient and accurate numerical solution of this system of equations is an important part of the overall solution methods for the UTCHEM simulator. Since we use large number of gridblocks in our field-scale simulations, the computational efficiency of the code requires a fast solver. The solver currently used for the solution of the pressure equation uses a Jacobi Conjugate Gradient (JCG) method. This solver has been vectorized and is very efficient on vector computers, especially on large, three-dimensional problems involving thousands of gridblocks even when simulating reservoirs with moderate to severe heterogeneities. To compare the efficiency of the existing solver in UTCHEM against other solvers on scaler computers such as PCs, we tested two solver packages coded for solving large sparse linear systems of equations that contain an implementation of various iterative methods in conjunction with the simulator. The packages that we tested are as follows:

1- PETSc, developed at Argonne National Lab. (Balay *et al.*, 1995). This solver package is available at the public domain: http//www-fp.mcs.anl.gov/petsc/.

2- NETLIB developed at the Lawrence Livermore National Laboratory. This solver package is available at the public domain: http//www.netlib.org.

We implemented the solvers in UTCHEM simulator and made several 3-D surfactant/polymer simulations with different numbers of gridblocks. The particular new solvers implemented in UTCHEM, for comparison, were JCG and Diagonally Scaled Conjugate Gradient (DSCG) from PETSc and NETLIB libraries, respectively. Table 3.2 gives a comparison of the total CPU time. The simulations were performed on Intel Pentium II 300 MHz chips. The results show that for this particular example, the existing JCG solver is the most efficient among the solvers tested.

3.5 Enhancements in the Geochemical Option

3.5.1 Solvers

UTCHEM presently handles an arbitrary number of chemical reactions involving aqueous species, including precipitation/dissolution, adsorption, ion exchange and speciation. All geochemical reactions assume local thermodynamic equilibrium. The existing geochemistry option in UTCHEM has not been optimized in terms of computational efficiency. Thus 3D simulations involving geochemical species may require hours of workstation CPU time. For example, 57% to 77% of total simulation CPU time is spent in the reaction routines for the two runs discussed below. Therefore, the practical utility of UTCHEM for problems involving geochemistry would clearly benefit from a focused effort at reducing the computational overhead in the geochemistry routines. The underlying algorithm for the geochemistry module is derived from a batch module for which run time was not a concern. In order to investigate the possibility of reduction of the computational time for the geochemical option in UTCHEM, we compared the existing routines in the simulator that solve the linear and nonlinear equations for the equilibrium calculation of species concentrations with routines from two public domain library packages. The non-linear set of equations that calculate the equilibrium concentrations of fluid chemical species, solid species, matrix adsorbed cations, and cations adsorbed on micellar surfaces are solved using the Newton method. We selected a nonlinear system solver called SNES from the PETSc library to compare with the existing nonlinear solver in UTCHEM. We also compared our solver for the systems of linear equations with a routine that uses a Gaussian elimination LU decomposition method from NETLIB library. Modifications were also made to reduce the computational efforts in the procedure for calculating the Jacobian matrix used in conjunction with the existing routine that implements the Newton method.

A summary of the two data sets used in the comparison study is given in Table 3.3. The results of this study indicated that there was not a significant improvement in computational time by using the linear and nonlinear solvers from the public domain libraries. However as shown in Tables 3.4 and 3.5, there is about 7-20% CPU reduction due to the modification of the procedure for evaluating the Jacobian matrix.

3.5.2 UTCHEM application for a field scale formation damage study

To test the generality of the geochemical model in UTCHEM we have, for the first time, simulated a field-scale waterflood to investigate the flow and transport of the barium and sulfate ions and the significance of barium sulfate precipitation. The reaction was kept simple with barium and sulfate as the reacting species and sodium, chloride, and calcium as non-reacting species. Barium sulfate was considered as the only solid precipitate with a constant solubility product of 1.4×10^{-15} at a temperature of 48 ^{o}C and pressure of 238.2 bars. The sulfate concentration in injected seawater was about 2800 ppm. With barium concentrations in the formation brine on the order of 150 ppm, large amounts of precipitation would be expected to occur. Interesting and important questions include:

- How much solid barium sulfate would precipitate if some of the sulfate were removed from the injected sea water
- How much sulfate would have to be removed from the sea water to prevent precipitation completely,
- How much of precipitation occurs in the reservoir rock and how much in the production wellbores, and
- How sensitive are the results to dispersion in the reservoir.

Conventional reservoir simulators that do not have models for geochemical reactions and often do not include physical dispersion models cannot address these questions. Three-dimensional simulations were performed with 19,360 gridblocks. Table 3.6 gives the gridblock data and Table 3.7 gives the initial reservoir and fluid properties. Four vertical injectors and 3 deviated producers were considered. The simulations were performed for a period of 10 years.

The geochemistry model in UTCHEM can model the chemical reactions among the injected chemical species and reservoir rock and fluids. The mathematical model is based on local thermodynamic equilibrium assumption. Assumptions made to develop the reaction equilibrium model are:

- All reactions attain thermodynamic equilibrium
- Activity coefficients of all reactive species are unity so that molar concentrations replace activities in reaction equilibrium calculations
- Supersaturation of aqueous species is not allowed
- Solid precipitates are stationary and can not migrate
- Equilibrium constants and solubility products are constant

Some limitations in UTCHEM reaction model worth mentioning since they can be important for the extent of barium sulfate scaling in production wells under certain reservoir conditions are as follows

- Lack of kinetic reactions. This can be important near the wellbore where the fluid rates are large and there may not be enough time for attaining equilibrium
- Once barium sulfate solid forms, it can not migrate and remains stationary
- There is no permeability reduction or pore plugging due to the barium sulfate scale in the formation
- Dependence of the solubility product on pressure has been neglected

Figure 3.8 shows the total amount of barium sulfate precipitate in all three producers as a function of both sulfate concentrations in the injected water and dispersivity. These simulations were performed with a barium concentration of 300 ppm in the formation water. The results indicate that amount of barium sulfate deposit decreases as the sulfate concentration is reduced in the injected water for any level of physical dispersion considered here. The mass of barium sulfate deposit in the wellbores is the largest in simulations with zero dispersion. Note that there is always numerical dispersion present in the simulation results but it is very small with the total-variation-third-order numerical method implemented in UTCHEM. The sensitivity to dispersion diminishes for the high sulfate concentration in seawater of 2800 ppm.

The mass of barium sulfate solid precipitate deposited in the reservoir formation is shown in Fig. 3.9. The results are for the simulations with a sulfate concentration of 120 ppm in the injected water and an initial barium concentration of 150 ppm in the formation water. The results indicate that the mass of precipitate increases as the dispersivity and thus mixing increases. There is about 2500 tons of barium sulfate deposited in the formation at the end of ten years when the moderate dispersivity of 12 m is used. These results emphasize the importance of including dispersive flux in the species conservation equation for processes that are sensitive to the amount of mixing such as the application studied here.

Examples of areal cross sections of barium, sulfate, and barium sulfate precipitate concentrations are shown in Figs. 3.10 through 3.15. The results are for simulation where the injected sulfate concentration was 200 ppm with the dispersivities of 0 and 100 m respectively. The results are shown in layer 10 of the reservoir at the end of 10 years. The maps of barium sulfate concentration show higher concentrations of precipitate and more spreading in the simulation with large physical dispersivity of 100 m (Fig. 3.11) compared to the one with zero dispersion (Fig. 3.10). The free ion sulfate concentration is more spread but with lower concentrations in the large dispersion case (Fig. 3.13) compared to the case with zero dispersion (Fig. 3.12). More barium is precipitated in the case with large dispersion (Fig. 3.15) compared to the zero dispersion case (Fig. 3.14).

Some of the conclusions from this study were as follows:

- When no sulfate is removed from the injected seawater, very large amount of solid $BaSO_4$ forms both in the reservoir and in the producers. This is true even in the absence of physical dispersion. For example, for 120 ppm sulfate about 2500 tons of barium sulfate solid were precipitated.
- The production of sulfate was substantially delayed for the simulations with the large physical dispersivity of 100 m.

- The peak concentration of barium sulfate solid was not very sensitive to either sulfate concentration or the dispersivity.

3.5.3 Development of a preprocessor for the geochemical option

We have also developed a Graphical User Interface to generate the geochemical input data. This utility is aimed to increase the user-friendliness and therefore the utilization of UTCHEM. The interface is basically a preprocessor for UTCHEM-GUI to generate the initial equilibrium data required for UTCHEM. The utility is called EQBATCH-GUI and will be linked to UTCHEM-GUI. EQBATCH-GUI will require very little input from the user and other data such as the stoichiometric coefficients and equilibrium constants will automatically be generated by the GUI. We have constructed our own database for chemical data based on the published data at a temperature of 25° C and pressure of 1 atm. Figures 3.16 through 3.18 are examples of a few panels of the EQBATCH-GUI.

SECTION 4

TASK 4. PHYSICAL PROPERTY ENHANCEMENTS

We have continued to enhance UTCHEM as in the past by adding new or revised physical and chemical property models as new or better information becomes available from our laboratories or from the literature. The physical property enhancements included relative permeability/capillary pressure models for mixed-wet reservoirs, enhancements in the current biodegradation model specific for advanced recovery methods of oil reservoirs, and extension of the trapping formulation and implementation to the gas phase for the foam simulations.

4.1 Relative Permeability and Capillary Pressure Models

It is well known that the relative permeability and capillary pressure are functions of phase saturations, saturation history, wettability, capillary number, and pore structure. Thus, it is clear that it requires an extensive laboratory effort to measure these properties to cover all scenarios. As a result, relative permeability and capillary pressure parametric models can be very useful for predicting fluid behavior in porous media. However, relative permeabilities and capillary pressures used in many oil reservoir simulators are commonly determined via interpolation between laboratory measurements. A problem with this approach is that the relations are valid only for the specific saturation path measured. Therefore, simulations of oil production using different saturation paths than that measured are likely to be in error and can limit the investigation of alternative production scenarios. We implemented a hysteretic gas relative permeability correlation for improved oil recovery processes such as foam for mobility control and improved sweep efficiency.

We also added the option of table look up for both capillary pressure and relative permeability to allow the simulation of improved oil recovery processes involving wettability alteration. The table look up option allows the user to specify multiple tables representing different wettability characteristics for the reservoir rock.

4.1.1 Hysteretic Water/Oil/Gas Relative Permeability Model

We have also incorporated a hysteretic gas relative permeability model in our existing Corey function. Here we give a brief description of the model. The three-phase oil/water/gas relative permeabilities in UTCHEM are calculated using Corey-type functions as below:

$$k_{ro} = k^{o}_{ro} \left(\frac{S_o - S_{or}}{1 - S_{or} - S_{wr} - S_{gr}}\right)^{e_o} \tag{4.1}$$

$$k_{rw} = k^{o}_{rw} \left(\frac{S_w - S_{wr}}{1 - S_{orw} - S_{wr} - S_{gr}}\right)^{e_w} \tag{4.2}$$

$$k_{rg} = k^{o}_{rg} \left(\frac{S_g - S_{gr}}{1 - S_{org} - S_{wr} - S_{gr}}\right)^{e_g} \tag{4.3}$$

where

$k_{r\ell}$ = Relative permeability of phase ℓ

$k^{o}_{r\ell}$ = Endpoint relative permeability of phase ℓ

S_{gc} = Critical gas saturation of phase

S_{ℓ} = Saturation of phase ℓ

$S_{\ell r}$ = Residual saturation of phase ℓ

S_{or} = Residual oil saturation in three-phase flow

S_{org} = Residual oil saturation to gas

S_{orw} = Residual oil saturation to water

ℓ = Phase number w: water, g: gas, o: oil

The residual oil saturation in three-phase flow (S_{or}) is calculated based on the model developed by Fayers and Matthews (1982). Both the residual water and gas saturations are assumed to be constant and input to the simulator in the original model.

$$S_{or} = f(S_g, S_w) = b * S_{orw} + (1 - b) * S_{org} \tag{4.4}$$

$$b = 1 - \frac{S_g}{1 - S_{wr} - S_{org}} \tag{4.5}$$

To incorporate the gas trapping and hysteresis in gas relative permeability, the residual gas saturation is first modified using the following expression:

$$S^*_{gr} = \frac{S_{g\max}}{1 - S_{org} - S_{wr}} S_{gr} \tag{4.6}$$

$$\text{if } S^*_{gr} \le S_{gc}\text{, then } S^*_{gr} = S_{gc} \tag{4.7}$$

This accounts for the fact that the endpoint of the gas imbibition curve will not be the residual gas saturation, S_{gr}, unless the drainage process has been carried all the way to the endpoint of the curve. Reversal of the process prior to this will cause the gas relative permeability to decline along a drainage curve that terminates somewhere between the critical gas saturation (S_{gc}) and the residual gas saturation. That value is empirically estimated here as S^*_{gr}. A second adjusted residual gas saturation, S^{**}_{gr}, is calculated as below:

$$S^{**}_{gr} = f\, S^*_{gr} + (1 - f)\, S_{gc} \tag{4.8}$$

where $f = \dfrac{S_{g\max} - S_g}{S_{g\max} - S^*_{gr}}$

This is used to smoothly interpolate from the drainage curve to the imbibition curve. As the gas saturation varies from the historical maximum in any simulation gridblock ($S_{g\max}$) to the adjusted residual gas saturation (S^*_{gr}), the value of S^{**}_{gr} varies from the critical saturation S_{gc}, to the adjusted residual value. This causes the imbibition curve to merge smoothly into the drainage curve. Once the above saturations are calculated, the adjusted gas saturation is then calculated as below:

$$S^*_g = S_{gc} + \frac{(S_g - S^{**}_{gr})(1 - S_{wr} - S_{org} - S_{gc})}{(1 - S_{wr} - S_{org} - S^*_{gr})} \tag{4.9}$$

If $S_g = S_{gmax}$ then $S_g^* = Sg$.

If $S_g = S_{gr}^*$ then $S_g^* = Sgc$

The gas relative permeability is then calculated from the gas drainage curve using the adjusted gas saturation. Thus the only input data for the simulator are drainage gas relative permeability curve and residual gas saturation. The imbibition curves are generated as described above. We have successfully incorporated and tested the model and its implementation in UTCHEM.

4.1.2 Table Look Up Option

In addition to several functional forms such as Brooks-Corey, van Genuchten, Parker, and Lenhard (Delshad *et al.*, 1999) available for relative-permeability and capillary-pressure curves, we have added the capability of table look-up for these properties. This option currently works only for two-phase oil/water flow and up to two tables can be included. These tables may represent two different wetting conditions i.e. water-wet and mixed-wet, or different rock types. We have used the table look up option for two different wetting conditions of strongly water wet and strongly oil wet conditions to simulate the imbibition of surfactant solution in an oil-wet fractured carbonate core based on the work of Chen *et al.*, 2000. Chen *et al.* Performed dilute surfactant imbibition tests for vertically oriented carbonate cores of the Yates field and found that additional oil is produced compared to brine imbibition. Wettability indices showed that dilute surfactants have shifted the wetting characteristics of the Yates rocks from oil wet to less oil-wet. The UTCHEM simulation model represents a core plug approximately 1 ft long and about 0.1 ft in diameter surrounded by fracture. The fracture contains water and surfactant solution. Matrix core plug has the initial oil saturation of 0.89 corresponding to a residual water saturation of 0.11. The residual oil saturation is 0.05. The core plug permeability is 72 md with a porosity of 0.24. The surfactant solution was allowed to spontaneously imbibe into the core plug. Initial wetting state of the core plug was assumed to be oil wet and represented by a set of relative permeability and capillary pressure tables. Figures 4.1 and 4.2 represent the capillary pressure and relative permeability relationships for the water-brine (surfactant free) flow. As surfactant solution is imbibed into the core, the wettability changes to more water wet condition. The capillary pressure and relative permeability tables will then switch to tables representing water-wet conditions once the surfactant concentration in the matrix core is above a threshold concentration. The capillary pressure and relative permeabilities representing the water-wet conditions are shown in Figs. 4.1 and 4.3. A comparison of relative permeability curves for the two wettability conditions is given in Fig. 4.4. Figure 4.5 shows the additional oil recovery due to wettability alterations in the matrix core plug by injection the surfactant solution.

4.2 Microbial Enhanced Oil Recovery Model

Microbial enhanced oil recovery (MEOR) process is based on the injection of large quantities of nutrients in the reservoir. These nutrients accelerate the growth of both the injected cultures and the indigenous microorganisms. During growth of bacteria, several metabolites such as alcohols, surfactants, and polymers are produced. Among these bio-products, surfactants, biomass, and polymers are potentially the most useful metabolic products for improved oil recovery. The oil recovery mechanisms involved in the MEOR processes include:

- Improved sweep efficiency due to selective permeability reduction
- Increased pressure and swelling of the crude oil due to the formation of gases such as CO_2
- Interfacial tension reduction and residual oil mobilization due to surfactant bio-products
- Improve sweep efficiency due to high viscosity bio-polymer formation

The MEOR implementation in UTCHEM includes the modeling of permeability reduction due to the bacterial retention by the porous medium and formation of surfactant and polymer bio-products.

UTCHEM simulates the destruction of substrates, the consumption of electron acceptors, and the growth of biomass. Substrates can be biodegraded by free-floating microorganisms in the aqueous phase or by attached biomass present as microcolonies. The model accommodates multiple substrates, electron acceptors, and biological species. Important general assumptions for the biodegradation model are listed below.

- Biodegradation reactions occur only in the aqueous phase.
- Microcolonies are fully penetrated; i.e., there is no internal resistance to mass transport within the attached biomass.
- Biomass is initially uniformly distributed throughout the porous medium.
- Biomass is prevented from decaying below a lower limit by metabolism of naturally occurring organic matter unless cometabolic reactions act to reduce the active biomass concentrations below natural levels.
- The area available for transport of oleic constituents into attached biomass is directly proportional to the quantity of biomass present.
- The number of cells per microcolony, biomass density, and microcolony volume are constant, so that mass per microcolony is also constant.
- Biodegradation reactions occur independently without mutual effects unless explicitly linked through competition or inhibition terms.
- Adsorption of biomass onto solids can be described with equilibrium partitioning.
- Chemical species within attached biomass do not adsorb to aquifer solids.

The biodegradation model has the following capabilities and features:

- Selection of Monod, first-order, or instantaneous biodegradation kinetics.
- First-order abiotic decay reactions.
- An option for external mass transfer resistances to microcolonies.
- Enzyme competition between multiple substrates.
- Inhibition of biodegradation by electron acceptors and/or toxic substrates.
- Formation of biodegradation or abiotic reaction by-products.
- Nutrient limitations to biodegradation reactions.
- Modeling of aerobic cometabolism with transformation capacities and reducing power limitations using the model of Chang and Alvarez-Cohen (1995).

The equations for a system of a single substrate, electron acceptor, and biological species are as follows.

$$\frac{dS}{dt} = -\frac{\mu_{max}X}{Y}\left(\frac{S}{K_S + S}\right)\left(\frac{A}{K_A + A}\right) - k_{abio}S \tag{4.10}$$

$$\frac{d\overline{S}}{dt} = -\frac{\mu_{max}\rho_x}{Y}\left(\frac{\overline{S}}{K_S + \overline{S}}\right)\left(\frac{\overline{A}}{K_A + \overline{A}}\right) - k_{abio}\overline{S} \tag{4.11}$$

$$\frac{dA}{dt} = -\frac{\mu_{max}XE}{Y}\left(\frac{S}{K_S + S}\right)\left(\frac{A}{K_A + A}\right) \tag{4.12}$$

$$\frac{d\overline{A}}{dt} = -\frac{\mu_{max}\rho_x E}{Y}\left(\frac{\overline{S}}{K_S + \overline{S}}\right)\left(\frac{\overline{A}}{K_A + \overline{A}}\right) \tag{4.13}$$

$$\frac{dX}{dt} = \mu_{max}X\left(\frac{S}{K_S + S}\right)\left(\frac{A}{K_A + A}\right) - bX \tag{4.14}$$

$$\frac{d\overline{X}}{dt} = \mu_{max}\overline{X}\left(\frac{\overline{S}}{K_S + \overline{S}}\right)\left(\frac{\overline{A}}{K_A + \overline{A}}\right) - b\overline{X} \tag{4.15}$$

where

$\underline{S}$ = aqueous phase substrate concentration (ML^{-3})
S = substrate concentration in attached biomass (ML^{-3})
$\underline{A}$ = aqueous phase electron acceptor concentration (ML^{-3})
A = electron acceptor concentration in attached biomass (ML^{-3})
$\underline{X}$ = aqueous phase (unattached) biomass concentration (ML^{-3})
X = attached biomass concentration; mass of attached cells per volume of aqueous phase (ML^{-3})
μ_{max} = maximum specific growth rate (T^{-1})
E = mass of electron acceptor consumed per mass of substrate biodegraded
ρ_x = biomass density; mass of cells per volume of biomass (ML^{-3})
Y = yield coefficient; mass of cells produced per mass of substrate biodegraded
K_S = substrate half-saturation coefficient (ML^{-3})
K_A = electron acceptor half-saturation coefficient (ML^{-3})
k_{abio} = first-order reaction rate coefficient (for abiotic decay reactions, T^{-1})
b = endogenous decay coefficient (T^{-1})
t = time (T)

Equation 4.10 describes mechanisms for loss of substrate in the aqueous phase. Equation 4.11 describes the loss of substrate within attached biomass and is written for a single microcolony (Molz *et al.*, 1986). Equations 4.12 and 4.13 describe the loss of the electron acceptor. Equations similar to Eqs. 4.10 and 4.11 are written for all other chemical species participating in biodegradation reactions. Equations 4.14 and 4.15 describe the growth and decay of unattached and attached biomass, respectively.

4.2.1 Permeability Reduction

The permeability reduction from biomass growth is very complex and is a very active field of investigation. Current models are either very simple, such as the Carman-Kozeny equation relating permeability reduction to reductions in porosity, or very complex. The more complex models relate permeability reduction to pore-size distributions or other characteristics of the porous medium. In general, the more complex models predict permeability reductions better than do the simple models. However, the complex models require a large number of medium-specific parameters and are very computationally intensive. Therefore, for this work, the Carman-Kozeny equation is currently being used to describe permeability reductions resulting from biomass growth. Other options considered required excessive computational effort and were not practical for field-scale applications. The Carmen-Kozeny equation incorporated in the model is

$$k = \frac{d_p^2 \, \phi^3}{300\,(1-\phi)^2} \tag{4.16}$$

where

k = permeability

ϕ = porosity

d_p = average particle size diameter

When significant biomass growth occurs, then the porosity will be reduced, with a concomitant reduction in permeability. Porosity and permeability reductions are most likely to occur near injection wells. UTCHEM accounts for both porosity and permeability reductions. Permeability is recalculated at every gridblock and time step according to the Carmen-Kozeny equation (Wilkins *et al.*, 1995):

$$k = k_{ini} \frac{(1-\phi_{ini})^2}{\phi_{ini}^3} \frac{\phi^3}{(1-\phi)^2} \tag{4.17}$$

where

k = reduced permeability due to biomass growth

k_{ini} = initial permeability

ϕ = reduced porosity due to biomass growth

ϕ_{ini} = initial porosity

4.2.2 Comparison of UTCHEM Biodegradation Model to Analytical Solution

Complete flow and biodegradation model solutions were compared to analytical and literature solutions to ensure that the simultaneous transport and biodegradation of substrates and electron acceptors produced reasonable results. Because Monod kinetics is nonlinear, only first-order (in substrate only) kinetics could be compared to analytical solutions. Figure 4.6 compares the UTCHEM solution to the analytical solution for the first-order decay of a substrate injected at a constant rate and concentration in a laboratory column. The analytical solution is solution number C14 of van Genuchten and Alves (1982), with a third-type boundary condition at the column entrance and a semi-infinite second-type boundary condition at the column exit. The flow and reaction rate parameters for this simulation are shown in Table 4.1. UTCHEM results very closely matched the analytical solution.

4.2.3- Comparison of UTCHEM Biodegradation Model to the Other Models

One-dimensional, single-phase simulations were also compared to biodegradation model solutions published by Molz *et al.* (1986). The flow and biodegradation reaction parameters for these simulations are given in Table 4.2. Figure 4.7 illustrates the comparison. The model predictions are not exactly the same because of slightly different assumptions about biomass decay, electron acceptor utilization, and adsorption. The boundary conditions are also different in the two models. However, UTCHEM is able to generally reproduce the results of the Molz model, indicating that the combined UTCHEM flow and biodegradation model is functioning properly.

4.2.3 MEOR Model Validation against Coreflood Results

To test and validate the MEOR model and its implementation in the code, we compared the simulation results with the coreflood results of Silfanus (1990). The core used in the coreflood number C06 was Berea sandstone, 2 in diameter and 6 in long, placed in the oven at a constant temperature of 35^0 C. Oil, brine and samples of microorganisms were from Southeast Vasser Vertz Sand Unit, Payne County in Oklahoma. The core had a permeability of 526 md to the field brine and porosity of 0.22. The core was initially flooded with Vertz brine with 15% NaCl salinity with nitrogen to minimize oxygen content. The core was then flooded with the Vertz crude oil to residual water saturation and then followed by brine to residual oil saturation. After these steps, the core was treated with one or several incubations of bacteria indigenous to the Vertz sand unit. The bacterial population was enriched by adding 1% molasses and 0.3% ammonium nitrate to the brine. The nutrient amended brine was incubated until growth occurred. The core was then allowed to produce fluids due to pressure buildup during incubation. The core was then flooded with another injection of nutrients. One treatment is referred to three steps of incubation, production, and injection. Table 4.1 summarized the core data.

The coreflood results included cumulative oil recovery, brine flow rates, and the pressure drop across the core to determine the effective brine permeability. The effective permeability reduction factor (PRF) was defined as the ratio of the brine permeability during each treatment to that at residual oil saturation. Several UTCHEM simulations were performed to simulate the experiment and match the oil recovery and PRF. Table 4.2 summarizes the simulation input parameters. A comparison of the measured and simulated permeability reduction factor is shown in Fig. 4.8. The measured oil recovery is compared with the simulation results in Fig. 4.9. These results seem encouraging since the model can qualitatively mimic the oil recovery mechanisms occurring during the MEOR process.

SUMMARY

Our past DOE sponsored research resulted in the development of a chemical flooding simulator UTCHEM, which is widely used for a variety of applications ranging from surfactant flooding to partitioning tracer simulations. We have continued to develop UTCHEM and make it more useful with features that are widely needed not only for chemical flooding IOR but also for a variety of other important applications such as chemical well treatments for water management and partitioning tracers for estimating remaining and bypassed oil saturation. Recent enhancements include the implementation of a mechanistic foam model for mobility and profile control during surfactant flood, a biodegradation model for MEOR processes, and a multiphase and multicomponent dual porosity model for chemical flooding of naturally fractured reservoirs. We have successfully incorporated and tested these models and their implementations in UTCHEM. A major accomplishment of this project was the development of a user friendly graphical interface (UTCHEM-GUI) to set up the input file, to make the simulation, and to process the output files all on the Windows Pcs.

UTCHEM source code and the documents became available for download at our CPGE web page http://www.pe.utexas.edu/cpge/UTCHEM/ in October 2000 and since then more than 100 individuals have downloaded the code. The UTCHEM-GUI was also made available for download in May 2002.

REFERENCES

Al-Lawati, S. and S. Saleh: "Oil Recovery in Fractured Oil Reservoirs by Low IFT Imbibition Process," paper SPE 36688 presented at the 1996 Society of Petroleum Engineers Annual Technical Conference and Exhibition, Denver, CO, Oct. 6-9.

Austad, T.: "An Evaluation of Using Surfactants in Order to Improve the Oil Recovery from the Ekofisk Chalk Formation by Water Imbibition," paper presented at the RUTH Seminar, Stavanger, Norway, September 5-6, 1994.

Balay, S., W. Gropp, L.C. McINnes, and B. Smith: PETsc 2.0 User's Manual, Math. And Computer Sci., Argone National Lab., IL (Nov. 1995).

Barenblatt, G.E., I.P. Zheltov, and I.N. Kochina: "Basic Concepts in the Theory of Homogeneous Liquids in Fissured Rocks," *J. Appl. Math. Mech.* (USSR) (1960) **24** (5), 852.

Chang, H. and L. Alvarez-Cohen: "Model for the Cometabolic Biodegradation of Chlorinated Organics," *Environmental Science and Technology*, **29**, No. 9, 2357, (1995).

Chen, J.: "New Approaches to Dual Porosity Modeling of water Flooding in Naturally Fractured Reservoirs," Ph.D. dissertation, The U. Of Texas, Austin (1993).

Chen, H.L., L.R. Lucas, A.D. Nogaret, H.D. Yang, and D.E. Kenyon: "Laboratory Monitoring of Surfactant Imbibition Using Computerized Tomography," paper SPE 59006, presented at the 2000 SPE International Conference and Exhibition, Villahermosa, Mexico, 1-3 February 2000.

Cheng, L., A.B. Rame, D. Shan, D.A. Coombe, and W.R. Rossen: "Simulating Foam Processes at High and Low Foam Qualities," paper SPE 59287, presented at the 2000 SPE/DOE Symposium on Improved Oil Recovery, Tulsa, OK, 3-5 April.

Coombe, D. and V. Oballa: "Foam Modeling Based on Lamellae as a Dispersed Component," CMG report 90.08.T, (1990).

de Blanc, P.C.: "Development and Demonstration of a Biodegradation Model for Non-Aqueous Phase Liquids," Ph.D. dissertation, The University of Texas at Austin, (1999).

Datta Gupta, A. G.A. Pope, K. Sepehrnoori, and R.L. Thrasher: "A Symmetric, Positive Definite Formulation of A Three Dimensional Micellar/Polymer Simulator," *SPE Reservoir Eng.* (1986) 1(6), 622-632.

Deeds, N.E.: "Development and Evaluation of Partitioning Interwell Tracer Test Technology for Detection of Non-Aqueous Phase Liquids in Fractured Media," Ph.D. dissertation, The University of Texas at Austin (Aug. 1999).

Delshad, M, R.J. Lenhard, M. Oostrom, G.A. Pope, and S. Yang, "A Mixed-Wet Hysteretic Relative Permeability and Capillary Pressure Model in a Chemical Compositional Reservoir Simulator," SPE 51891 Proceedings of the 1999 SPE Reservoir Simulation Symposium, Houston, TX, 14-17 February.

Delshad, M. G.A. Pope and K. Sepehrnoori: "A Compositional Simulator for Modeling Surfactant Enhanced Aquifer Remediation 1. Formulation," *J. of Contaminant Hydrology* (1996) **23**, 303-327.

ECLIPSE 100 Reference manual (97a), Schlumberger Geoquest, Geoquest Reservoir Technologies, Houston, TX (1997).

Fayers, F.J. and J.P. Mattews: "Evaluation of Normalized Stone's Methods for Estimating Three-Phase Relative Permeabilities," *SPEJ* **24** (1982), 224-232.

Islam, M.R. and S.M. Farouq Ali: "Numerical simulation of foam flow in Porous Media," J. Can. Petrol. Technol., 47-51, (July-Aug. 1990).

Kazemi, H., L.S. Merrill, Jr., K.L. Porterfield, and P.R. Zeman: "Numerical Simulation of Water-Oil in Naturally Fractured Reservoirs," *Soc. Pet. Eng. J.* (December 1976), 317-326

Keijzer, P.P.M., and A.S. de Vries: "Imbibition of Surfactant Solutions," Paper SPE/DOE 20222 presented at the 7th Symposium on EOR, Tulsa, OK, April 22-25, (1990).

Kharabaf, H. and Y.C. Yortsos: "A Pore-Network Model for Foam Formation Propagation in Porous Media," paper SPE 36663, presented at the 1996 SPE Annual Technical Conference and Exhibition, Denver, Colorado, 6-9 October.

Khatib, Z.I., G.J. Hirasaki, and A.H. Falls: "Effects of Capillary Pressure on Coalescence and Phase Mobilities in Foams Flowing Through Porous Media," *SPE Reser. Eng.*, **3**(3), 919-926 (August 1988).

Kibodeaux, K.R: "Experimental and Theoretical Studies of Foam Mechanisms in Enhanced Oil Recovery and Matrix Acidization Applications," Ph.D. dissertation. The University of Texas at Austin (Aug. 1997).

Kovscek, A.R., T.W. Patzek, and C.J. Radke: "A Mechanistic Population Balance Model for Transient and Steady-State Foam Flow in Boise Sandstone," *Chem. Eng. Sc.*, 50, **23**, 3783-3799, (1995).

Logan, B.E., D.G. Jewett, R.G. Arnold, E.J. Bouwer, and C.R. O'Melia: "Clarification of Clean-Bed Filtration Models," *Journal of Environmental Engineering* (December 1995) **121**(12), 869-873.

Molz, F. J., M. A. Widdowson, and L. D. Benefield: "Simulation of Microbial Growth Dynamics Coupled to Nutrient and Oxygen Transport in Porous Media," *Water Resources Research*, **22**, No. 8, 1207, (August 1986).

Patzek, T.W.: "Description of Foam Flow in Porous Media by Population Balance Method," *Surfactant Based Mobility Control Progress in Miscible Flood*

Enhanced Oil Recovery, Smith D.H. (ed.), ACS Symposium Series No. 373, 326-341, (1988).

Pope, G.A., K. Sepehrnoori, and M. Delshad: "Development of an Improved Simulator for Chemical and Microbial IOR Methods," First Annual Report prepared for U.S. Department of Energy, Contract No. DE-AC26-98BC15109, Sept. 2000.

Rajagopalan, R. and C. Tien: "Trajectory Analysis of Deep-Bed Filtration with the Sphere-in-cell Porous Media Model," AIChE *Journal* (May 1976) **22**(3), 523-533.

Rossen, W.R. and P.A. Gauglitz: "Percolation theory," paper SPE 22627 presented at the 66th Annual Technical Conference, Dallas, Texas, 1991.

Rossen, W.R., Z.H. Zhou, and C.K. Mamun: "Modeling Foam Mobility in Porous Media," paper SPE 22627 presented at the 66th Annual Technical Conference, Dallas, Texas, (1991).

Rossen, W.R., S.C. Zeilinger, J.-X. Shi, and M.T. Lim: "Mechanistic Simulation of Foam Processes in Porous Media," paper 28940 presented at the 1994 Annual Technical Conference and Exhibition, New Orleans, LA, September 26-28.

Saad, N.: "Field Scale Simulation of Chemical Flooding," Ph.D. dissertation. The University of Texas at Austin (1989).

Schechter, D.S., D. Zhou, and F.M. Orr: "Capillary Imbibition and Gravity Segregation in Low IFT Systems," paper SPE 22594 presented at the 66th Society of Petroleum Engineers Annual Technical Conference, Dallas, TX, Oct. 6-9, (1991).

Silfanus, N.J.: "Microbial Mechanisms for Enhanced Oil Recovery from High Salinity Core Environments," M.S. Thesis, University of Oklahoma, Norman, Oklahoma (1990).

Tang, D.H., E.O. Frind, and E.A. Sudicky: "Contaminant Transport in Fractured Porous Media: Analytical Solution for Single Fracture," *Water Resources Research* **17**(3), 555-564, (1981).

Tuma, J.J.: "Engineering Mathematics Handbook," McGraw -Hill, Inc., New York, (1979).

van Genuchten, M.T. and W.J. Alves: "Analytical Solution of the One-Dimensional Convection-Dispersion Solute Transport Equation," U.S. Department of Agriculture Technical Bulletin 1161.

Vassenden, F., T. Holt: "Experimental Foundation for Relative Permeability Modeling of Foam," paper .SPE 39660 presented at the 1998 SPE/DOE IOR Symposium, Tulsa, O.K., 19-22 April.

Vassenden, F., T. Holt, A. Ghaderi, and A Solheim: "Foam Propagation on Semi-Reservoir Scale," *SPE Reservoir Eval. & Eng.* **2**(5), 436-441, (Oct. 1999).

Warren, J.E. and P.J. Root: "The Behavior of Naturally Fractured Reservoirs," *Soc. Pet. Eng. J.* (Sept. 1963).

Wilkins, M.D., L.M. Abriola, and K.D. Pennell: "An Experimental Investigation of Rate-limited Nonaqueous Phase Liquid Volatilization in Unsaturated Porous Media: Steady State Mass Transfer," *Water Resources Research* 31(9), 2159-2172, (Sept. 1995).

Wu, Y.S. and K. Pruess: "A Multiple-Porosity Method for Simulation of Naturally Fractured Reservoir," paper SPE 15129 presented at the 1986 Soc. Pet. Eng. California Regional Meeting, Oakland, CA, April 2-4.

TABLES

Table 1.1. Parameters for Tang's analytical solution and UCHEM

Parameter	Analytical Solution	UTCHEM Input
Length	60 cm	1.969 ft
Width	5.0 cm	0.164 ft
Height	5.0 cm	0.164 ft
Retardation Factor, R	2.25	
Oil saturation		0.2
Tracer partition coefficient		5
Fracture spacing (2b)	0.027535	
Porosity		0.00688371
Velocity, u	0.0206 cm/s	58.337 ft/d
Flow rate, q	0.17 cc/min	0.00864503 ft^3/d
Slug size	3.2 cc	0.013 d
Dispersivity	0.6 cm	0.02 ft
Diffusion coefficient (D_L)	0.012348 cm^2/sec	1.148 ft^2/d
D_e	1.66×10^{-6} cm^2/sec	0.00015424 ft^2/d
No. of gridblocks	50	50

Table 1.2. Parameters for Coreflood and UTCHEM

Parameter	Experiment	UTCHEM Input
Length	60 cm	1.97 ft
Width	undefined	0.16 ft
Height	undefined	0.16 ft
Oil saturation	---	0.2
Aperture, cm	0.028	--
Fracture porosity	--	0.009
Flow rate, q	0.17 cc/min	0.00865 ft^3/d
Slug size	3.2 cc	0.013 d
Dispersivity	---	0.015 ft
Diffusion coefficient (D_L)	0.009576 cm^2/sec	---
D_e	2.18×10^{-6} cm^2/sec	2.03×10^{-3} ft^2/d
No. of gridblocks	100	100

Table 1.3. Input parameters used for the quarter-five-spot waterflood

Property	Value
Fracture porosity	0.01
Fracture irreducible water saturation	0
Fracture residual oil saturation	0
Fracture permeability	500.0 md
Matrix porosity	0.19
Matrix irreducible water saturation	0.25
Matrix residual oil saturation	0.30
Matrix permeability	1.0 md
Pore compressibility	3.0×10^{-6} psi^{-1}
Water compressibility	3.0×10^{-6} psi^{-1}
Oil compressibility	1.0×10^{-5} psi^{-1}
Water specific weight	0.4444 psi/ft
Oil specific weight	0.3611 psi/ft
Water viscosity	0.5 cp
Oil viscosity	2.0 cp
Injection rate	200 bbls/d

Table 1.4. Input parameters used for the quarter-five-spot tracer test

Property	Value
Fracture porosity	0.01
Fracture irreducible water saturation	0.10
Fracture residual oil saturation	0.0
Fracture permeability	100.0 md
Matrix porosity	0.19
Matrix irreducible water saturation	0.25
Matrix residual oil saturation	0.30
Matrix permeability	10 md
Pore compressibility	3.0×10^{-6} psi^{-1}
Water compressibility	3.0×10^{-6} psi^{-1}
Oil compressibility	1.0×10^{-5} psi^{-1}
Water specific weight	0.4444 psi/ft
Oil specific weight	0.3611 psi/ft
Water viscosity	0.5 cp
Oil viscosity	2.0 cp
Injection rate	2000 ft^3/d

Table 1.5. Input parameters used for the matrix subgridding study

Property	Value
Reservoir size	640 ft x 80 ft x 30 ft
Reservoir gridblock size	80 ft x 80 ft x 30 ft
No. of reservoir gridblocks	8 x 1 x 1
Matrix gridblock size	10 ft x 10 ft x 10 ft
No. of matrix gridblocks in each reservoir block	8 x 8 x 1
No. of matrix subgridblocks	4 x 4 (base case)
Fracture permeability	500 md
Matrix permeability	10 md
Fracture porosity	0.01
Matrix porosity	0.19
Initial oil saturation in fracture	0.0
Residual oil saturation in fracture	0.0
Residual water saturation in fracture	0.1
Residual oil saturation in matrix	0.5
Residual oil saturation in matrix	0.30
Residual water saturation in fracture	0.25
Tracer molecular diffusion coefficient	$1.54\text{x}10^{-4}$ ft^2/d
Injection rate	250 bbls/day
Tracer slug size	20 days

Table 1.6. Input parameters used for the quarter-five-spot surfactant flood

Property	Value
Fracture porosity	0.01
Fracture irreducible water saturation	0.1
Fracture residual oil saturation	0
Fracture permeability	100 md in layers 1, 2, 4, 5 500 md in layer 3
Matrix porosity	0.19
Matrix irreducible water saturation	0.25
Matrix residual oil saturation	0.30
Matrix permeability	1.0 md
Pore compressibility	$3.0\text{x}10^{-6}$ psi^{-1}
Water compressibility	$3.0\text{x}10^{-6}$ psi^{-1}
Oil compressibility	$1.0\text{x}10^{-5}$ psi^{-1}
Water specific weight	0.4444 psi/ft
Oil specific weight	0.3611 psi/ft
Water viscosity	0.5 cp
Oil viscosity	2.0 cp
Injection rate	1000 bbls/d

Table 2.1. Injection strategy used in the foam experiment of Vassenden *et al.* (1999)

Foam quality	**Time (days)**	**Gas flow rate (cc/h)**	**Water flow rate (cc/hr)**	**Gas vel. (cm/d)**	**Water vel. (cm/d)**
1.0	0-1	5	0.0	121.34	0.0
0.95	1-10.5	5	0.26	121.34	6.4
0.90	10.5-12.5	5	0.55	121.34	13.04
0.80	12.5-16.5	5	1.25	121.34	30.49
0.60	16.5-20	5	3.33	121.3	80.79

Table 2.2. Input parameter for 2-D Foam simulations

Property	**Value**
No. of gridblocks (x,y,z)	10 x 1 x 10
Gridblock size, ft	3 x 3 x 0.3
Horizontal permeability in layers 1-5, md	750
Horizontal permeability in layers 6-10, md	130
Porosity	0.25
Initial Pressure, psi	2000
Initial oil saturation	0.6
Const. Pressure at the production wells, psi	2000
Water viscosity, cp	0.7116
Oil Viscosity, cp	4
Gas Viscosity, cp	0.02286
Injected Surfactant concentration, vol %	3
Surf. Solution injection rate, ft^3/d	5.543
Gas injection rate, ft^3/d	22.1724
Foam parameters	
C_s^*	1/2 injected surfactant concentration
R_{ref}	15000
ε	0.01
σ	1
S_w^* in layers 1-5	0.37
S_w^* in layers 6-10	0.43

Table 3.1. List of new output files

Property	Output file name
Reservoir permeability and porosity	PERM
Relative permeability	RPERM
Trapping number and interfacial tension	TRAP
Geochemical-related data	ALKP
Microbial-related data	BIOD
Foam-related data	FOAM
Nonequilibrium mass transfer	DISS
Hysteresis-related data	HYST
Gel-related data	GFILEP
Temperature	TEMPP
Viscosity	VISC
Species conc. in the aqueous phase	COMP_AQ
Species conc. in the oleic phase	COMP_OIL
Species conc. in the microemulsion phase	COMP_ME
Average component concentration in matrix blocks	CONCPM
Average phase saturation in matrix blocks	SATPM
Average phase pressure in matrix blocks	PRESPM
Component concentration in matrix subgrid blocks	MATCON
Phase saturation in matrix subgrid blocks	MATSAT
Phase pressure in matrix subgrid blocks	MATPRES

Table 3.2: Summary of UTCHEM execution times using several solver packages

Solver	Execution Times, Seconds		
	1000 gridblocks (10x10x10)	5000 gridblocks (25x20x10)	10,000 gridblocks (40x25x10)
UTCHEM – JCG	946	43,280	231,816
PETSc - JCG	938	47,235	276,057
NETLIB-DSCG	1,270	43,346	245,987

Table 3.3: Summary of input for geochemical simulations

Description	Simulation Number	
	EX07	EX45
No. of gridblocks	19x19x3	100
No. of components	11	15
No. of reacting elements	7	12
No. of fluid species	18	51
No. of solid species	4	7
No. of adsorbed species	4	0
Simulation time, days	251	150

Table 3.4: Summary of UTCHEM execution times (seconds) for geochemical simulations on DEC-alpha 550 workstation

Method	**Execution Times on DEC-alpha (seconds)**	
	Run EX07	Run EX45
Newton (original UTCHEM)	3435	45
Newton (modified Jacobian)	3202	37

Table 3.5: Summary of UTCHEM execution times (seconds) for geochemical simulations on 300 MHz Intel Pentium

Method	**Execution Times on DEC-alpha (Seconds)**	
	Run EX07	Run EX45
Newton (original UTCHEM)	4711	91
Newton (modified Jacobian)	4366	73

Table 3.6. Summary of geochemical simulation input data

Number of gridblocks	22 x 40 x 22 (19,360)
Gridblock sizes, m	$\Delta x = 200$
	$\Delta y = 200$
	Layer 1: $\Delta z = 7.58$
	Layer 2: $\Delta z = 7.58$
	Layer 3: $\Delta z = 7.618$
	Layer 4: $\Delta z = 7.618$
	Layer 5: $\Delta z = 7.668$
	Layer 6: $\Delta z = 7.668$
	Layer 7: $\Delta z = 4.13$
	Layer 8: $\Delta z = 4.138$
	Layer 9: $\Delta z = 4.130$
	Layer 10: $\Delta z = 4.185$
	Layer 11: $\Delta z = 4.185$
	Layer 12: $\Delta z = 4.1935$
	Layer 13: $\Delta z = 8.472$
	Layer 14: $\Delta z = 8.472$
	Layer 15: $\Delta z = 9.658$
	Layer 16: $\Delta z = 9.658$
	Layer 17: $\Delta z = 4.849$
	Layer 18: $\Delta z = 4.849$
	Layer 19: $\Delta z = 4.815$
	Layer 20: $\Delta z = 4.814$
	Layer 21: $\Delta z = 9.22$
	Layer 22: $\Delta z = 9.22$

Table 3.7. Rock and fluid properties used in the geochemical simulations

Property	Value
Rock compressibility, 1/kPa	$4\text{x}10^{-6}$ (P_{ref} : 268 bars)
Water density, g/cc	1.15
Water viscosity, cp	0.65135
Water formation volume factor, rm^3/sm^3	1.02
Water compressibility, 1/kPa	$4.7\text{x}10^{-7}$
Oil density, g/cc	0.9234
Oil viscosity, cp	6.3
Oil formation volume factor, rm/sm^3	1.14
Oil compressibility, 1/kPa	$5\text{x}10^{-5}$
Original oil in place, m^3	$38\ \text{x}10^6$
Pore volume, m^3	$123\text{x}10^6$
Initial average reservoir pressure, bars	238.2
Temperature, °C	48

Table 4.1. Flow Parameters for the Solution of the 1-D Advection-Dispersion Equation

Property	Value
Average velocity, v (m/d)	1.0
Porosity, ϕ	0.38
Bulk soil density, ρ_b (g/cm^3)	1.64
Longitudinal dispersivity, α_L (m)	0.1
Substrate injection concentration, S_0 (mg/L)	1.0
Column length, L (m)	2.0
Number of grid blocks	25
Numerical time step (d)	0.0001
Simulation time (d)	0.5
Pe	1
Cr	1×10^4

Table 4.2. Simulation Parameters for the Comparison of the UTCHEM Model to the Model of Molz *et al.* [1986]

Parameter	**Value**
Flow and porous medium parameters	
Column length, L (m)	1.0
Average velocity, v (m/d)	0.5
Porosity, ϕ	0.30
Bulk soil density, ρ_b (g/cm^3)	1.67
Longitudinal dispersivity, α_L (m)	0.0056
Numerical simulation parameters:	
Number of grid blocks	100
Numerical time step (d)	0.001
Simulation time (d)	4
Pe	1.79
Cr	2.2×10^{-2}
Biodegradation kinetic parameters	
Initial concentration of all chemical species (mg/L)	5.0
Substrate injection concentration, S_0 (mg/L)	15.0
Electron acceptor injection concentration, A_0 (mg/L)	5.0
Initial attached biomass population, C_b (cells/g-solid)	6.0×10^{-6}
Biomass density, ρ_X (g/cm^3)	0.09
Colony radius , r_c (cm)	5.0×10^{-4}
Colony thickness , τ_c(cm)	5.0×10^{-4}
Cells/colony, n	100
Substrate retardation coefficient, R_f	1.12
Biomass maximum specific growth rate, μ_{max} (d^{-1})	4.34
Biomass endogenous decay coefficient, b (d^{-1})	0.02
Biomass yield coefficient , Y (mass X/mass S)	0.278
Substrate half-saturation coefficient, K_S (mg/L)	120
Electron acceptor half-saturation coefficient, K_S (mg/L)	0.77
Electron acceptor utilization coefficient, E (mass A/mass S)	0.3892
Substrate mass transfer coefficient, κ_S (cm/d)	1.2
Electron acceptor mass transfer coefficient, κ_A (cm/d)	14.2

Table 4.3. Parameters for Coreflood of Silfanus (1990)

Parameter	Value
Core diameter	2 in
Core length	5.98 in
Vertz brine permeability	526 md
Porosity	0.22
Brine permeability at S_{or}	55 md
Brine density	1.1 g/cc
Oil density	0.89 g/cc
Brine viscosity	1.4 cp
Oil viscosity	8 cp
Residual water saturation	0.274
Residual oil saturation	0.296
Injection rate	46.8 cc/hr
Injected bacteria conc.	9×10^8 cells/cc
Injected ammonium conc.	47.5 mM
Injected glucose conc.	59 mM
Injected nitrate conc.	37.5 mM
Bacteria density	0.7917 g/cc

Table 4.4. Input parameters used in UTCHEM simulation of MEOR coreflood

Parameter	Value	
First order abiotic reaction rate constant (RABIO)	0.00432 (d^{-1})	
Biomass Partitioning coeff. (ADSBIO)	50	
Max. specific growth rate of unattached microorganisms (BRMAX)	0.0288 (d^{-1}) 14.4 (d^{-1})	(treatments 1-4) (treatments 5-14)
Max. specific growth rate of attached microorganisms (BRMAXB)	0.0288 (d^{-1}) 14.4 (d^{-1})	(treatments 1-4) (treatments 5-14)
Yield coefficient : biomass produced per mass of substrate biodegraded (YXS)	0.8202	
Substrate half-saturation coeff.(AKS)	45 mg/l	
Electron acceptor half-saturation coeff. (AKA)	45 mg/l	
Electron acceptor utilization coeff.(FEA)	0.1202	
Product generation coeff. (FPR)	0.3 0.4	(treatments 1-6) (treatments 7-14)

FIGURES

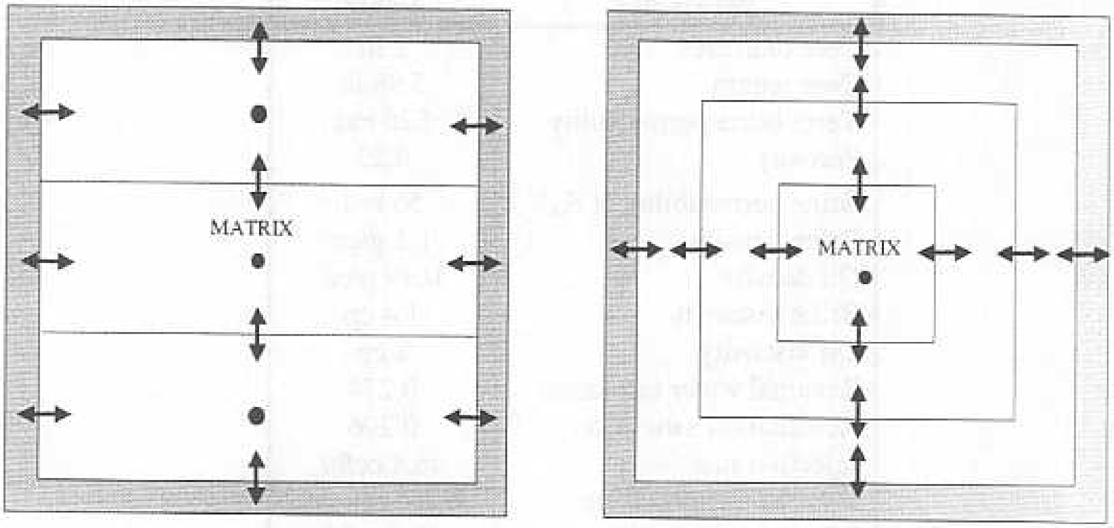

Stacked grids

Nested grids

Fig. 1.1: Subgrids of a single matrix block.

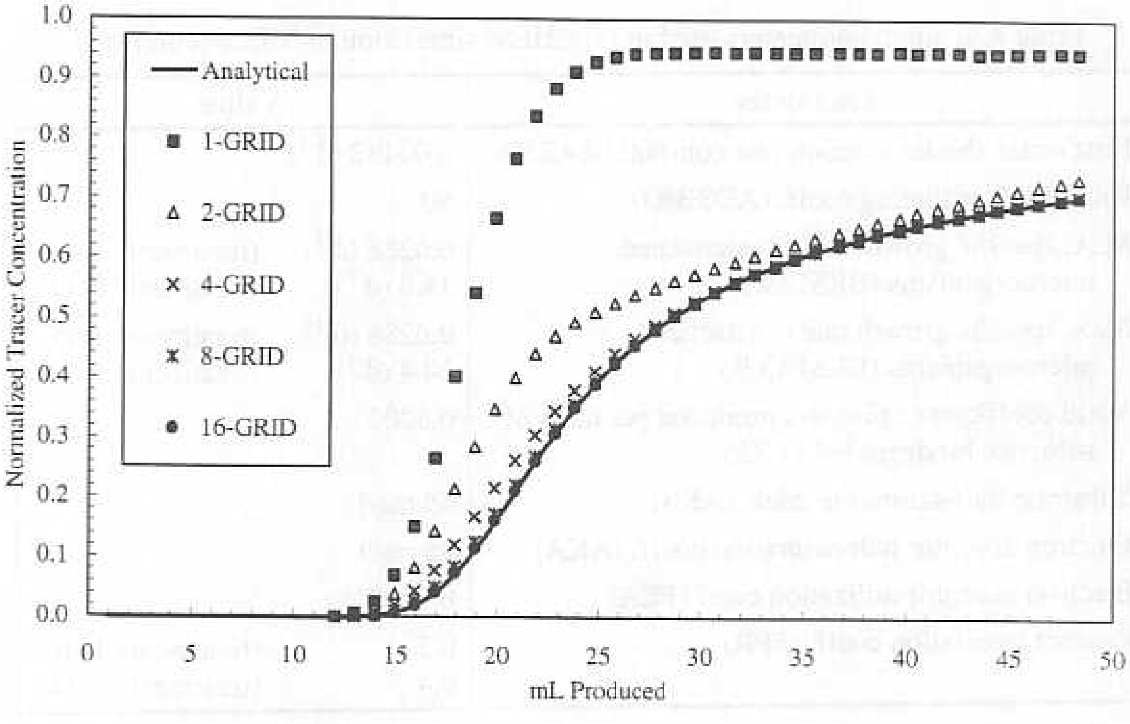

Fig. 1.2. Comparison of UTCHEM results with analytical solution.

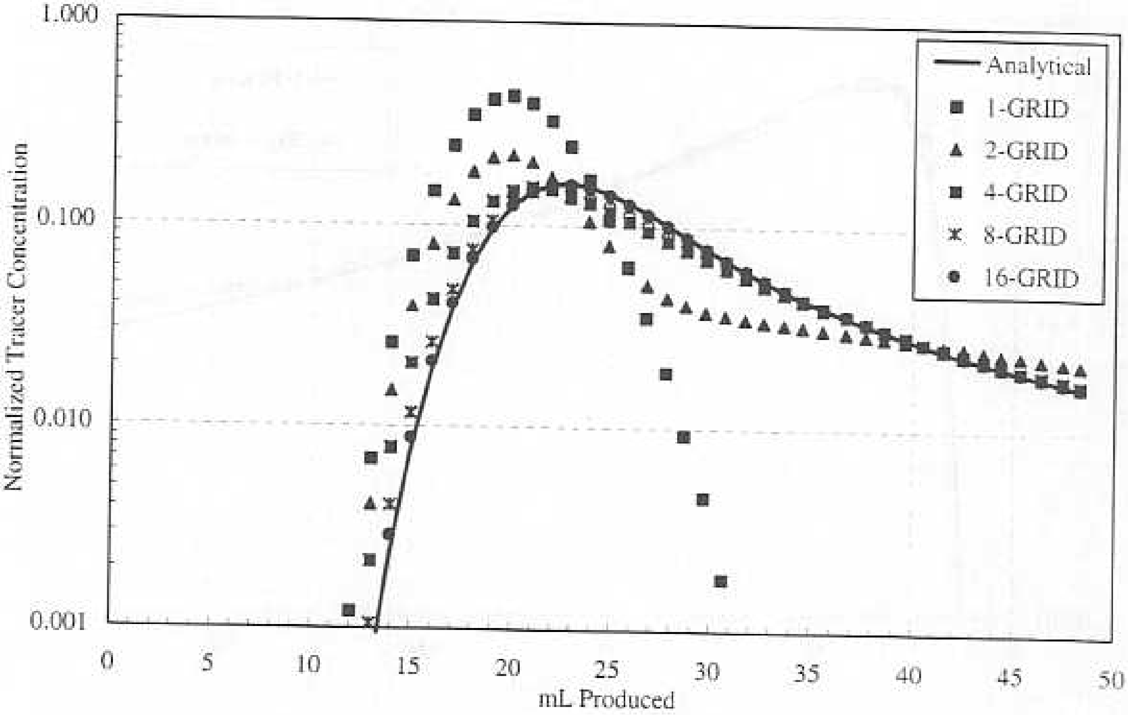

Fig. 1.3. Comparison of UTCHEM results with analytical solution.

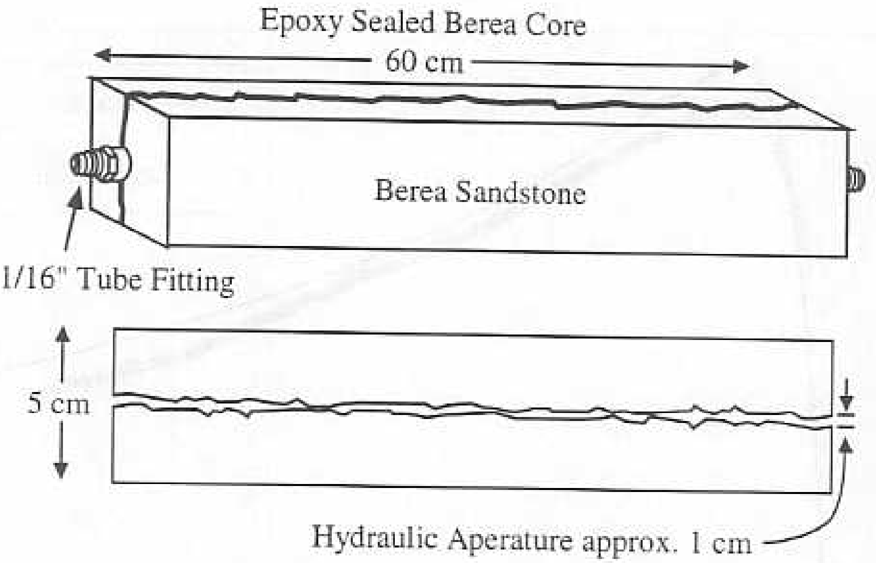

Fig. 1.4. Schematic of the core used for single-fracture experiments.

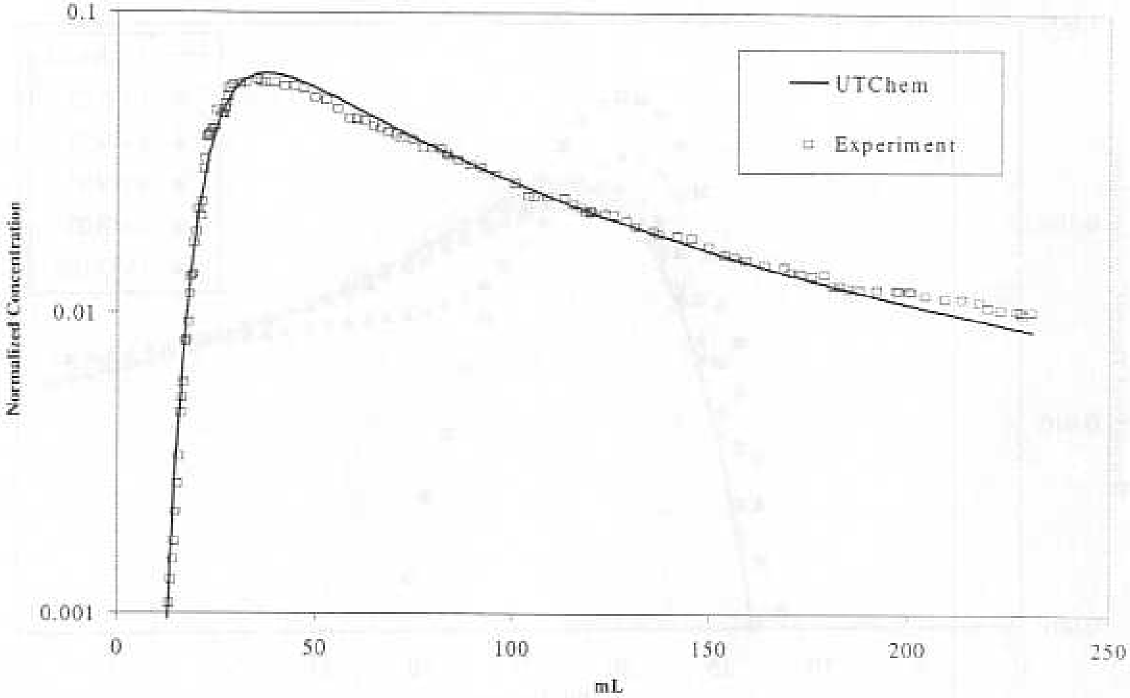

Fig. 1.5. Comparison of IPA response data and UTCHEM model in a fractured Berea core.

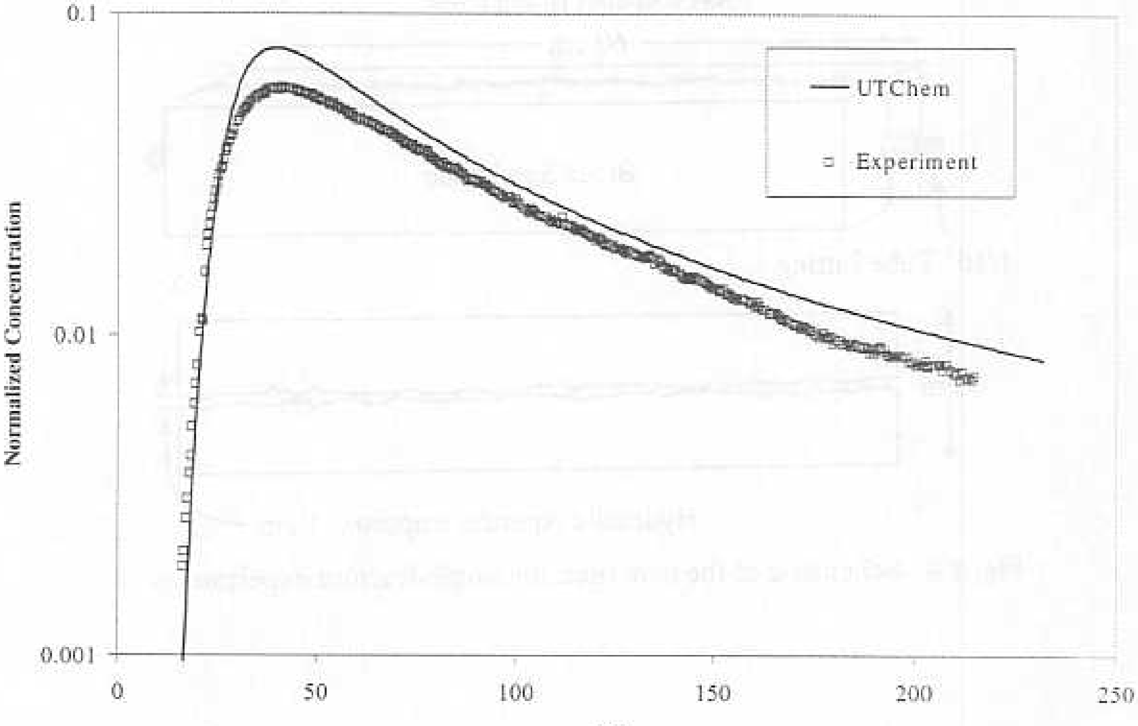

Fig. 1.6. Comparison of hexanol response data and UTCHEM model in a fractured Berea core.

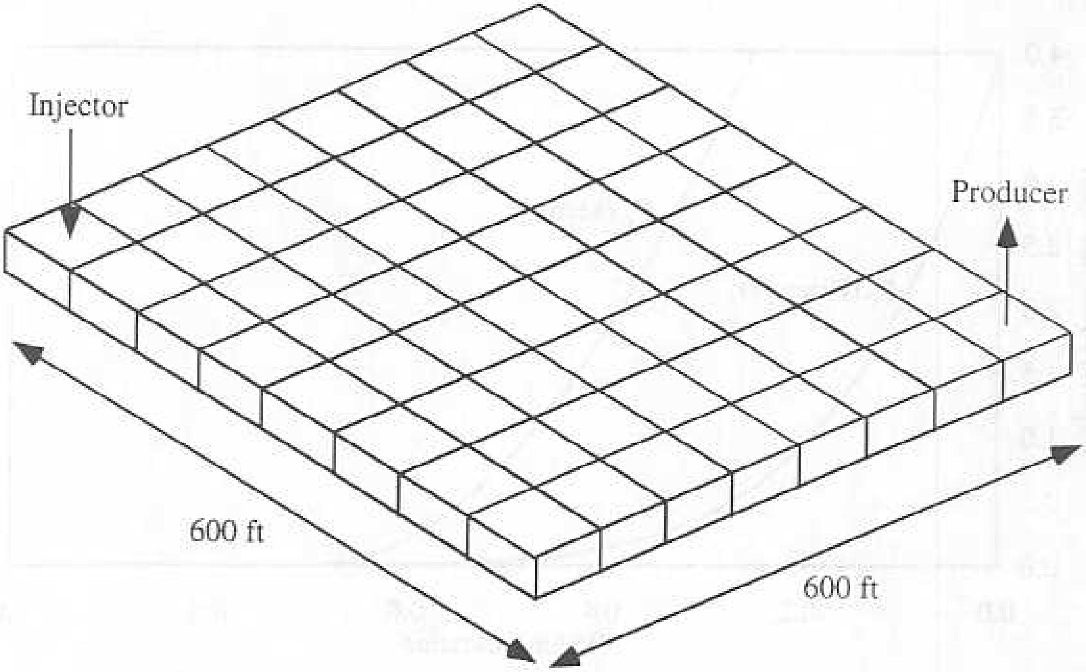

Fig. 1.7. Schematic of grid used in ECLIPSE and UTCHEM.

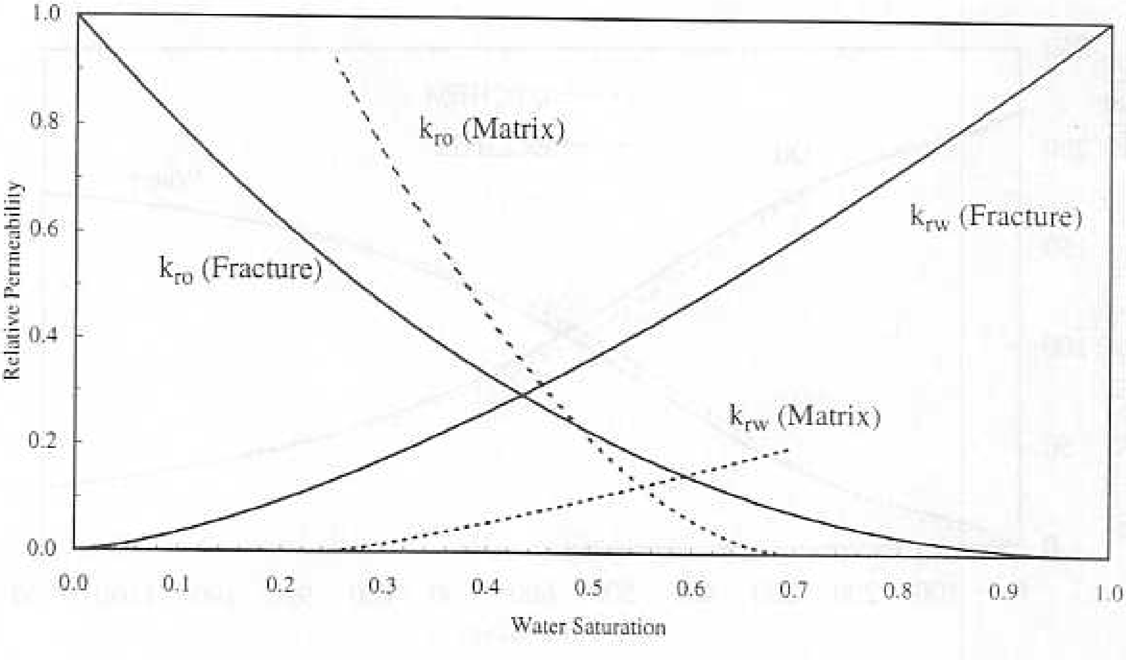

Fig. 1.8. Water and oil relative permeability curves for both fracture and matrix rocks used in the simulations.

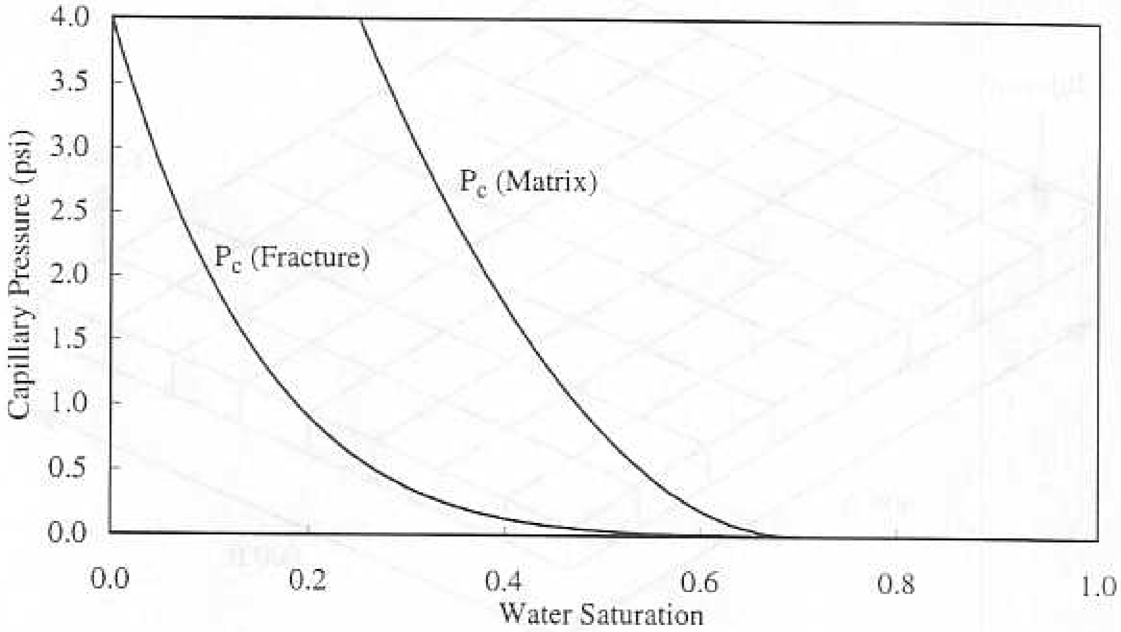

Fig. 1.9. Capillary pressure curves for fracture and matrix rocks used in the simulations.

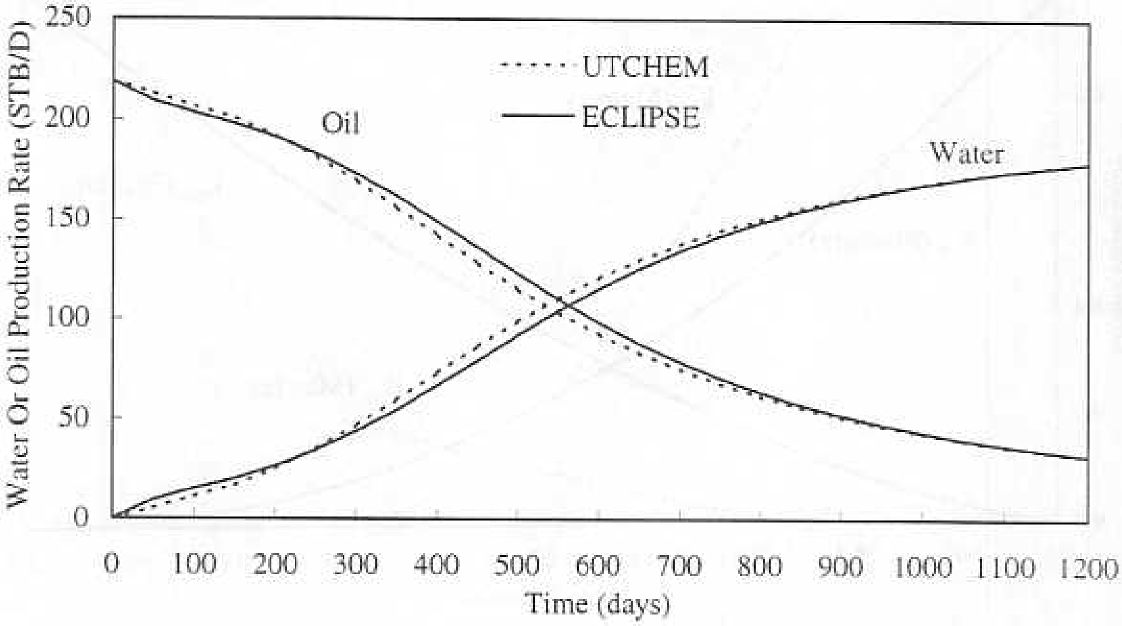

Fig. 1.10. Comparison of production rates.

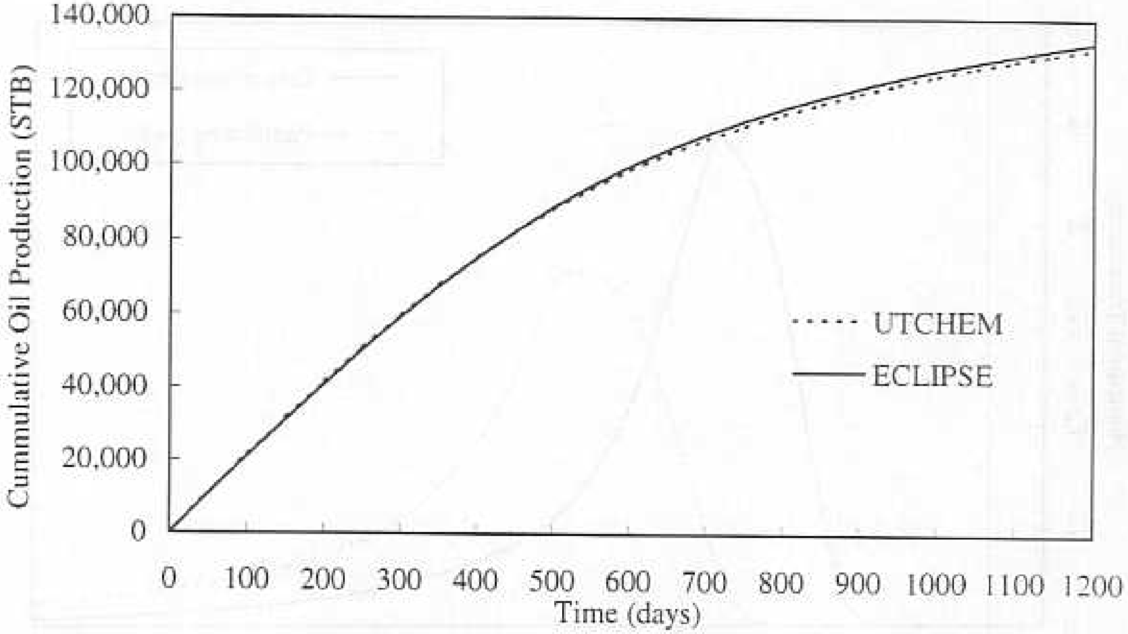

Fig. 1.11. Comparison of cumulative oil recovery.

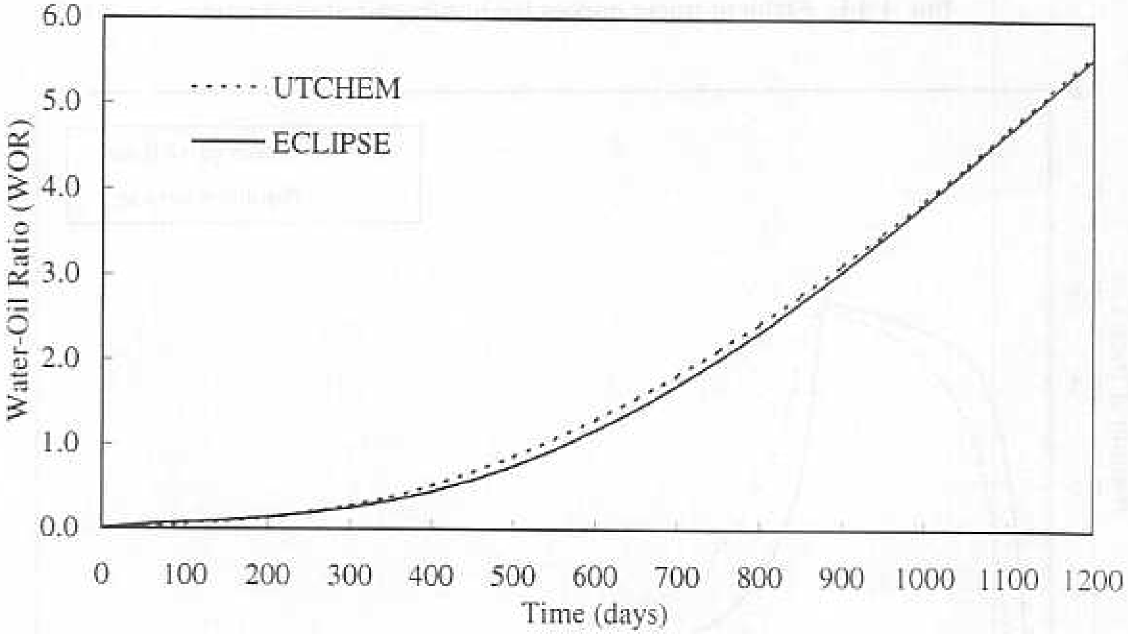

Fig. 1.12. Comparison of water-oil ratio.

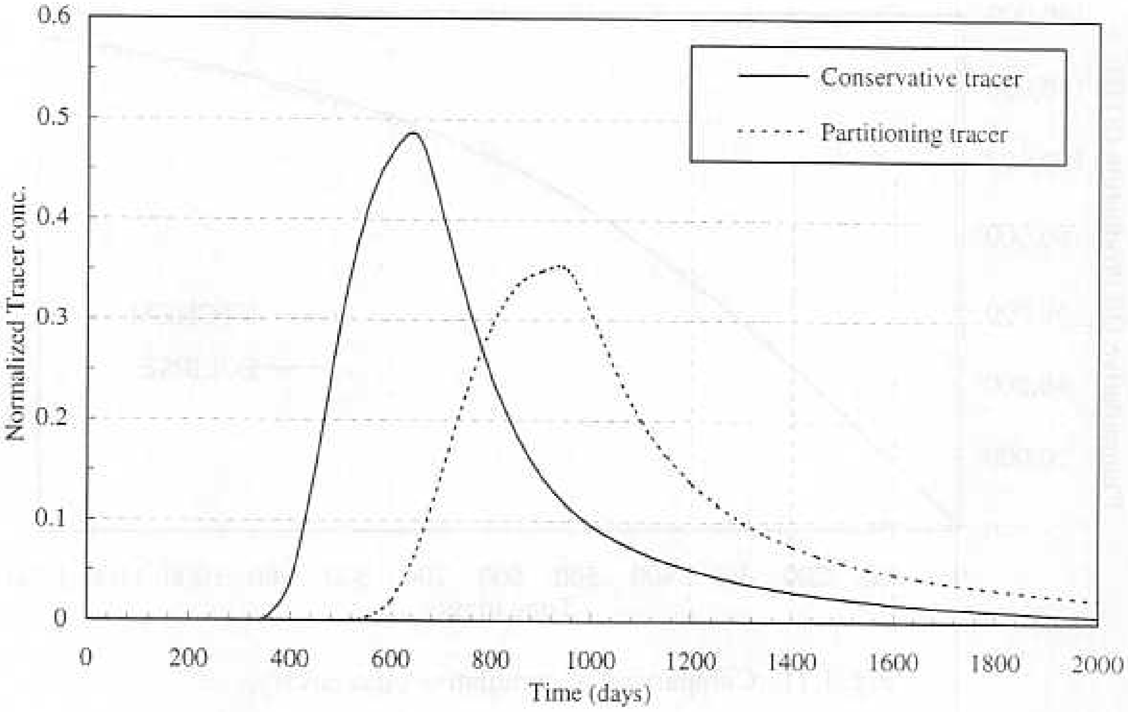

Fig. 1.13. Effluent tracer curves for nonfractured reservoir.

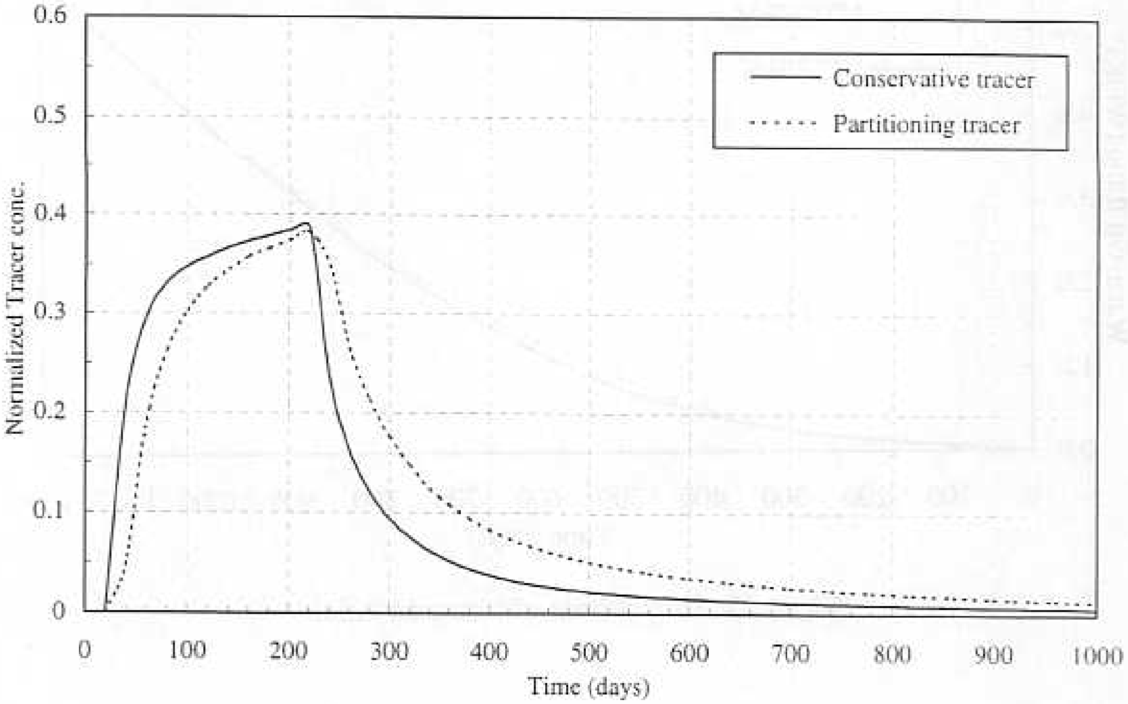

Fig. 1.14. Effluent tracer curves for fractured reservoir.

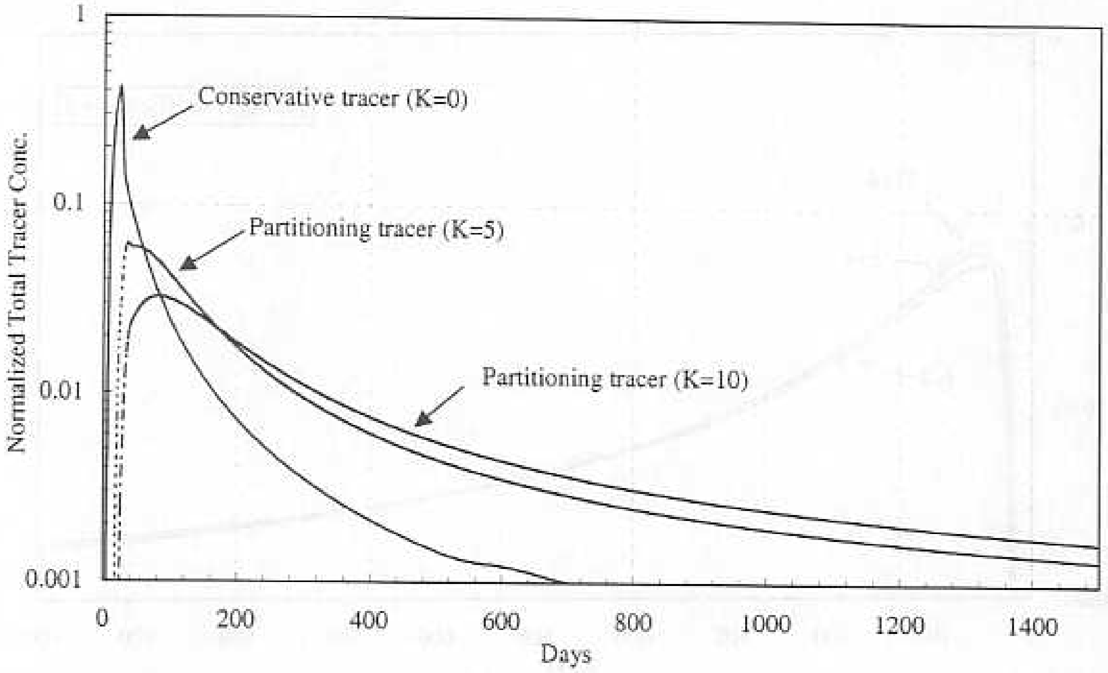

Fig. 1.15. Tracer response curves in a naturally fractured reservoir with mobile oil saturation present in the matrix only.

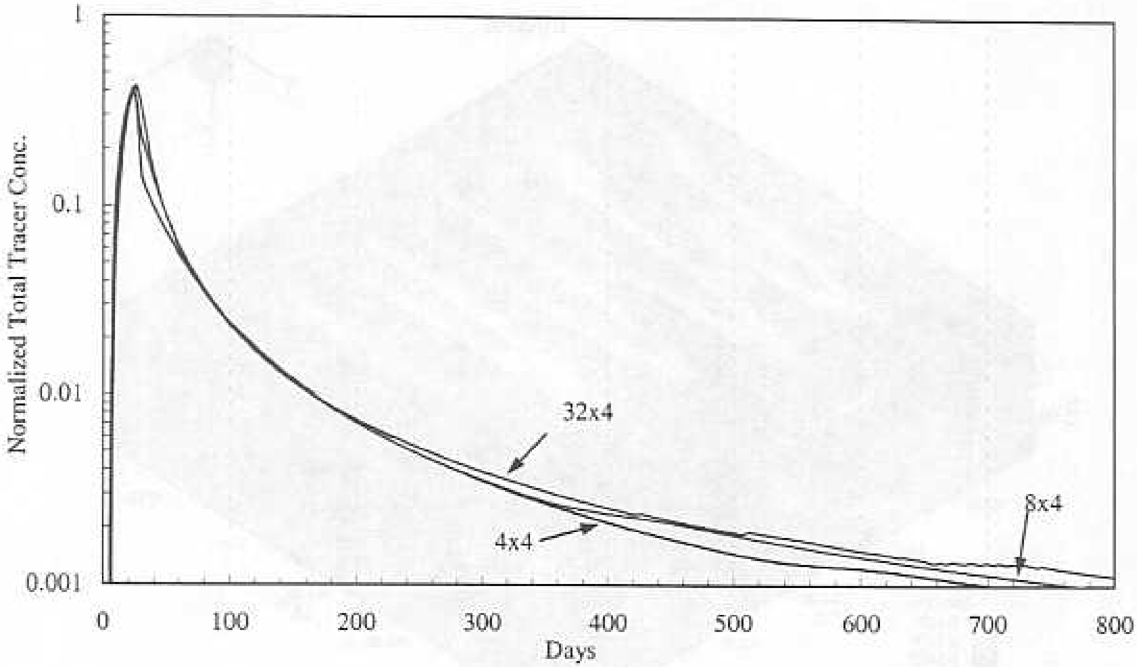

Fig. 1.16. Effect of horizontal matrix subgridding on effluent conservative tracer concentration.

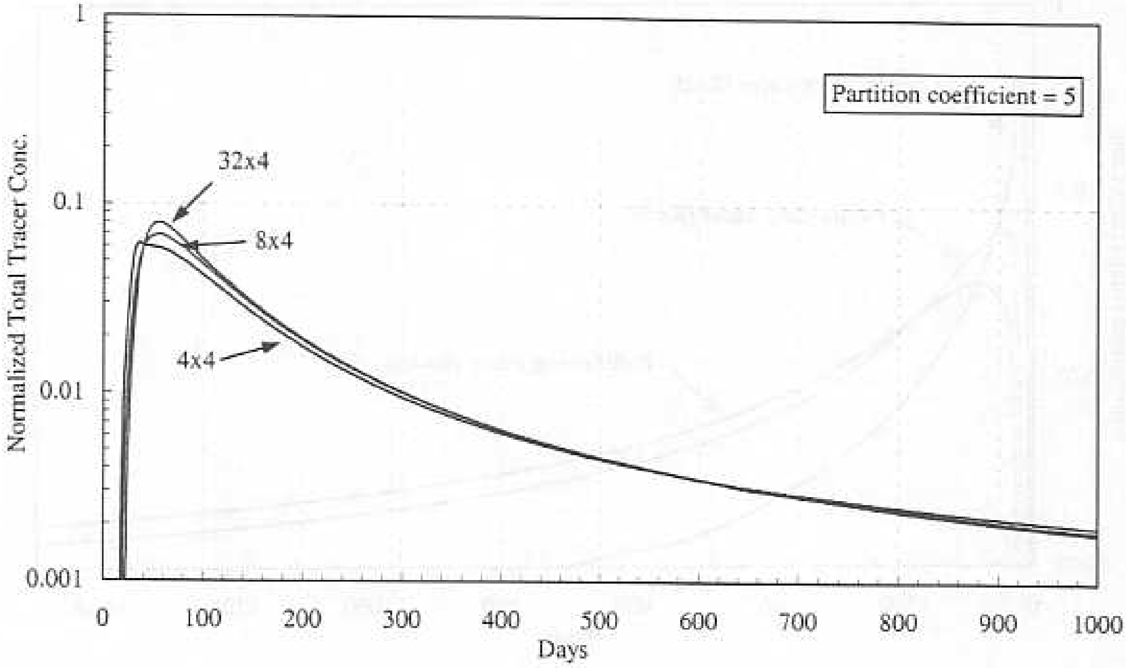

Fig. 1.17. Effect of horizontal matrix subgridding on effluent partitioning tracer concentration

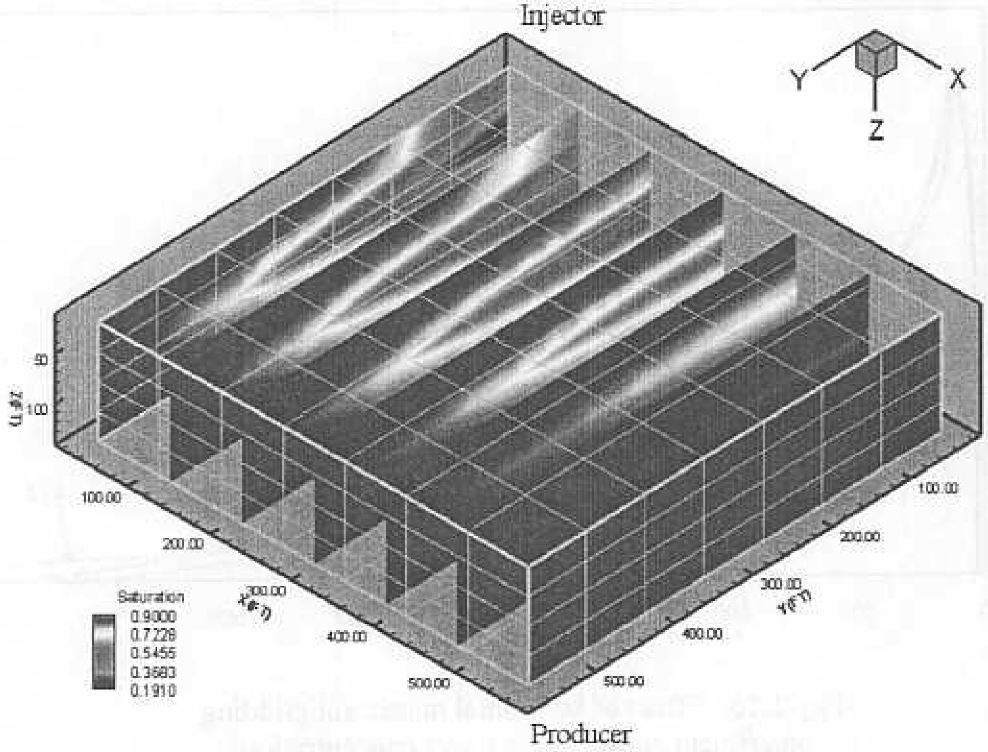

Fig. 1.18. Oil saturation profile in the fracture at the end of 50 days.

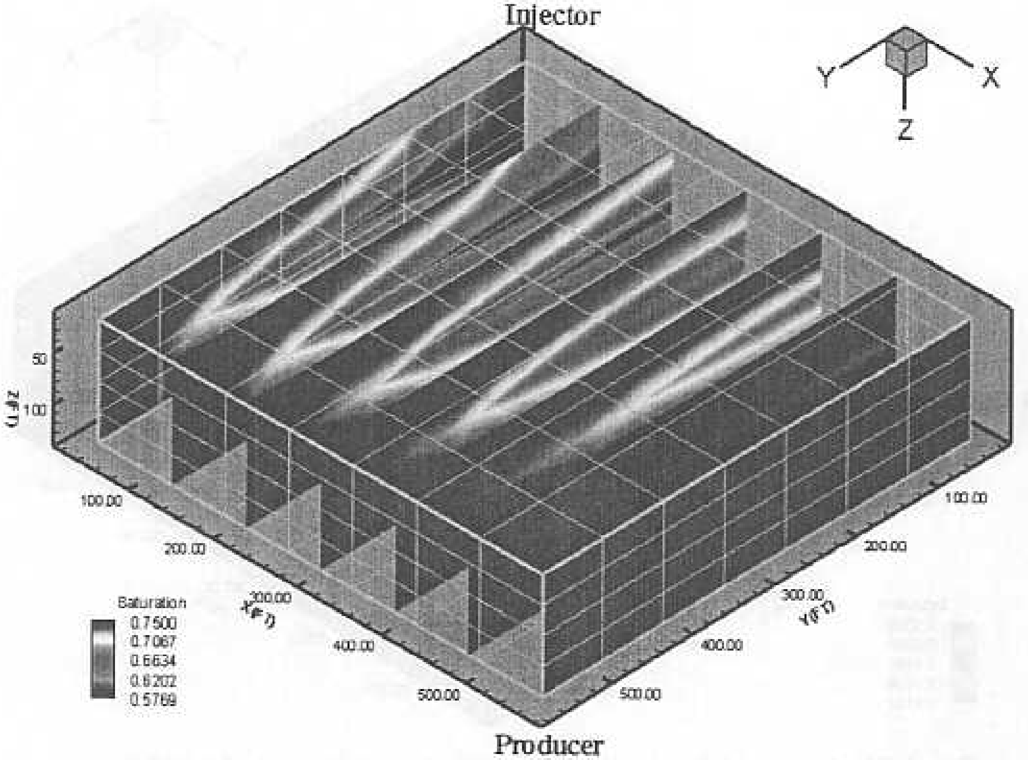

Fig. 1.19. Average oil saturation in the matrix at 50 days.

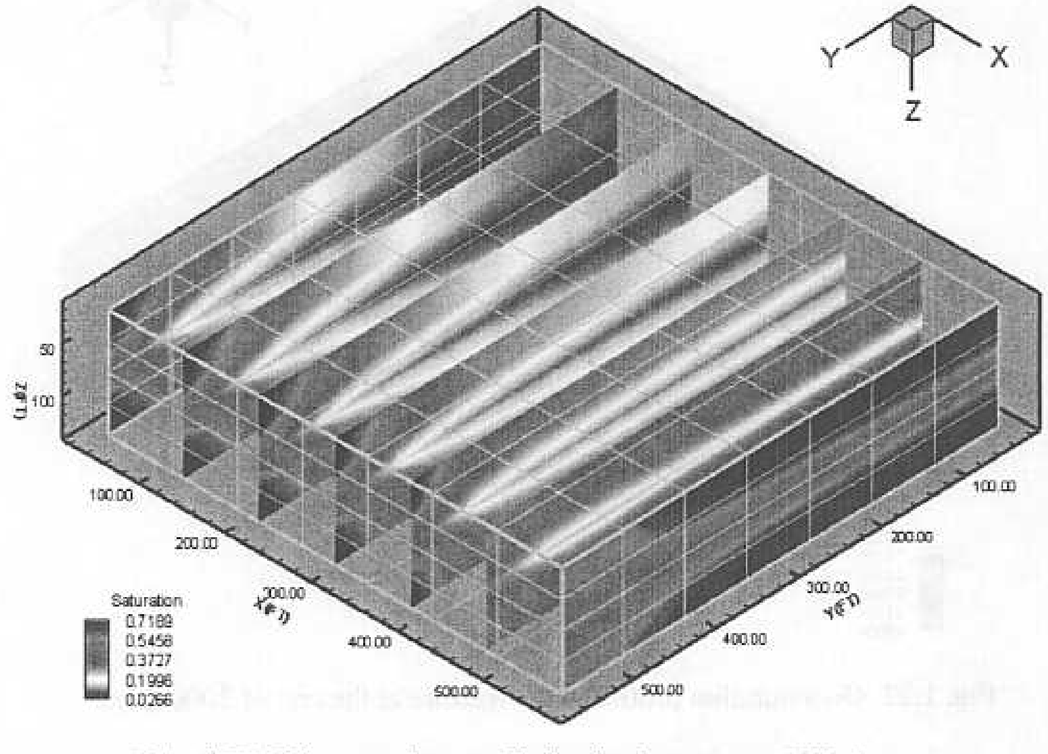

Fig. 1.20. Oil saturation profile in the fracture at 1500 days.

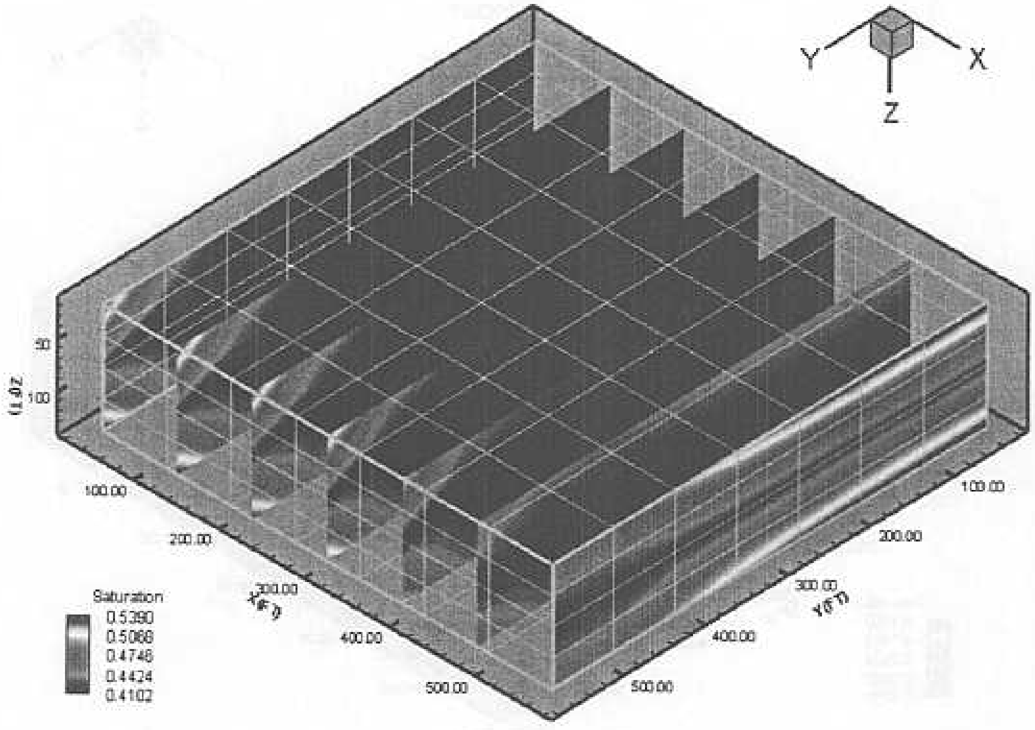

Fig. 1.21. Average oil saturation in the matrix at the end of 1500 days.

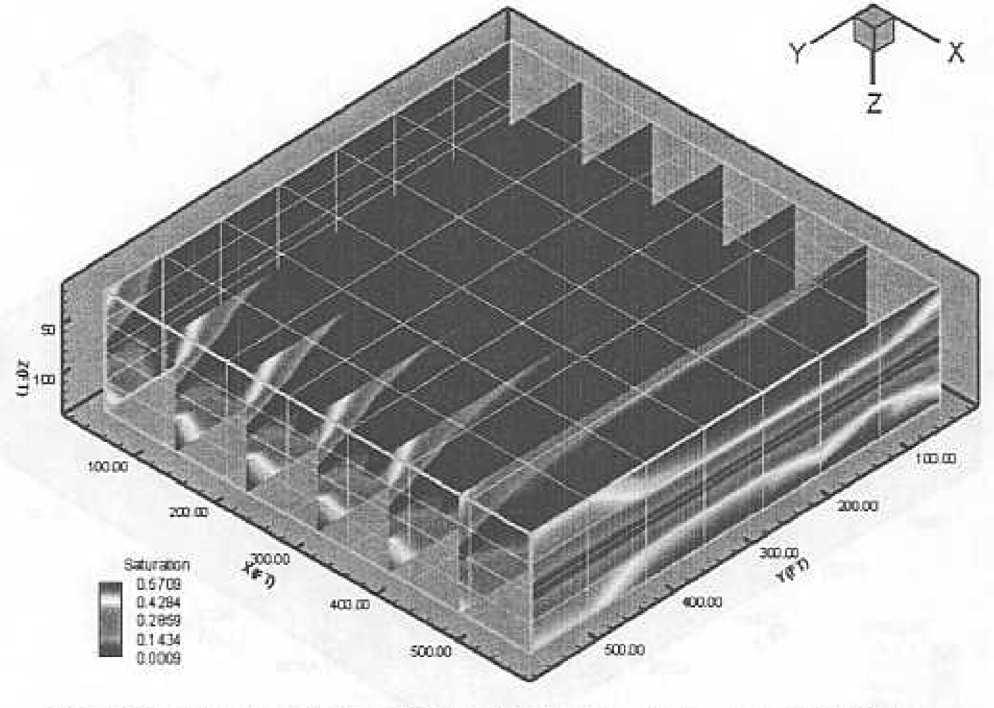

Fig. 1.22. Oil saturation profile in the fracture at the end of 2000 days.

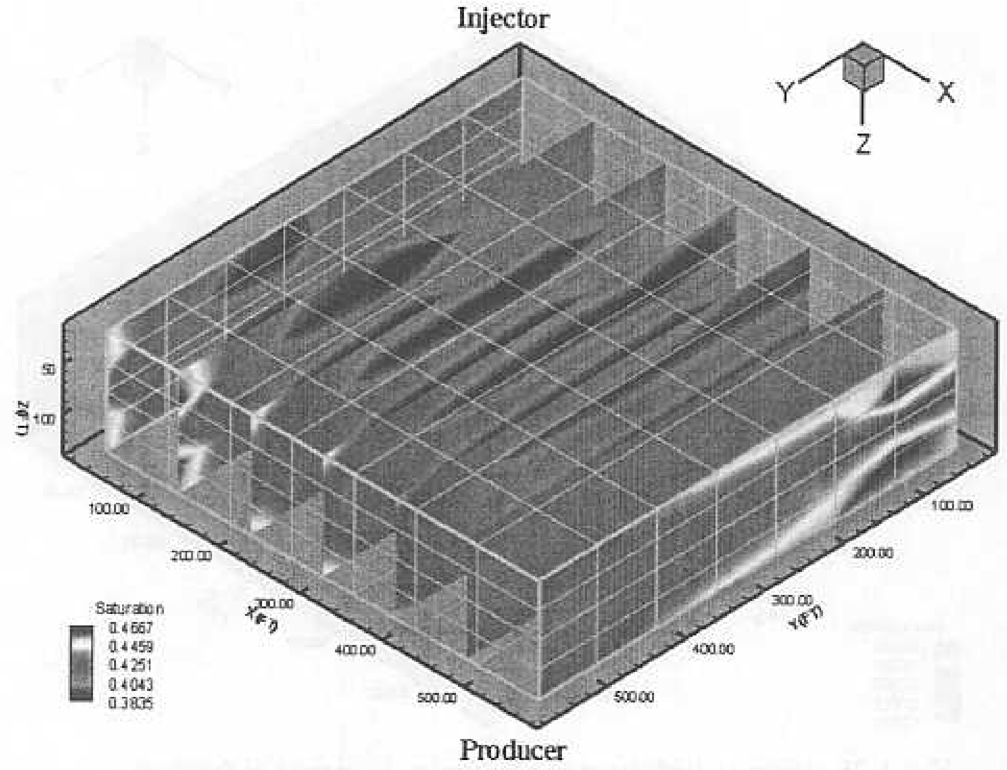

Fig. 1.23. Average oil saturation in the matrix at the end of 2000 days.

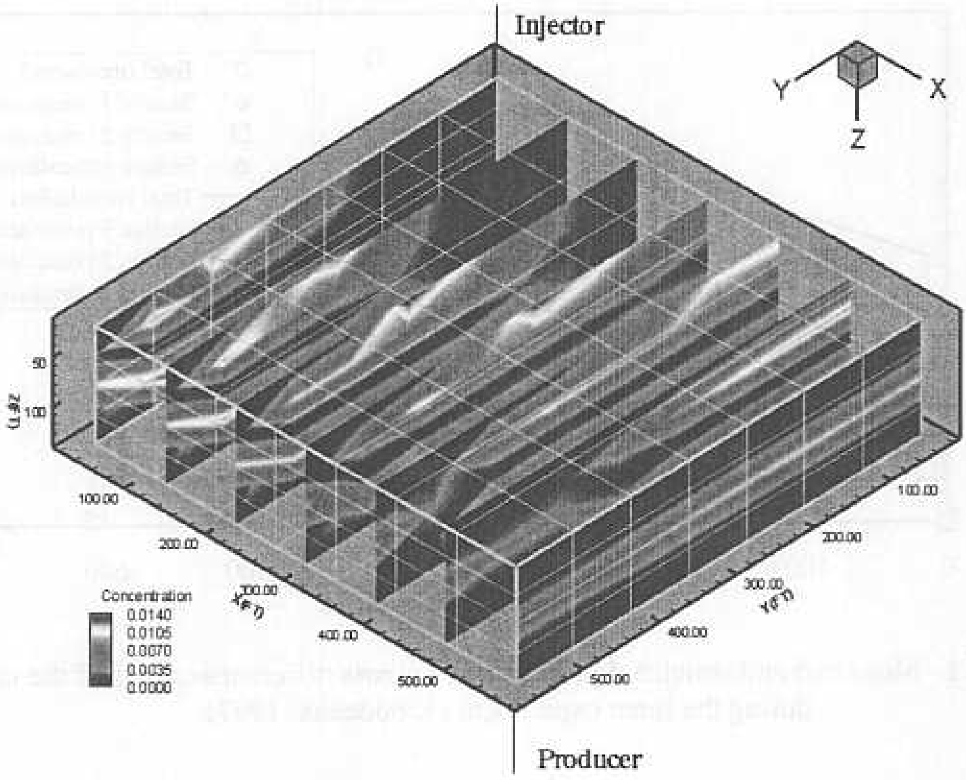

Fig. 1.24. Surfactant concentration profile in the fracture at 2000 days.

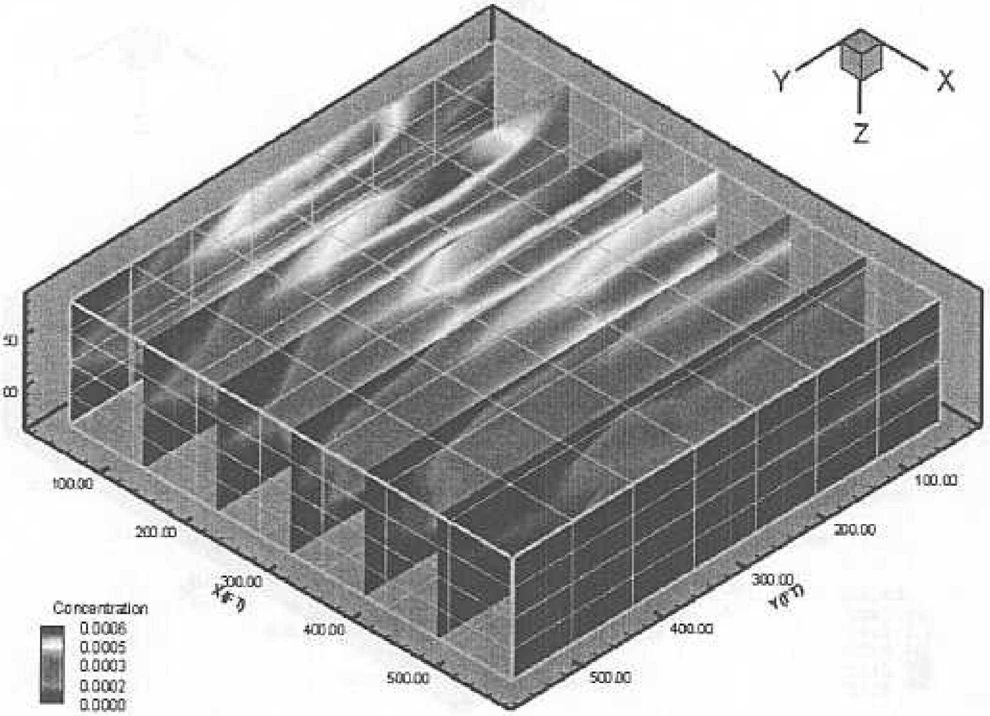

Fig. 1.25. Average surfactant concentration in matrix at 2000 days.

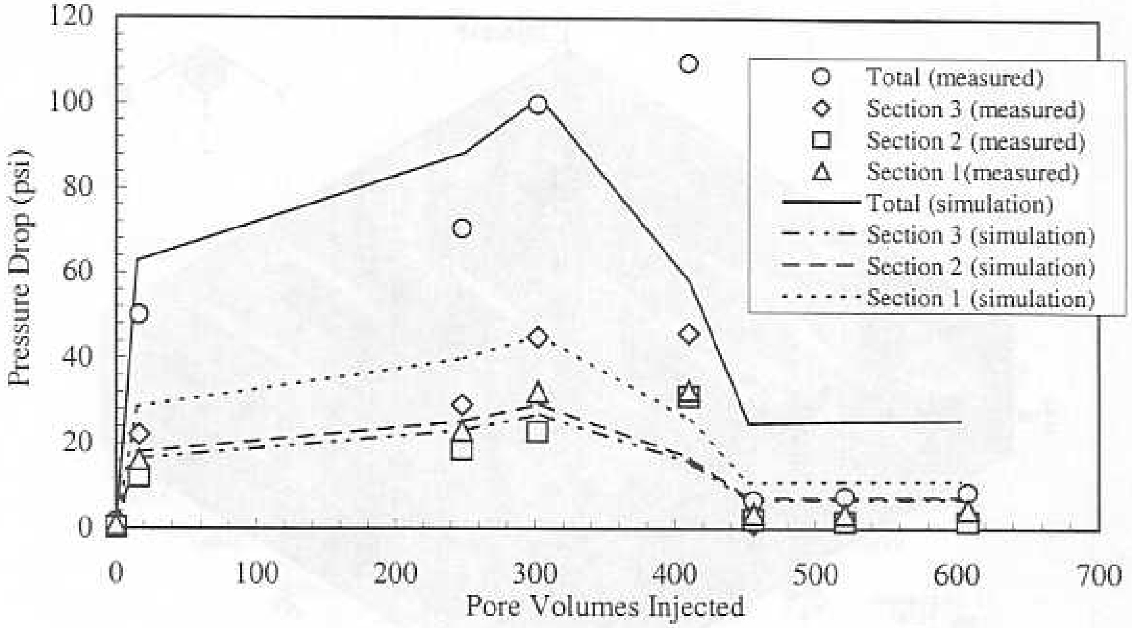

Fig. 2.1: Measured and simulated pressure drop across different sections of the core during the foam experiment (Kibodeaux, 1997).

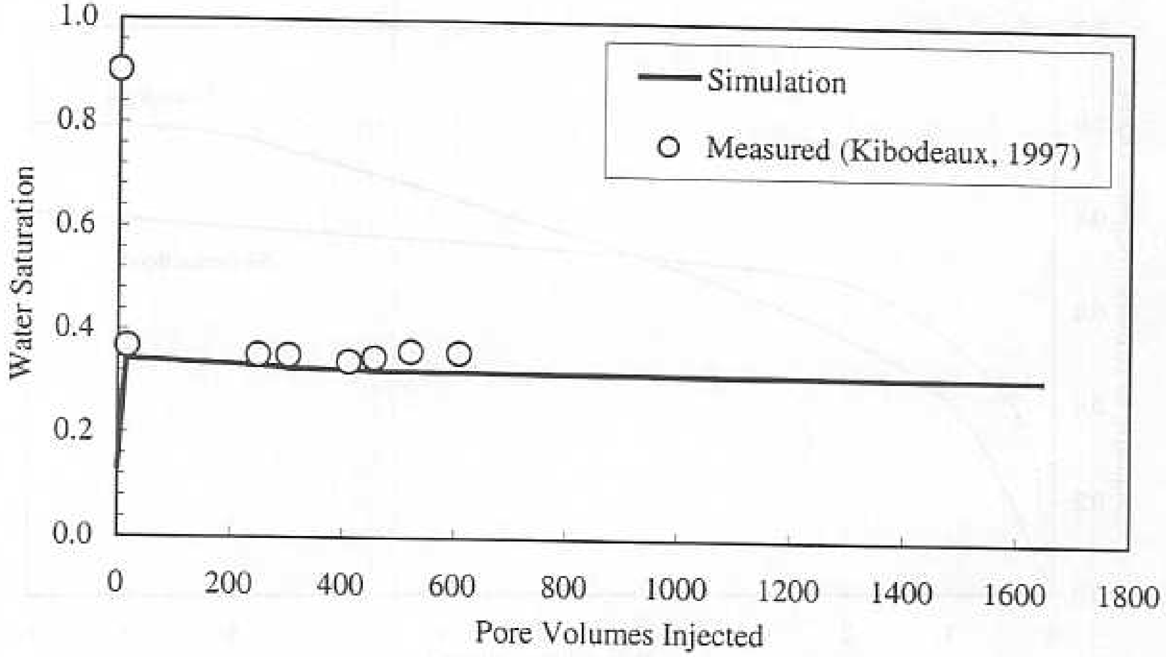

Fig. 2.2: Measured and simulated average water saturation during the foam experiment.

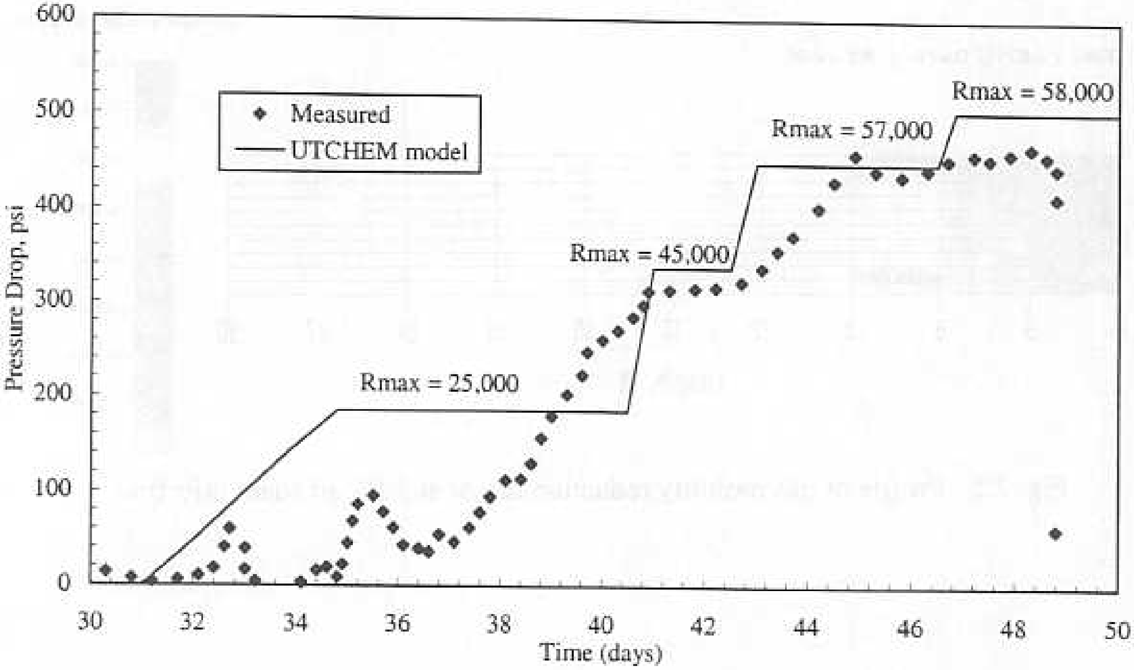

Fig. 2.3. Comparison of measured pressure drop of Vassenden *et al.* (1999) and UTCHEM simulation results.

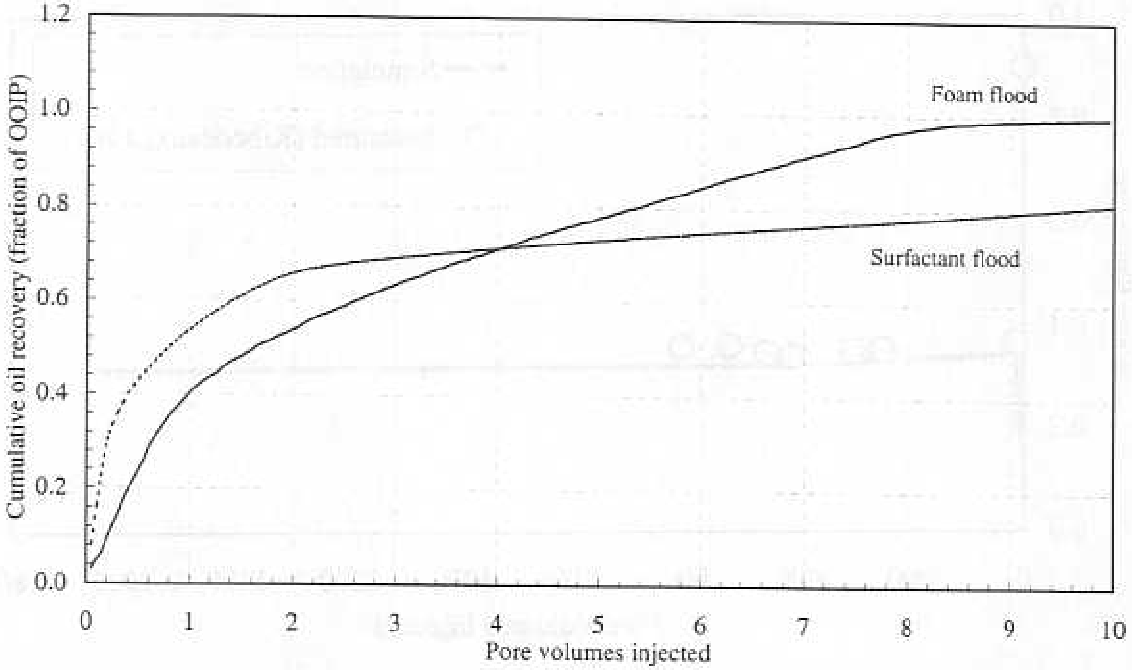

Fig. 2.4. Comparison of oil recovery for foam and surfactant floods.

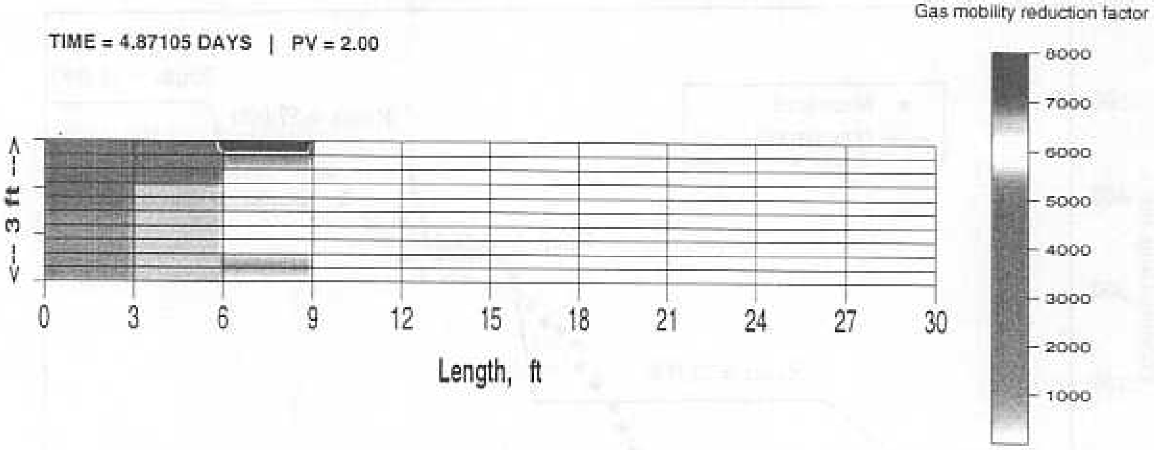

Fig. 2.5. Profile of gas mobility reduction factor at 2 PV of foam injection.

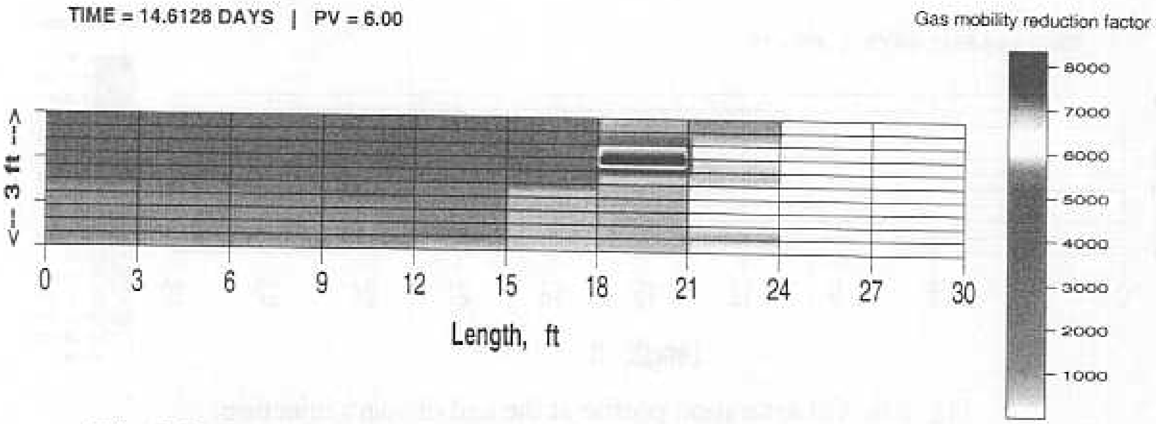

Fig. 2.6. Profile of gas mobility reduction factor at 6 PV of foam injection.

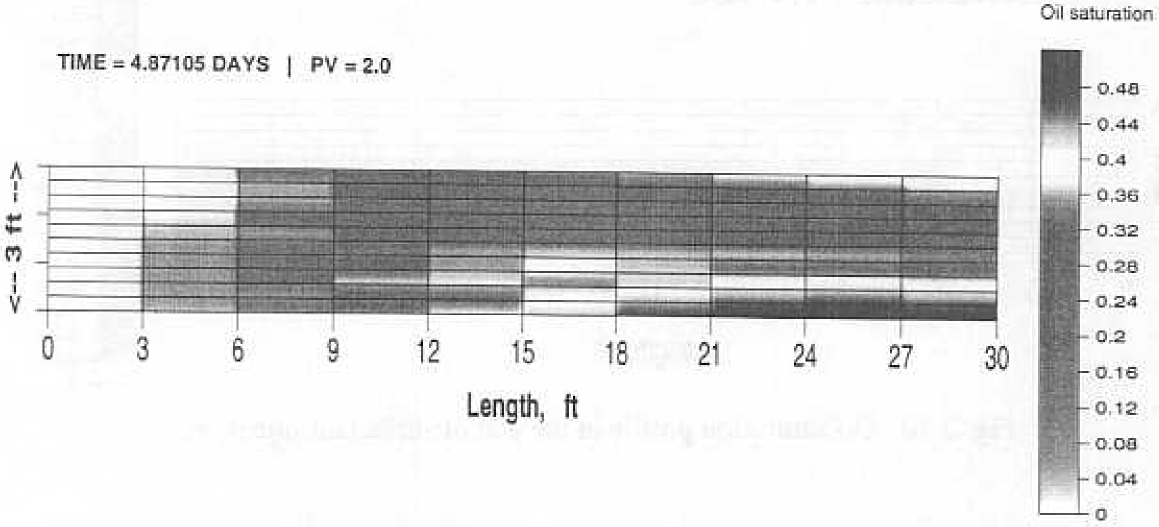

Fig. 2.7. Oil saturation profile at 2 PV of foam injection.

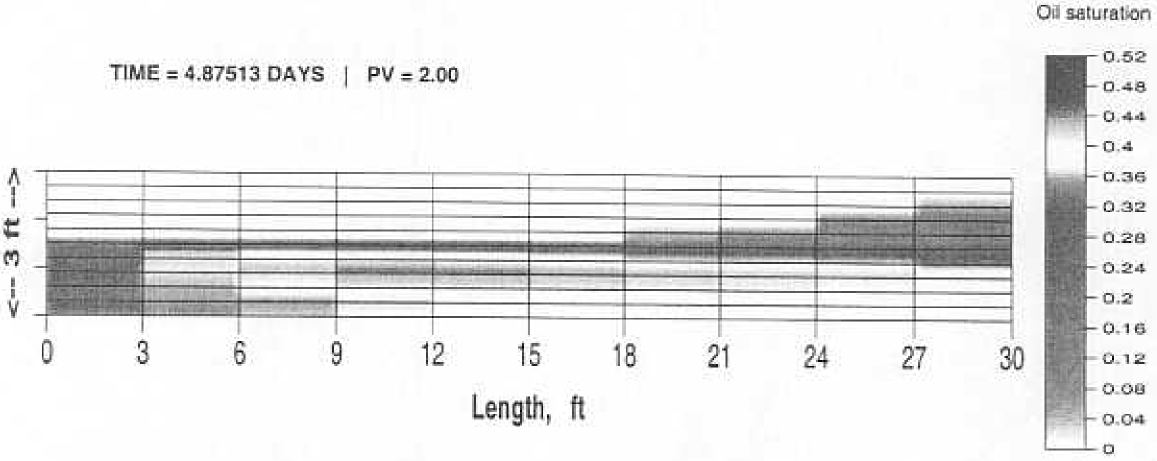

Fig. 2.8. Oil saturation profile at 2 PV of surfactant injection.

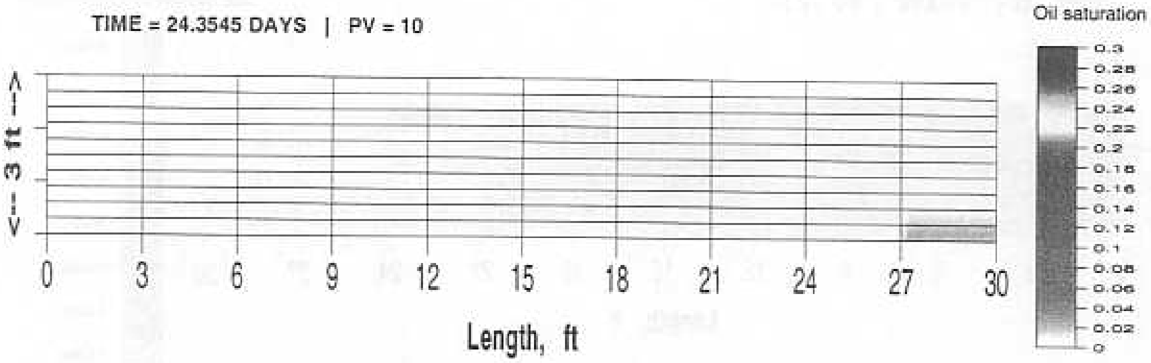

Fig. 2.9. Oil saturation profile at the end of foam injection.

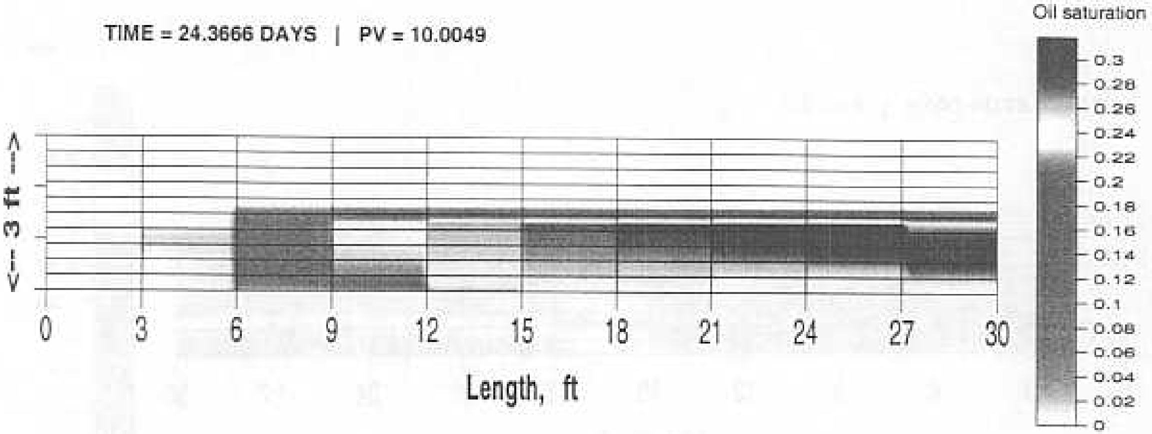

Fig. 2.10. Oil saturation profile at the end of surfactant injection.

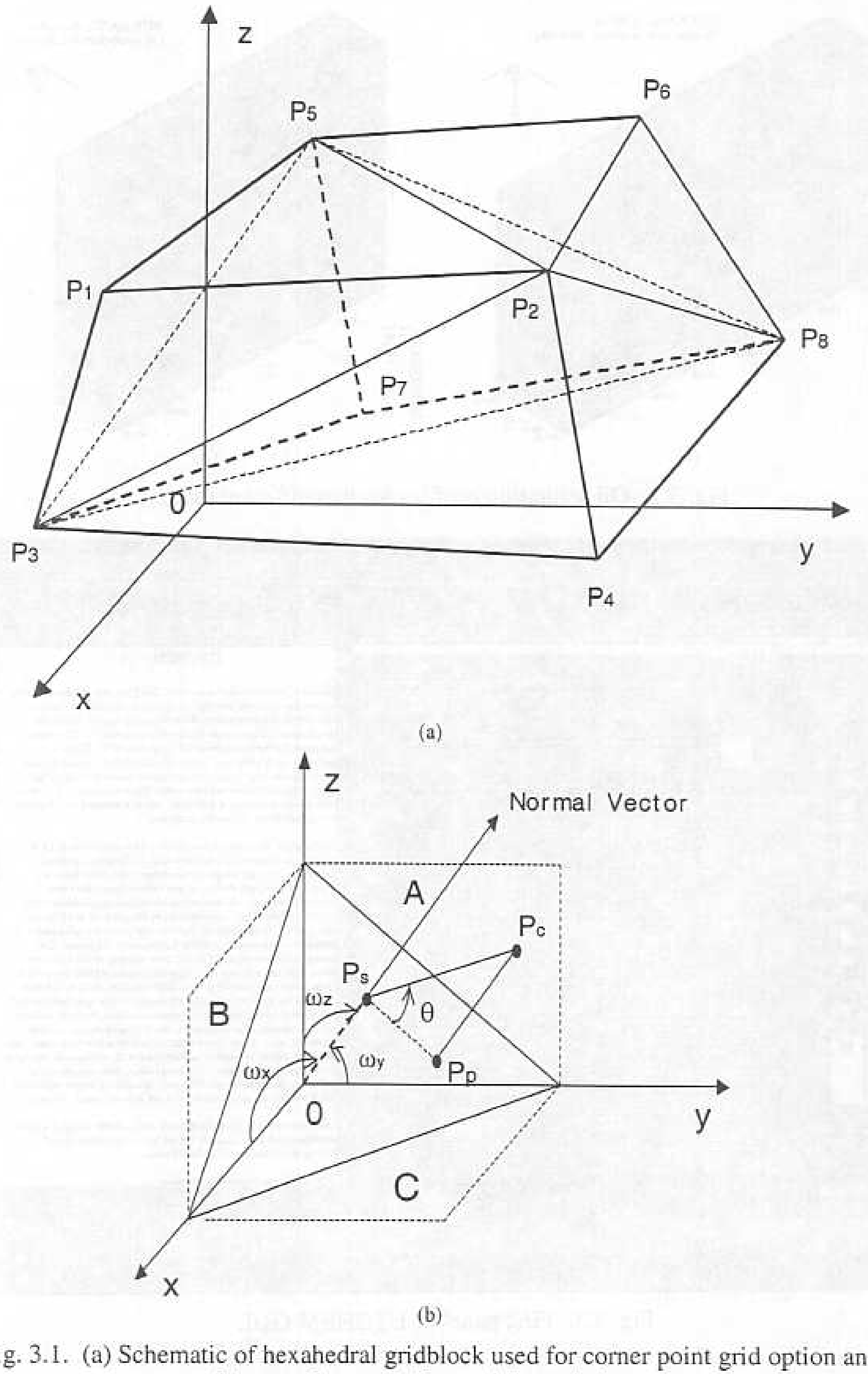

Fig. 3.1. (a) Schematic of hexahedral gridblock used for corner point grid option and (b) normal vector of a quadrilateral plane.

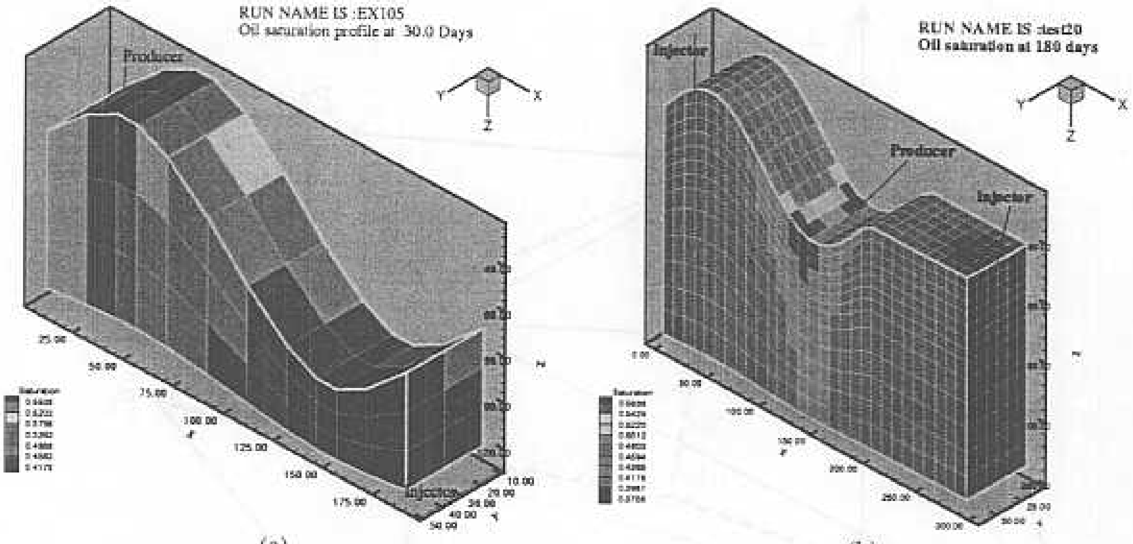

(a) (b)

Fig. 3.2. Oil saturation profiles for two different runs.

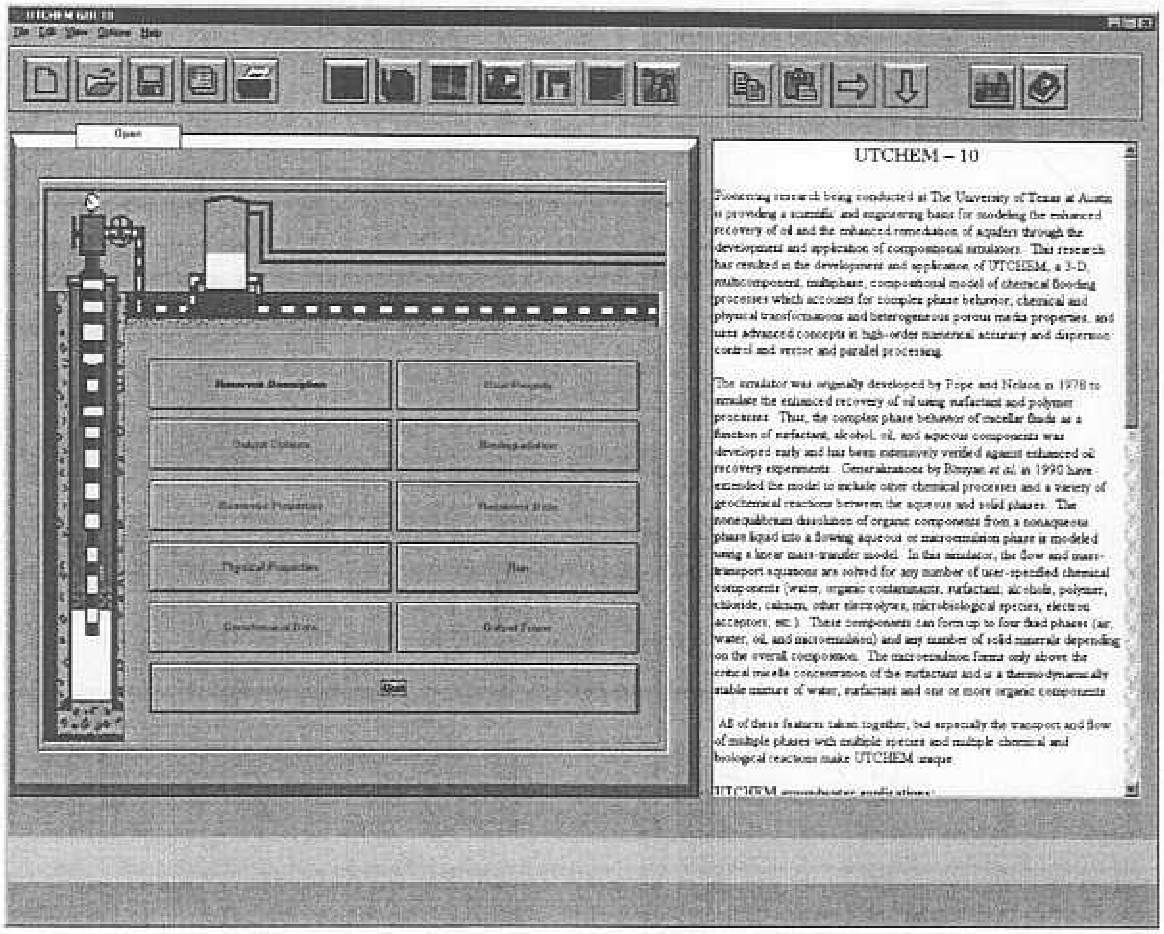

UTCHEM – 10

Pioneering research being conducted at The University of Texas at Austin is providing a scientific and engineering basis for modeling the enhanced recovery of oil and the enhanced remediation of aquifers through the development and application of compositional simulators. This research has resulted in the development and application of UTCHEM, a 3-D, multicomponent, multiphase, compositional model of chemical flooding processes which accounts for complex phase behavior, chemical and physical transformations and heterogeneous porous media properties, and uses advanced concepts in high-order numerical accuracy and dispersion control and vector and parallel processing.

The simulator was originally developed by Pope and Nelson in 1978 to simulate the enhanced recovery of oil using surfactant and polymer processes. Thus, the complex phase behavior of micellar fluids as a function of surfactant, alcohol, oil, and aqueous components was developed early and has been extensively verified against enhanced oil recovery experiments. Generalizations by Bhuyan *et al.* in 1990 have extended the model to include other chemical processes and a variety of geochemical reactions between the aqueous and solid phases. The nonequilibrium dissolution of organic components from a nonaqueous phase liquid into a flowing aqueous or microemulsion phase is modeled using a linear mass-transfer model. In this simulator, the flow and mass-transport equations are solved for any number of user-specified chemical components (water, organic contaminants, surfactant, alcohols, polymer, chloride, calcium, other electrolytes, microbiological species, electron acceptors, etc.). These components can form up to four fluid phases (air, water, oil, and microemulsion) and any number of solid minerals depending on the overall composition. The microemulsion forms only above the critical micelle concentration of the surfactant and is a thermodynamically stable mixture of water, surfactant and one or more organic components.

All of these features taken together, but especially the transport and flow of multiple phases with multiple species and multiple chemical and biological reactions make UTCHEM unique.

UTCHEM groundwater applications:

Fig. 3.3. First panel of UTCHEM GUI.

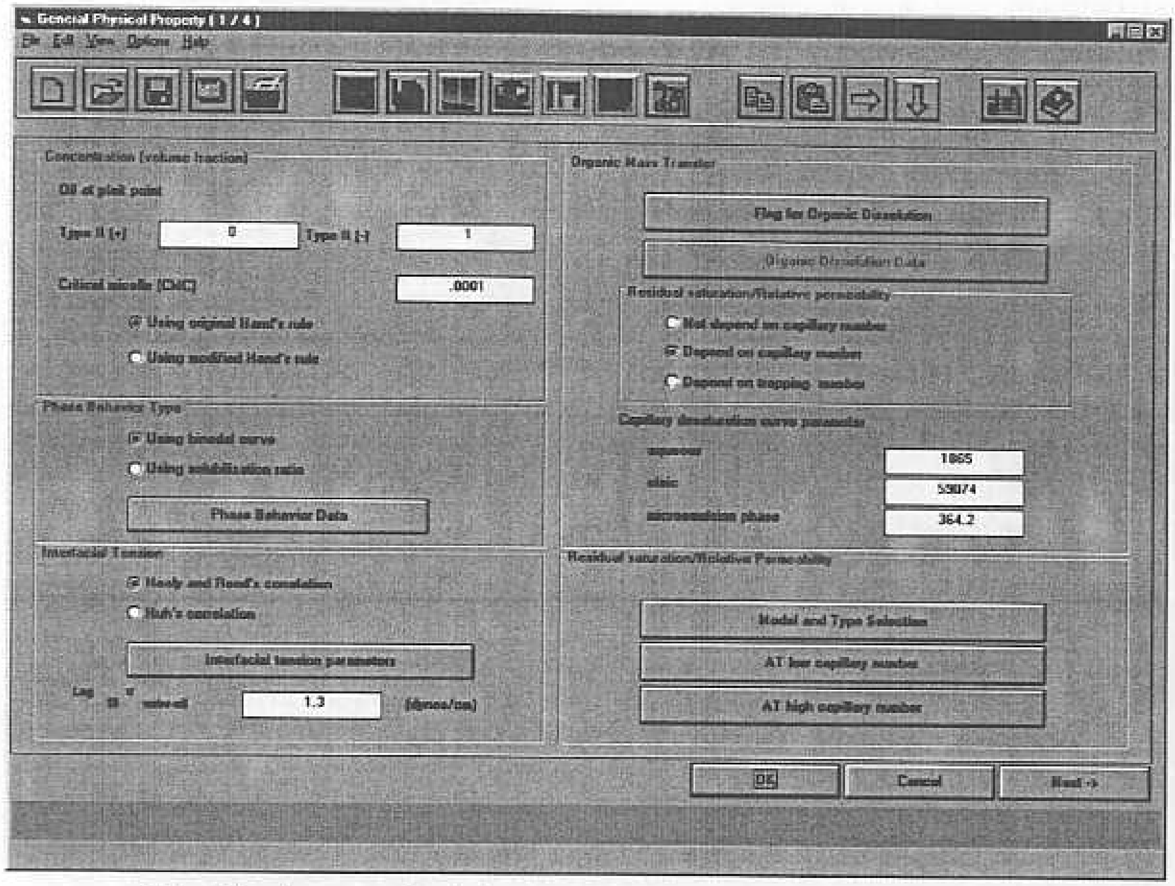

Concentration (volume fraction)

Oil at plait point

Type II (+) 0 Type II (-) 1

Critical micelle (CMC) .0001

● Using original Hand's rule

○ Using modified Hand's rule

Phase Behavior Type

● Using binodal curve

○ Using solubilization ratio

Interfacial Tension

● Healy and Reed's correlation

○ Huh's correlation

$\text{Log}_{10}\,\sigma_{\text{mw-oil}}$ 1.3 (dynes/cm)

Organic Mass Transfer

Residual saturation/Relative permeability

○ Not depend on capillary number

● Depend on capillary number

○ Depend on trapping number

Capillary desaturation curve parameter

aqueous 1865

oleic 59074

microemulsion phase 364.2

Residual saturation/Relative Permeability

Fig. 3.4. An example of physical property panel of UTCHEM GUI.

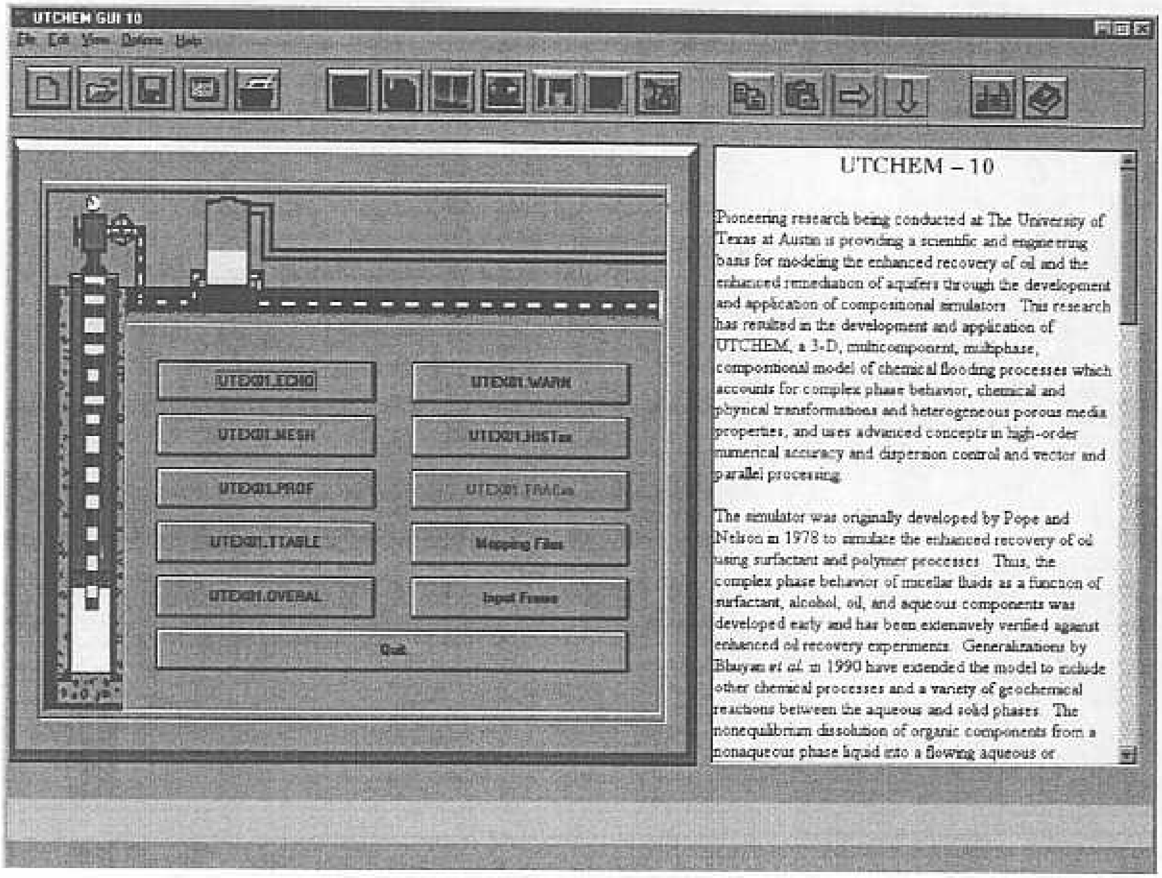

UTCHEM – 10

Pioneering research being conducted at The University of Texas at Austin is providing a scientific and engineering basis for modeling the enhanced recovery of oil and the enhanced remediation of aquifers through the development and application of compositional simulators. This research has resulted in the development and application of UTCHEM, a 3-D, multicomponent, multiphase, compositional model of chemical flooding processes which accounts for complex phase behavior, chemical and physical transformations and heterogeneous porous media properties, and uses advanced concepts in high-order numerical accuracy and dispersion control and vector and parallel processing.

The simulator was originally developed by Pope and Nelson in 1978 to simulate the enhanced recovery of oil using surfactant and polymer processes. Thus, the complex phase behavior of micellar fluids as a function of surfactant, alcohol, oil, and aqueous components was developed early and has been extensively verified against enhanced oil recovery experiments. Generalizations by Bhuyan *et al.* in 1990 have extended the model to include other chemical processes and a variety of geochemical reactions between the aqueous and solid phases. The nonequilibrium dissolution of organic components from a nonaqueous phase liquid into a flowing aqueous or

Fig. 3.5. The output panel of UTCHEM GUI.

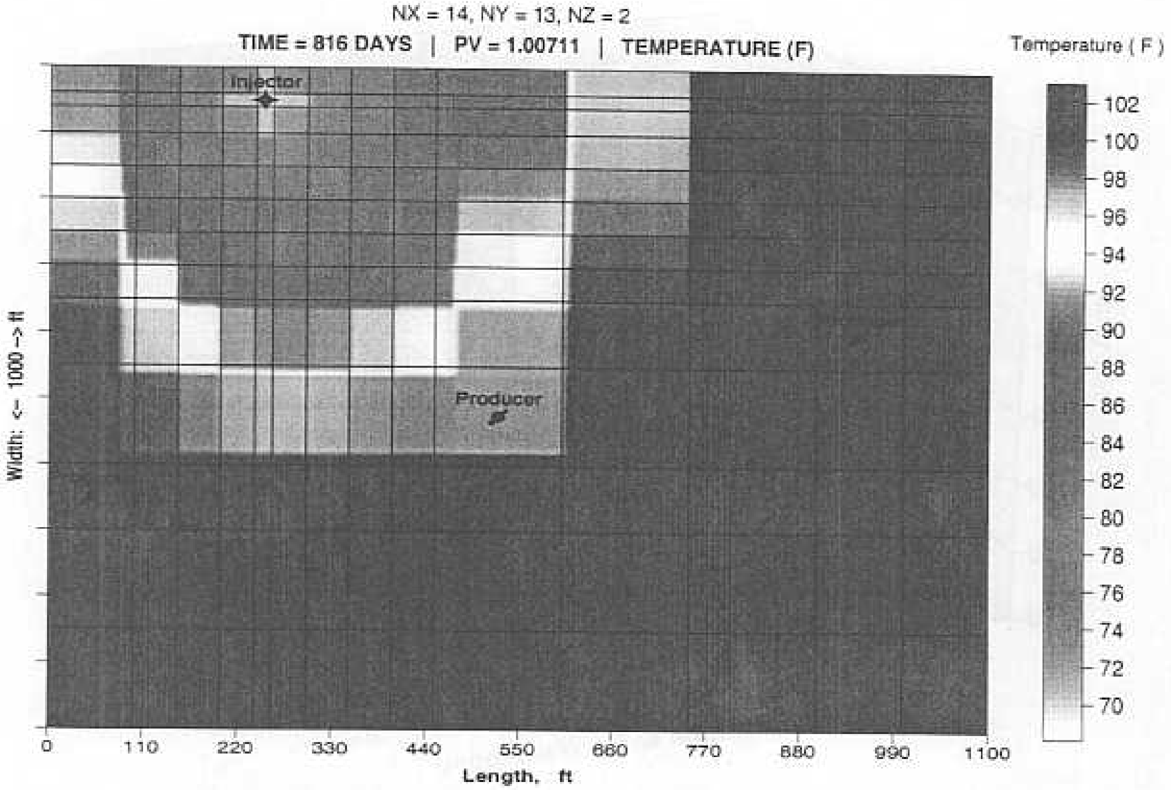

Fig. 3.6. Temperature profile for cold water injection.

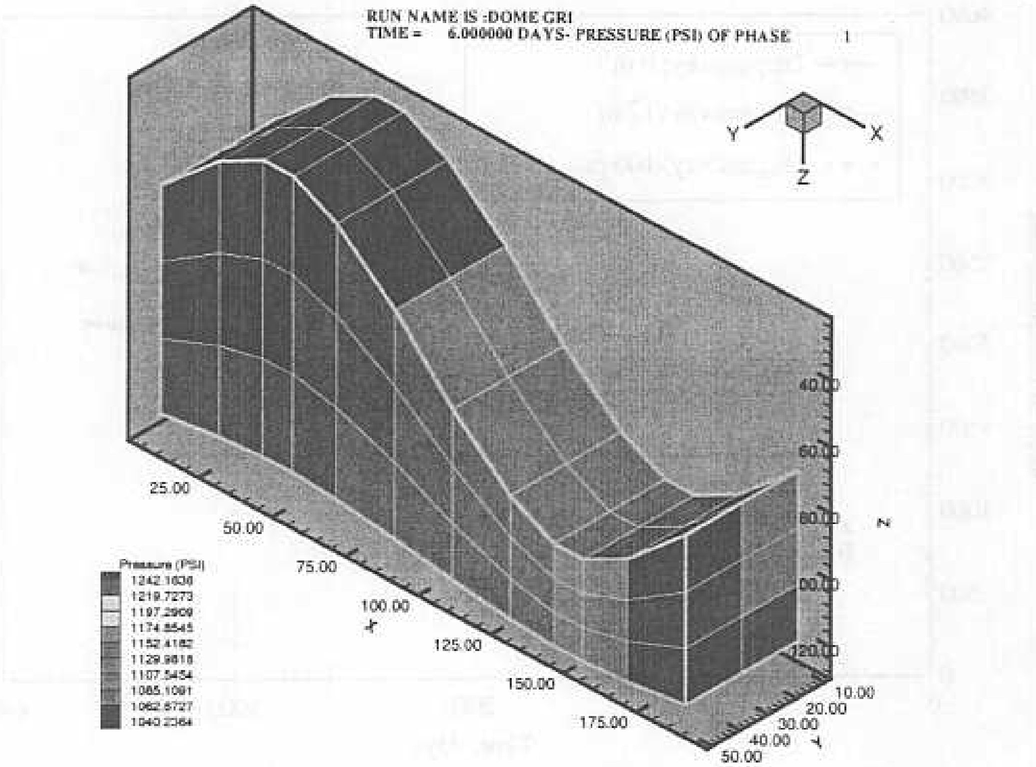

Fig. 3.7. Example of a 3-D pressure distribution map generated with UTPLOT utility.

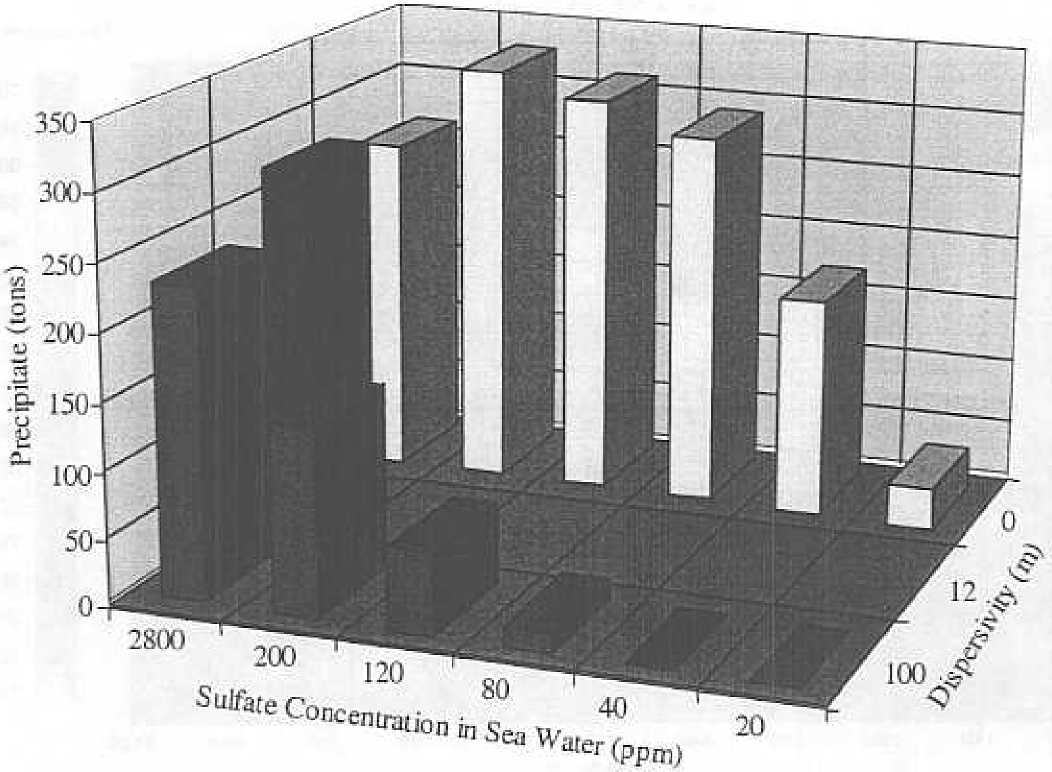

Fig. 3.8. Total amount of barium sulfate precipitate in the production wellbores.

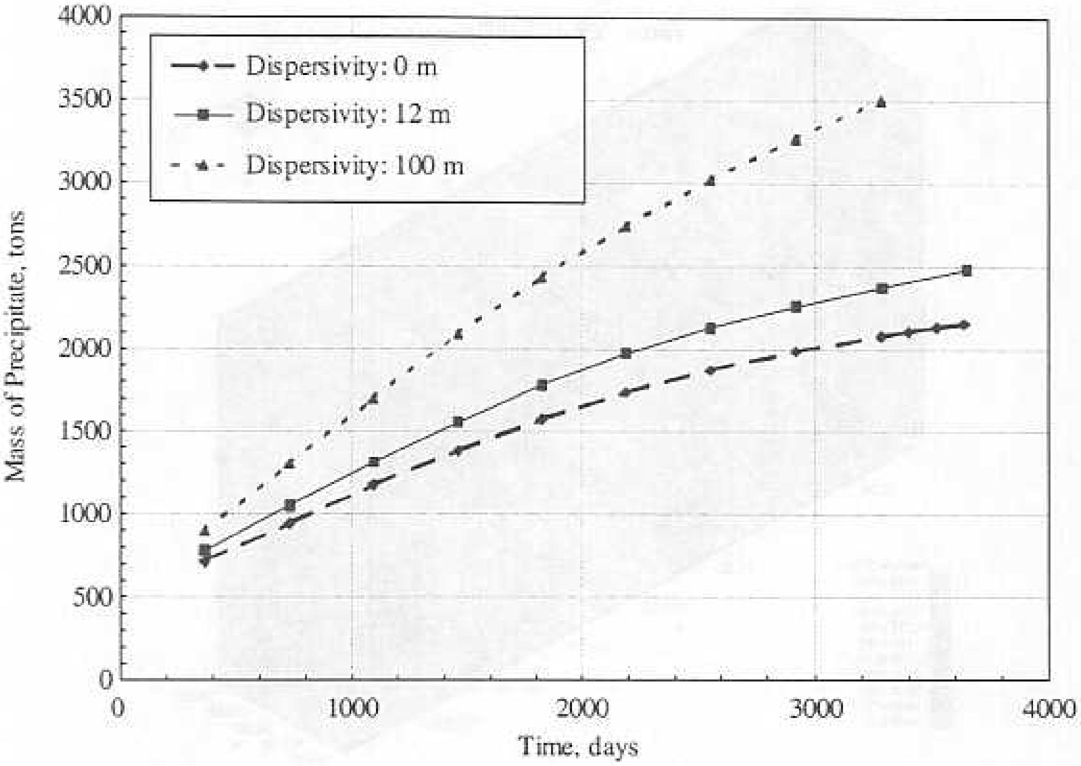

Fig. 3.9. Mass of $BaSO_4$ precipitated in the formation (120 ppm injected SO_4 and 151 ppm initial Ba concentration).

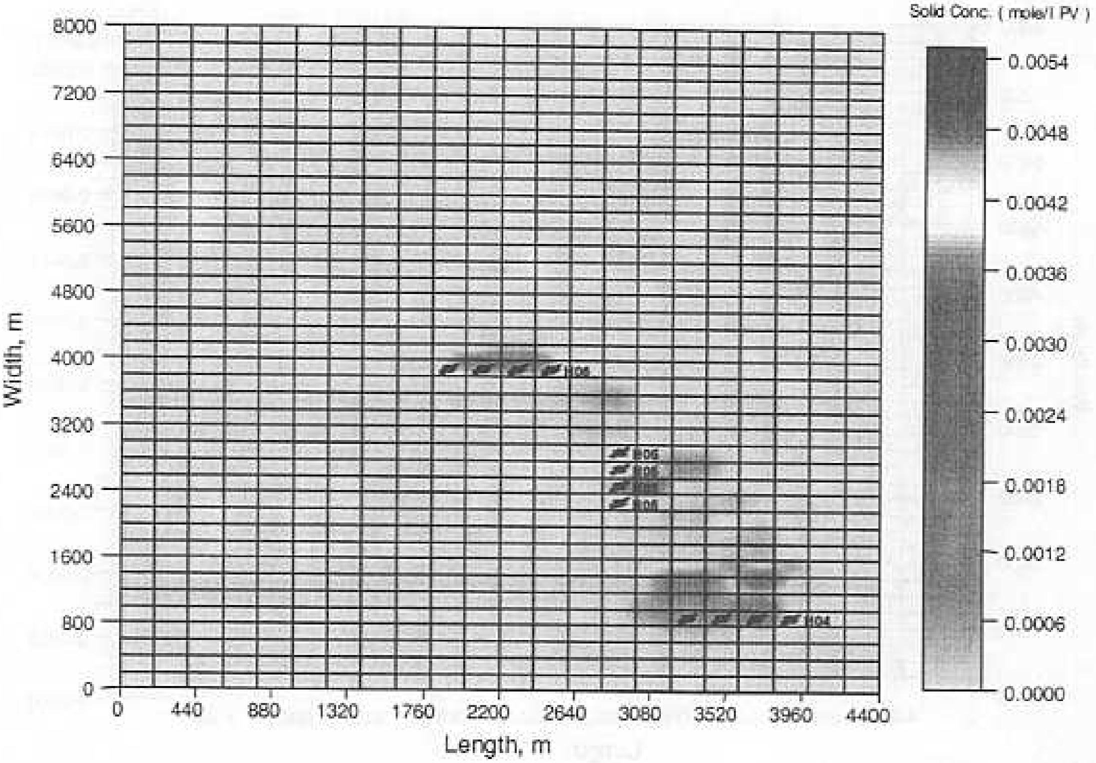

Fig. 3.10. Barium sulfate precipitate concentration in Layer 10 (dispersivity =0 m).

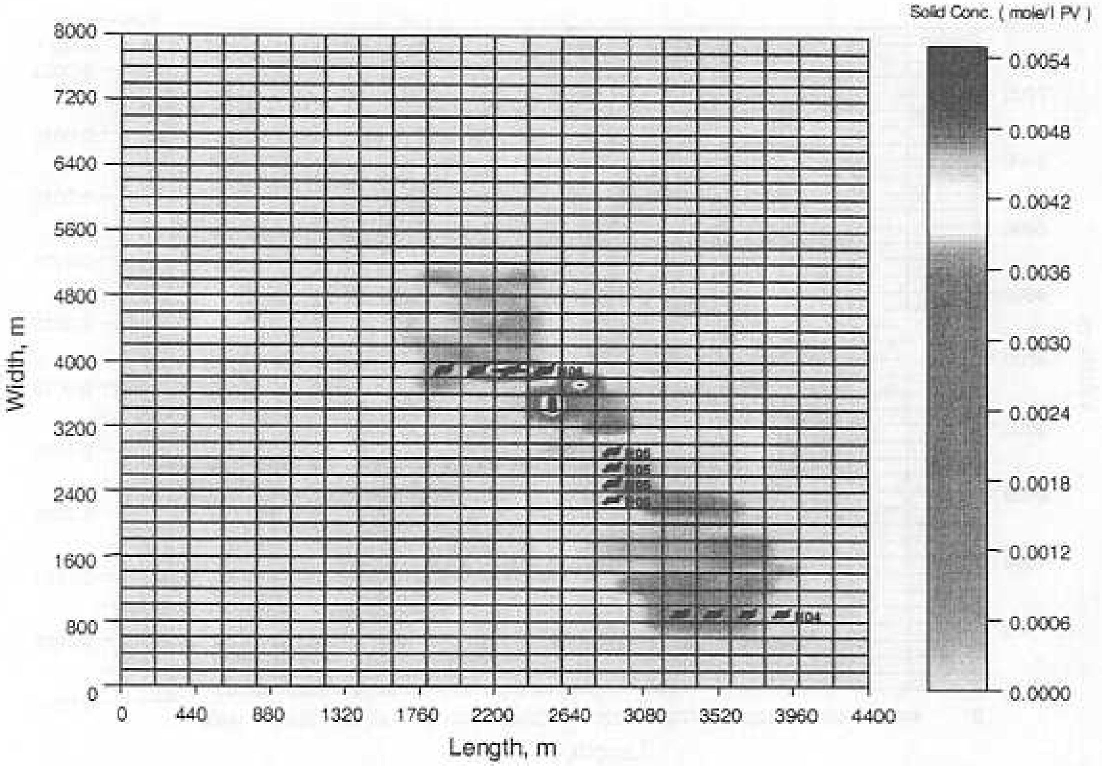

Fig. 3.11. Barium sulfate precipitate concentration in layer 10 (dispersivity = 100 m).

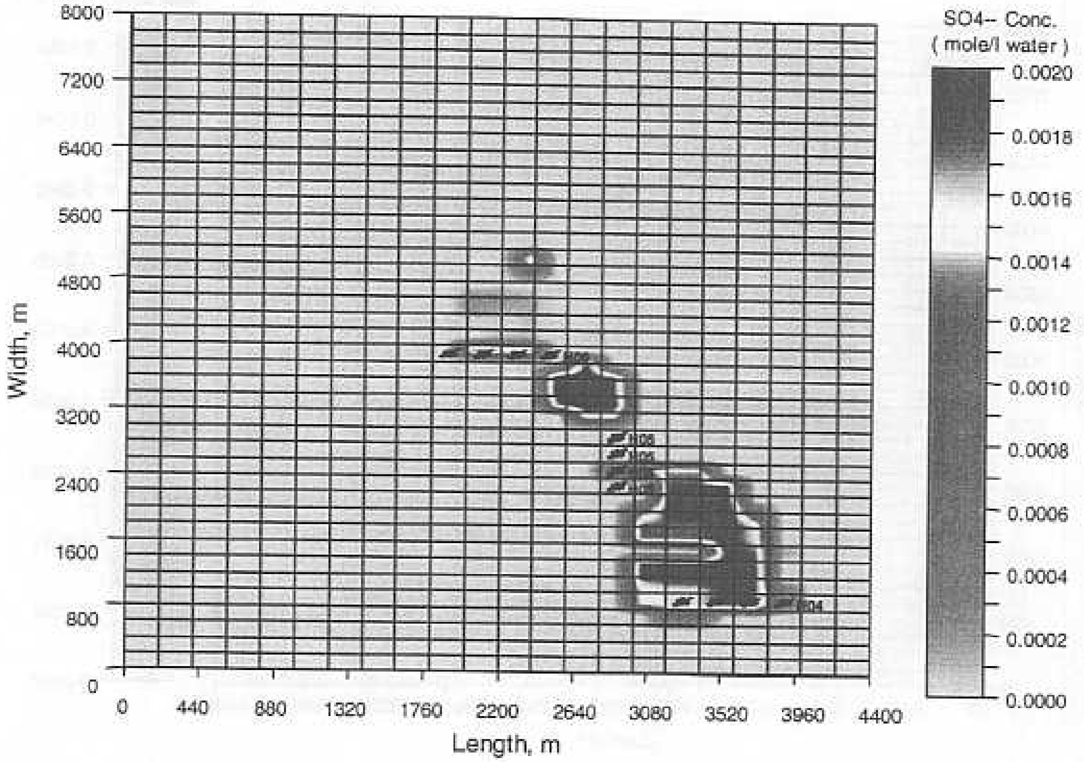

Fig. 3.12. Sulfate concentration in layer 10 (dispersivity = 0 m).

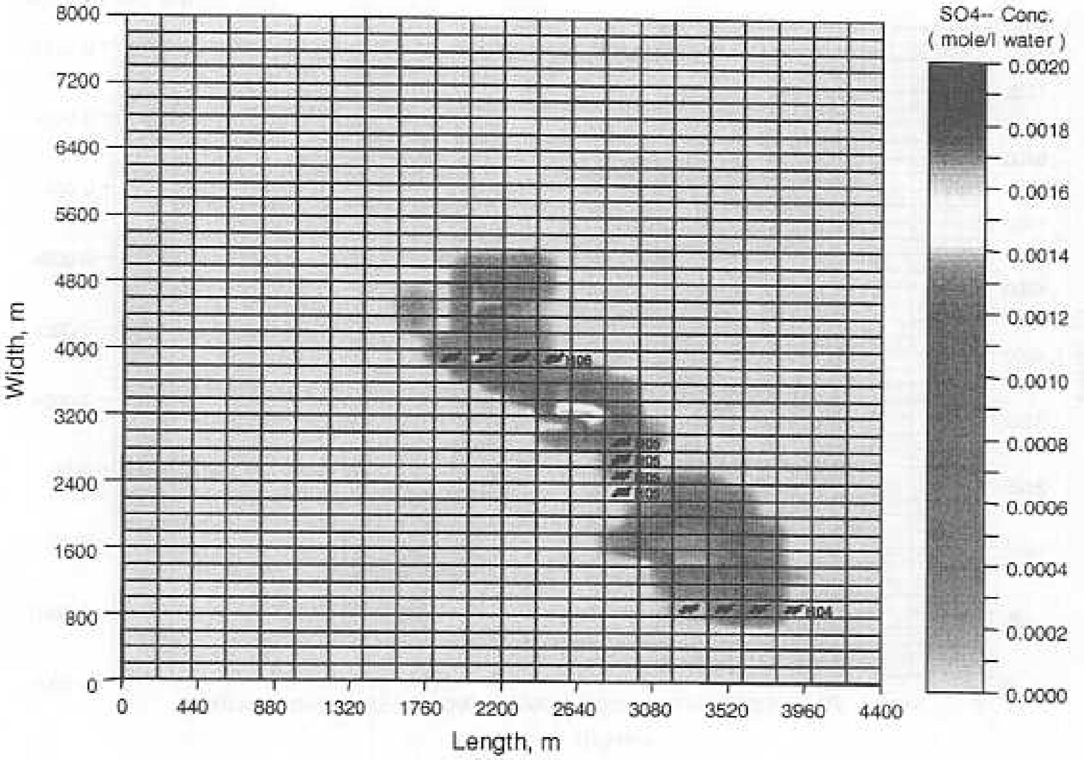

Fig. 3.13 . Sulfate concentration in layer 10 (dispersivity = 100m).

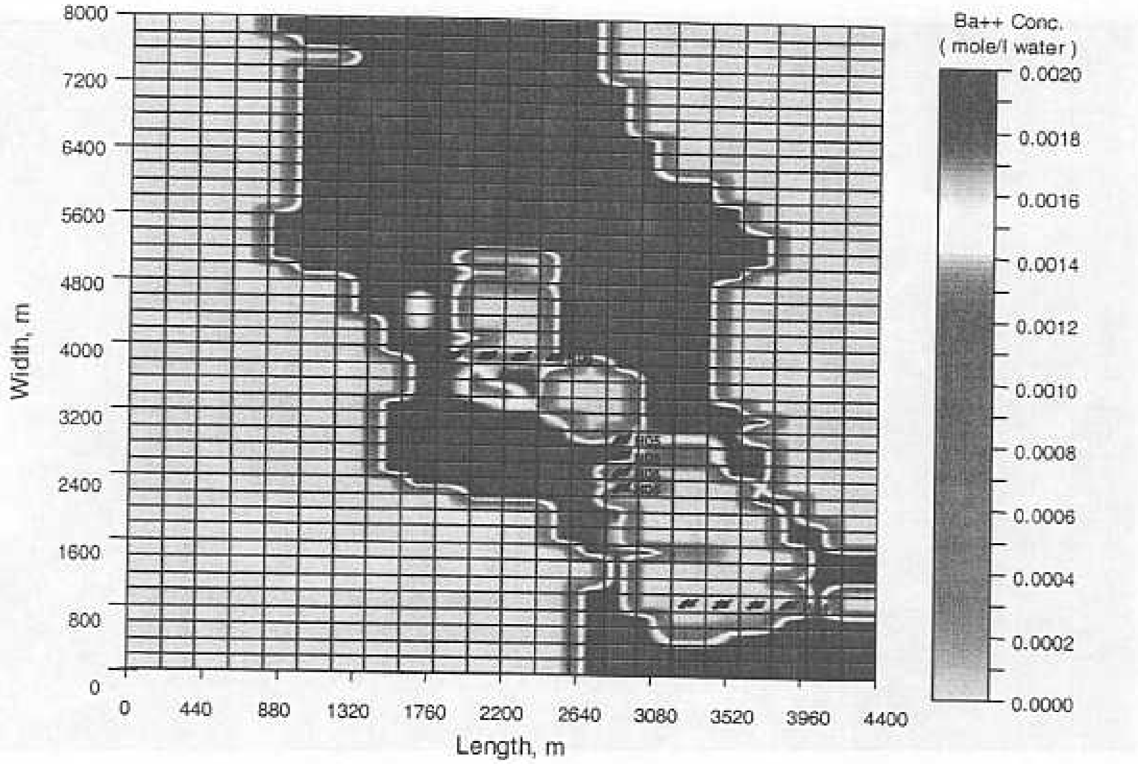

Fig. 3.14. Barium concentration in layer 10 (dispersivity = 0 m).

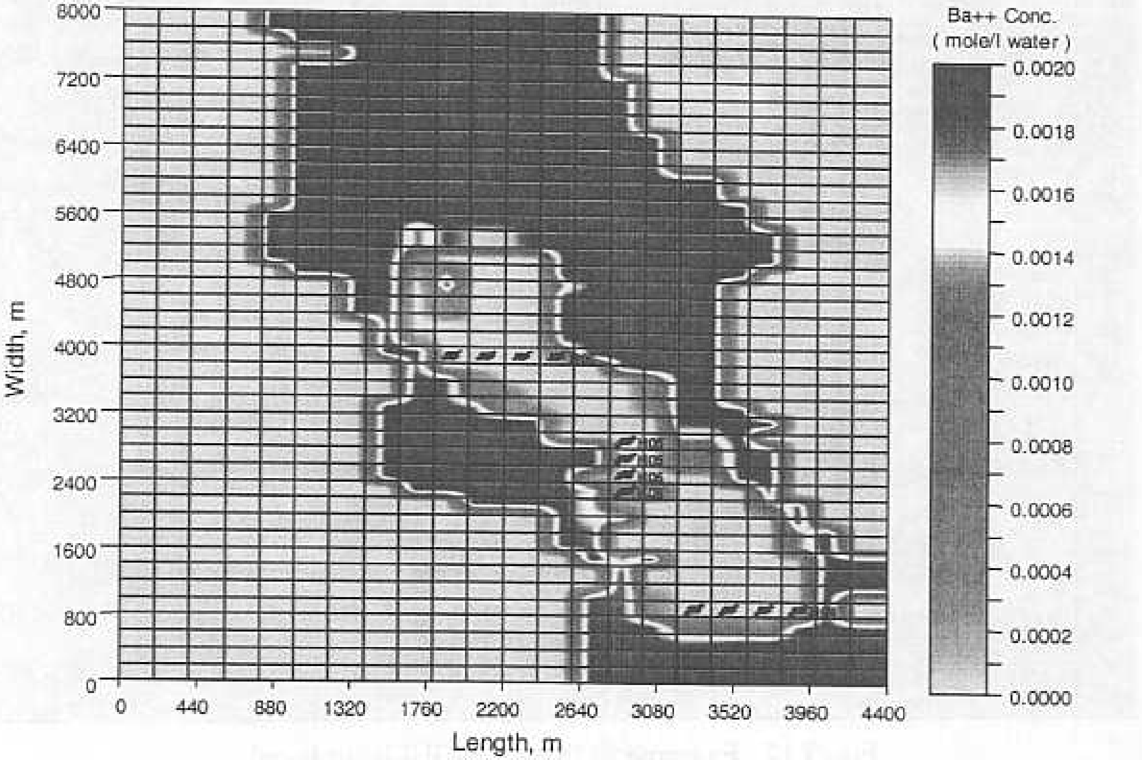

Fig. 3.15 . Barium concentration in layer 10 (dispersivity = 100m).

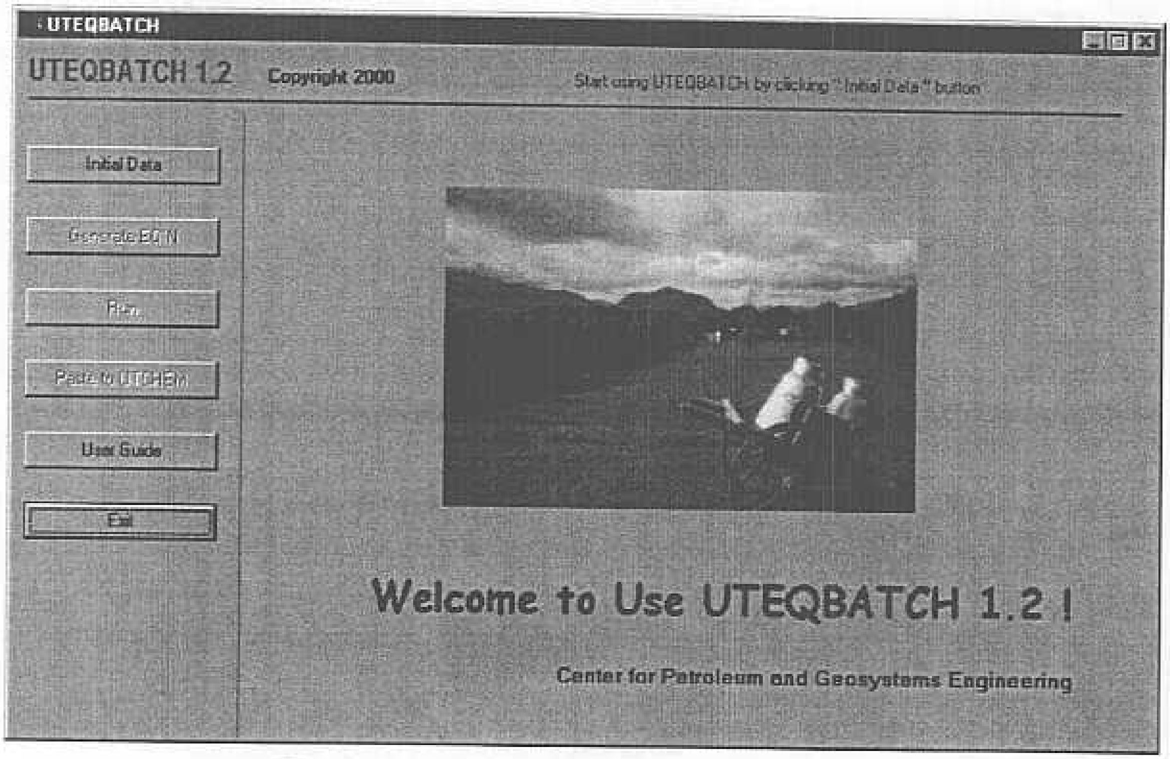

Start using UTEQBATCH by clicking " Initial Data " button

Welcome to Use UTEQBATCH 1.2 !

Center for Petroleum and Geosystems Engineering

Fig. 3.16: An example EQBATCH-GUI panel.

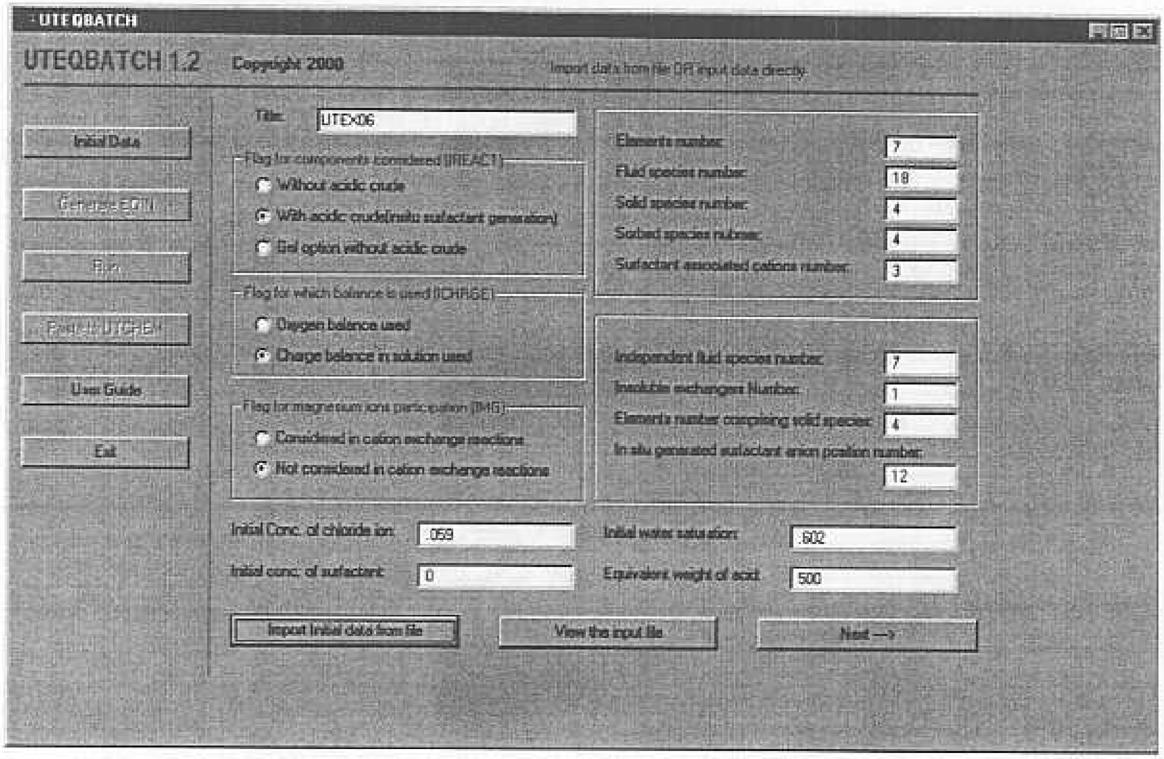

Import data from file OR input data directly

Title: UTEX06

Flag for components considered (IREACT)
- ○ Without acidic crude
- ● With acidic crude(insitu sufactant generation)
- ○ Gel option without acidic crude

Flag for which balance is used (ICHRGE)
- ○ Oxygen balance used
- ● Charge balance in solution used

Flag for magnesium ions participation (IMG)
- ○ Considered in cation exchange reactions
- ● Not considered in cation exchange reactions

Elements number: 7
Fluid species number: 18
Solid species number: 4
Sorbed species nubmer: 4
Sufactant associated cations number: 3

Independent fluid species number: 7
Insoluble exchangers Number: 1
Elements number comprising solid species: 4
In-situ generated sufactant anion position number: 12

Initial Conc. of chloride ion: .059
Initial conc. of sufactant: 0
Initial water saturation: .602
Equivalent weight of acid: 500

Fig. 3.17: Example EQBATCH-GUI input panel.

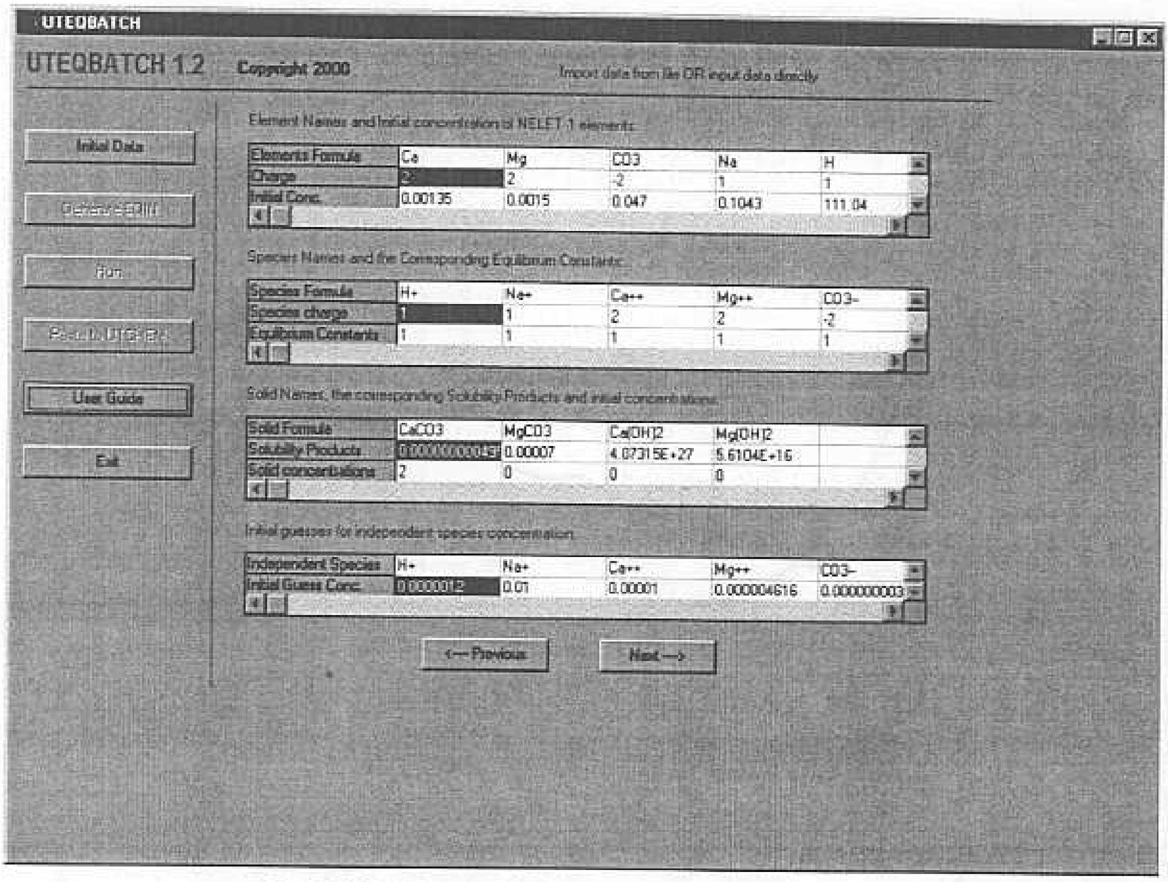

Element Names and Initial concentration of NELET-1 elements

Elements Formula	Ca	Mg	CO3	Na	H
Charge	2	2	-2	1	1
Initial Conc.	0.00135	0.0015	0.047	0.1043	111.04

Species Names and the Corresponding Equilibrium Constants

Species Formula	H+	Na+	Ca++	Mg++	CO3-
Species charge	1	1	2	2	-2
Equilibrium Constants	1	1	1	1	1

Solid Names, the corresponding Solubility Products and initial concentrations

Solid Formula	CaCO3	MgCO3	Ca(OH)2	Mg(OH)2	
Solubility Products	0.00000000004	0.00007	4.07315E+27	5.6104E+16	
Solid concentrations	2	0	0	0	

Initial guesses for independent species concentration

Independent Species	H+	Na+	Ca++	Mg++	CO3-
Initial Guess Conc.	0.0000012	0.01	0.00001	0.000004616	0.000000003

Fig. 3.18: Example EQBATCH-GUI input panel.

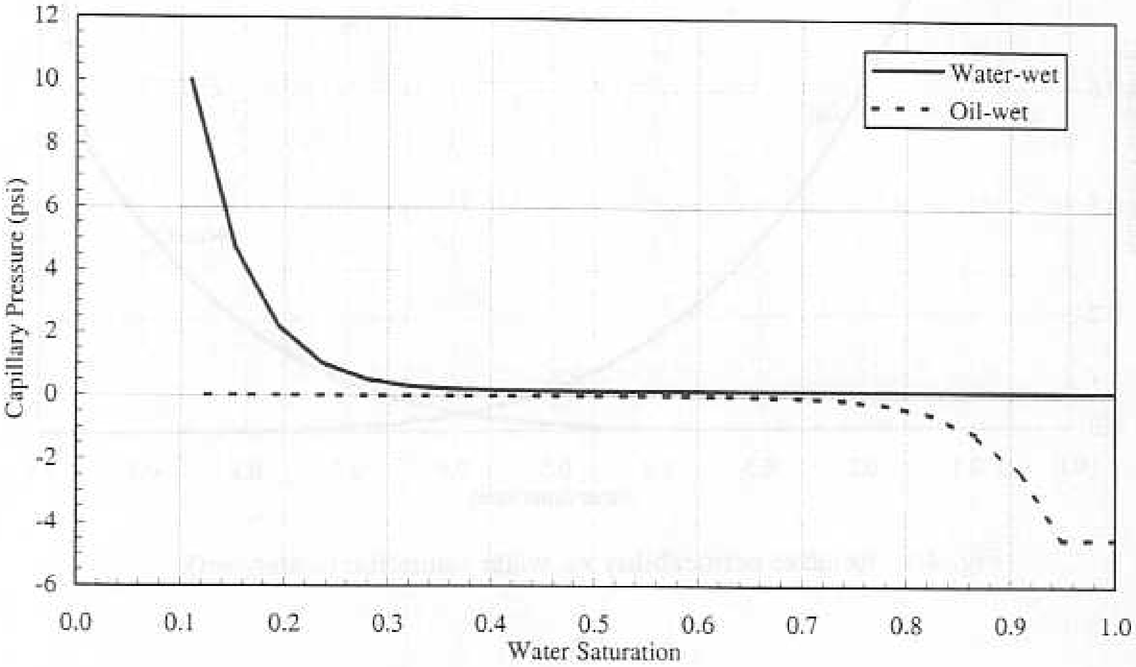

Fig. 4.1: Capillary pressure curves for water-wet and oil-wet rocks.

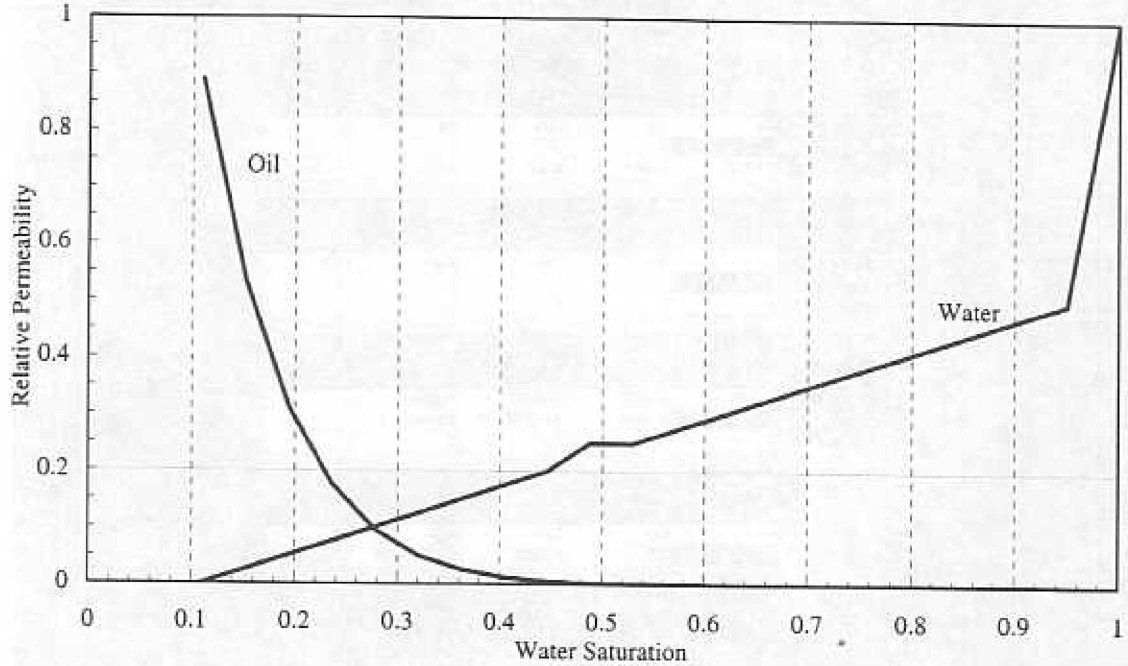

Fig. 4.2: Relative permeability vs. water saturation (oil-wet).

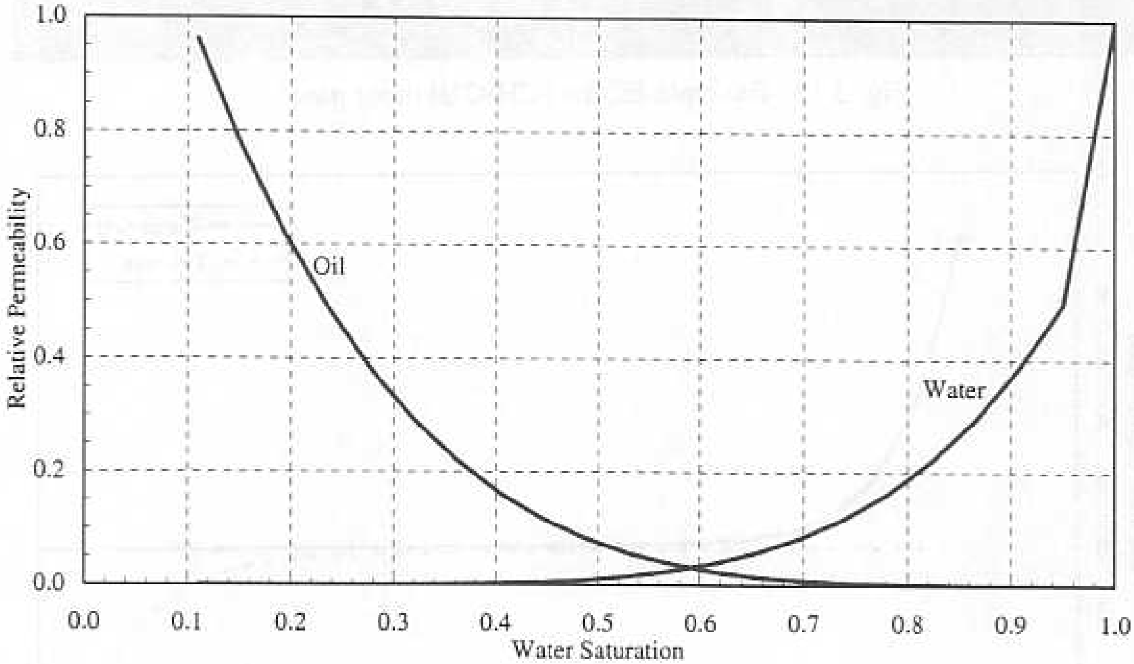

Fig. 4.3: Relative permeability vs. water saturation (water-wet).

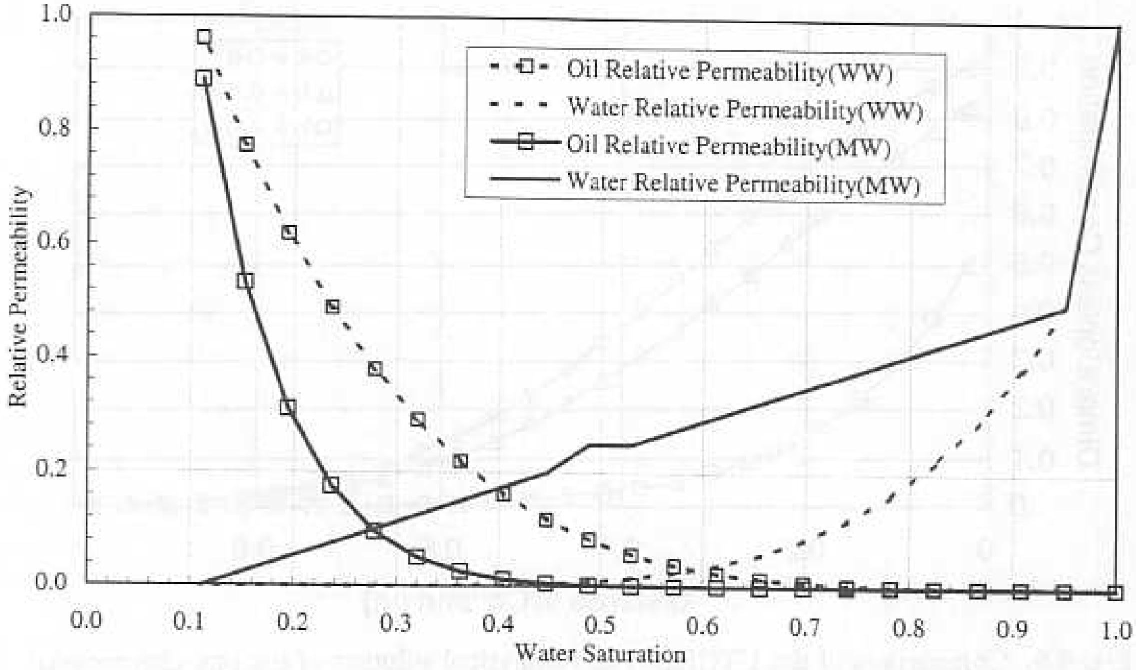

Fig. 4. 4: Relative permeability curves for water-wet and oil-wet rocks.

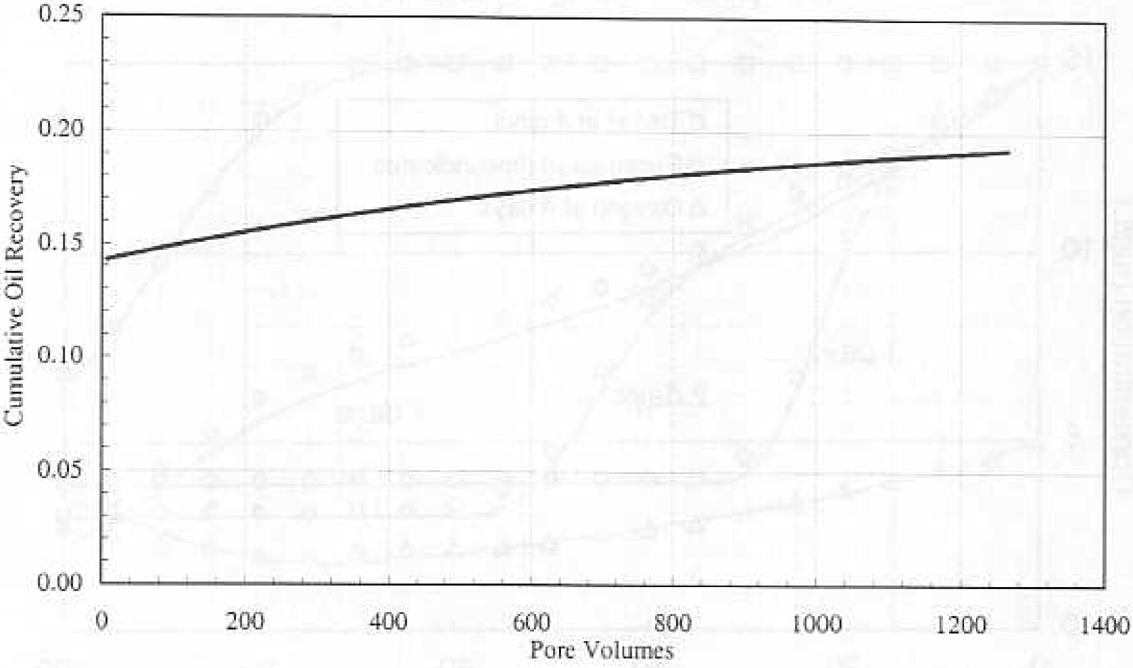

Fig. 4.5: Cumulative oil recovery during the surfactant imbibition test.

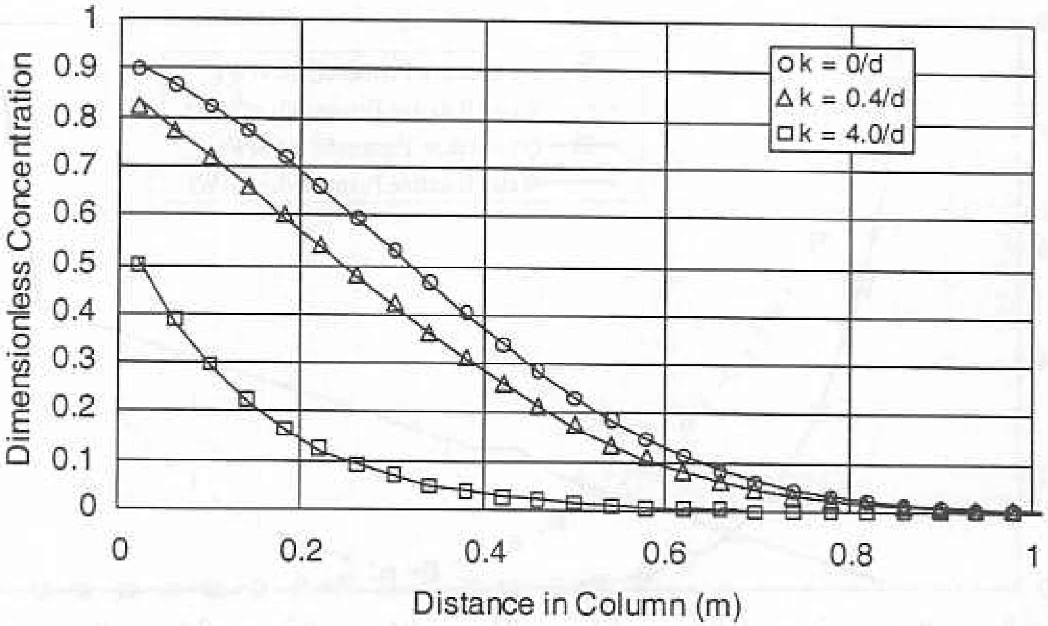

Fig. 4.6. Comparison of the UTCHEM and analytical solution of the one-dimensional advection-dispersion equation. The UTCHEM solution is represented by the symbols, and the analytical solution is represented by the solid line. Flow parameters are given in Table 4.1.

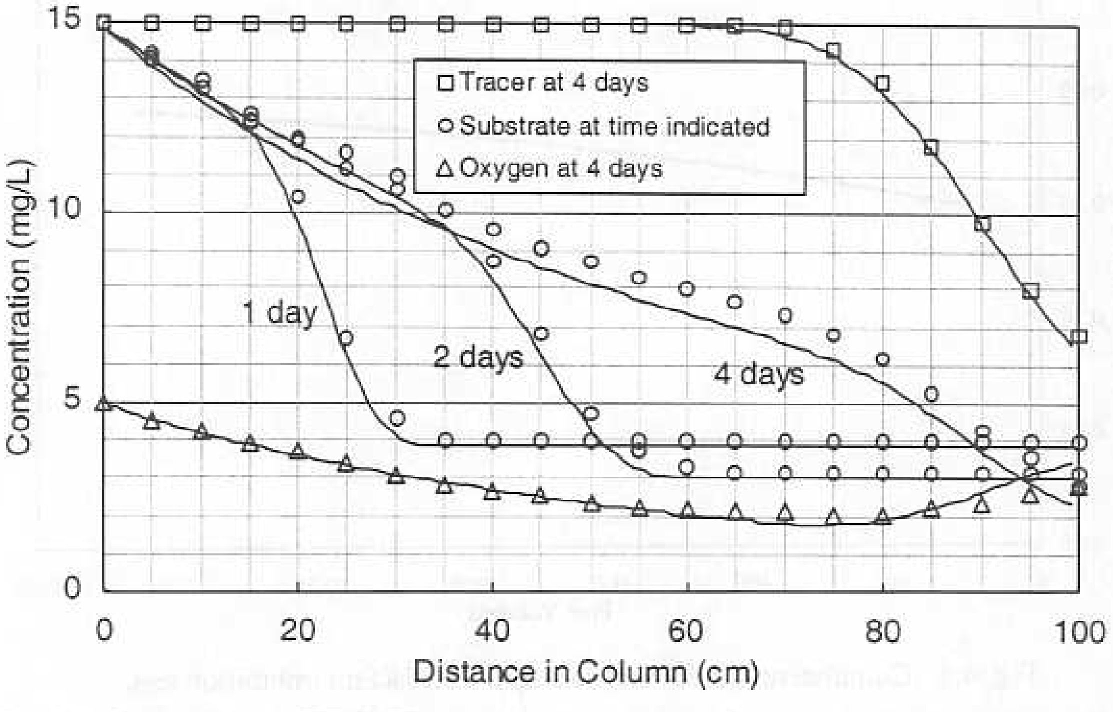

Fig. 4.7. Comparison of UTCHEM and Molz *et al.* [1986] solution of the biodegradation of a single substrate by a single microbial species using a single electron acceptor in a 1-m long column. Flow and kinetic parameters are given in Table 4.2.

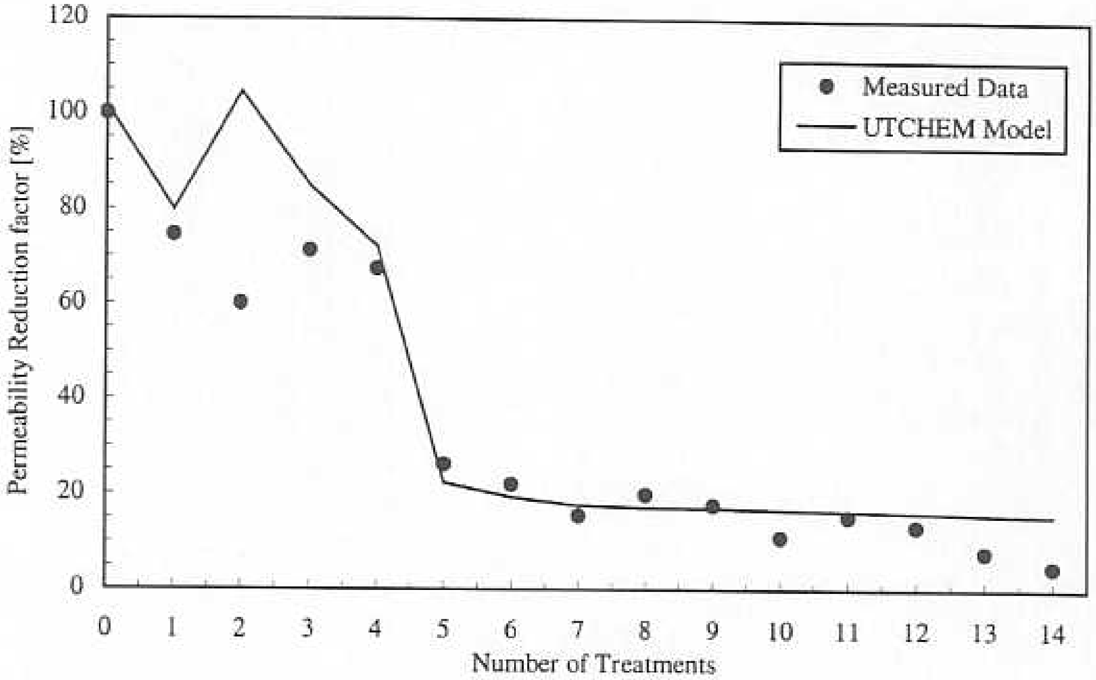

Fig. 4.8. Comparison of measured permeability reduction factor of Silfanus (1990) and UTCHEM simulation results.

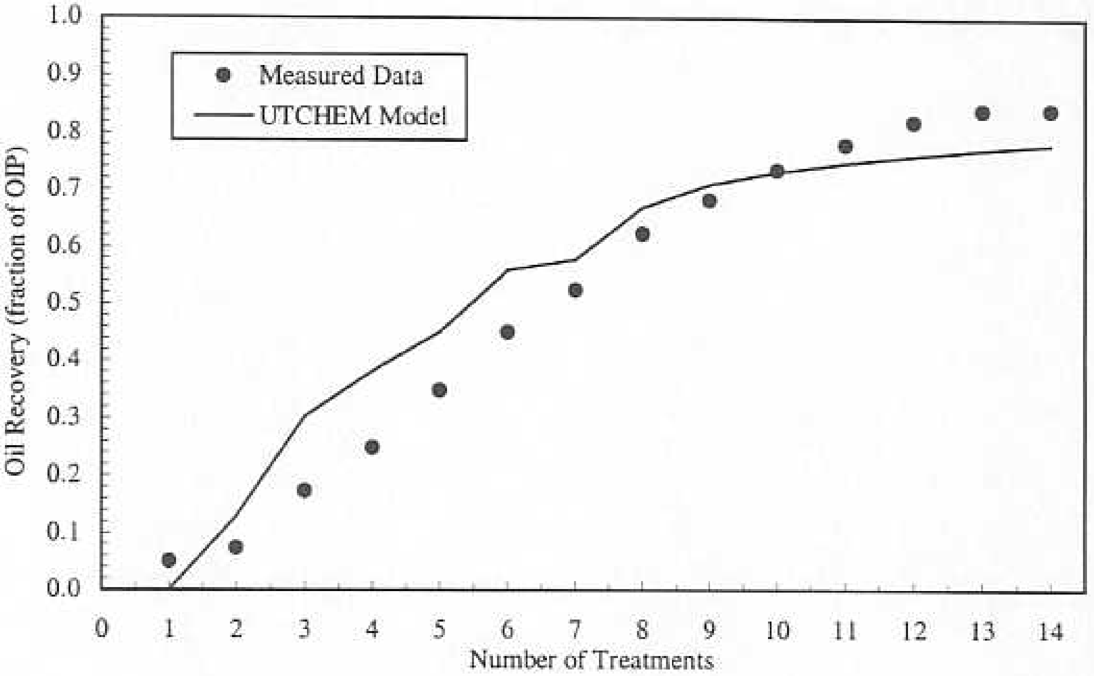

Fig. 4.9. Comparison of measured oil recovery of Silfanus (1990) and UTCHEM simulation results.